

Search for displaced leptons in proton-proton collisions at  
 $\sqrt{s} = 13 \text{ TeV}$

Dissertation

Presented in Partial Fulfillment of the Requirements for the Degree  
Doctor of Philosophy in the Graduate School of The Ohio State  
University

By

Bryan Cardwell, B.S., M.S.

Graduate Program in Physics

The Ohio State University

2021

Dissertation Committee:

Christopher Hill, Advisor

Stanley Durkin

Linda Carpenter

Andrew Heckler

© Copyright by

Bryan Cardwell

2021

## Abstract

A search is presented for new long-lived particles that propagate a measurable distance through the CMS detector before decaying to leptons. The search is performed in  $113\text{--}118\,\text{fb}^{-1}$  of proton-proton collision data produced by the CERN LHC at a center-of-mass energy of 13 TeV and collected by the CMS detector in 2016, 2017, and 2018. Events are selected with two leptons (an electron and a muon, two electrons, or two muons) that both have transverse impact parameter values between 0.01 cm and 10 cm. Using transverse impact parameter as the discriminating variable allows for sensitivity to displaced decays without requiring that the leptons form a common vertex. The search is designed to be sensitive to a wide range of new physics models that produce displaced di-lepton final states. The observation is consistent with the background-only hypothesis, and limits are set on the product of the cross-section of top squark pair production and the branching fraction to a lepton and a  $b$  or  $d$  quark through an R-parity-violating vertex. For a proper decay length hypothesis of 2 cm, top squarks with masses up 1500 GeV are excluded at the 95 % confidence level.

For Cristiana and Montague.

## **Vita**

2015 .....	B.S. Physics, North Central College
2015-2017 .....	Graduate Teaching Associate, The Ohio State University
2017 .....	M.S. Physics, The Ohio State University
2017-present .....	Graduate Research Associate, The Ohio State University

## **Publications**

### **Research Publications**

Included in the author list of 78 publications from CMS.

## **Fields of Study**

Major Field: Physics

## Table of Contents

	Page
Abstract . . . . .	ii
Dedication . . . . .	iii
Vita . . . . .	iv
List of Tables . . . . .	viii
List of Figures . . . . .	xii
1. Introduction . . . . .	1
1.1 The Standard Model . . . . .	2
1.1.1 Quantum chromodynamics . . . . .	4
1.1.2 The electroweak theory . . . . .	4
1.1.3 The Higgs mechanism . . . . .	5
1.1.4 Current status . . . . .	7
1.2 Beyond the Standard Model . . . . .	10
1.2.1 Supersymmetry . . . . .	10
1.2.2 Long-lived particles . . . . .	12
1.2.3 Displaced supersymmetry . . . . .	15
2. The Large Hadron Collider and Compact Muon Solenoid experiment . .	19
2.1 The Large Hadron Collider . . . . .	19
2.1.1 Injection chain . . . . .	20
2.1.2 Main ring . . . . .	21
2.2 The Compact Muon Solenoid experiment . . . . .	27
2.2.1 Solenoid magnet . . . . .	29
2.2.2 Tracker . . . . .	29

2.2.3	Electromagnetic calorimeter . . . . .	35
2.2.4	Hadronic calorimeter . . . . .	37
2.2.5	Muon system . . . . .	39
2.2.6	Trigger . . . . .	41
2.2.7	Physics object reconstruction . . . . .	43
3.	Search for displaced leptons . . . . .	48
3.1	Overview . . . . .	50
3.1.1	Long-lived particles at the LHC . . . . .	50
3.1.2	Displaced leptons signature . . . . .	52
3.1.3	Analysis strategy . . . . .	55
3.2	Data and simulated samples . . . . .	58
3.2.1	Experimental data . . . . .	58
3.2.2	Simulated background events . . . . .	58
3.2.3	Simulated signal events . . . . .	59
3.3	Event selection . . . . .	62
3.3.1	Triggers . . . . .	62
3.3.2	Preselection . . . . .	64
3.3.3	Prompt control region . . . . .	74
3.3.4	Inclusive signal region . . . . .	77
3.4	Corrections to simulation . . . . .	80
3.4.1	Pileup . . . . .	80
3.4.2	Lepton ID . . . . .	80
3.4.3	Lepton $d_0$ resolution . . . . .	80
3.4.4	Trigger efficiency . . . . .	85
3.5	Background estimation . . . . .	89
3.5.1	Background sources . . . . .	89
3.5.2	Data-driven ABCD method . . . . .	91
3.5.3	Closure tests in control regions . . . . .	95
3.5.4	ABCD correction and systematic uncertainty . . . . .	97
3.5.5	Testing full background estimation procedure . . . . .	103
3.5.6	Additional background checks . . . . .	104
3.6	Systematic uncertainties . . . . .	112
3.6.1	Integrated luminosity . . . . .	112
3.6.2	Pileup . . . . .	112
3.6.3	Displaced tracking efficiency . . . . .	114
3.6.4	Trigger efficiency . . . . .	114
3.6.5	Lepton ID and isolation . . . . .	114
3.6.6	Muon pixel hit efficiency . . . . .	115
3.6.7	Lepton $d_0$ resolution . . . . .	116
3.7	Results . . . . .	117

3.7.1	Observed events . . . . .	117
3.7.2	Limits . . . . .	122
3.7.3	Additional likelihood tests . . . . .	126
4.	Conclusion . . . . .	130
Appendices		133
A.	Impact of APV25 saturation on displaced tracking . . . . .	133
B.	Poorly measured lepton $ d_0 $ at large $ \eta $ . . . . .	137
C.	Displaced tracking efficiency . . . . .	139
Bibliography . . . . .		147

## List of Tables

Table	Page
2.1 Luminosity parameters used in Eq. (2.1). . . . .	22
3.1 The top squark production cross sections used when generating the simulated $\tilde{t}\tilde{t} \rightarrow \bar{l}b\bar{l}b$ and $\tilde{t}\tilde{t} \rightarrow \bar{l}d\bar{l}d$ events. Cross sections are calculated at NLO + NLL by the LHC SUSY Cross Section Working Group. . .	61
3.2 The $e\mu$ preselection criteria. The electron and muon $p_T$ thresholds increase in 2017 in accordance with the increased HLT electron and muon $p_T$ thresholds. . . . .	65
3.3 The $ee$ preselection criteria. The electron $p_T$ threshold increases in 2017 and 2018 in accordance with the increased HLT electron $p_T$ threshold. .	66
3.4 The $\mu\mu$ preselection criteria. The muon $p_T$ threshold increases in 2017 and 2018 in accordance with the increased HLT muon $p_T$ threshold. .	67
3.5 The electron tight ID requirements, which are identical to the tight cut-based ID from the CMS EGamma Physics Object Group with the $d_0$ and $d_z$ requirements removed. Electron ID quantity definitions are available in Ref. [1]. . . . .	68
3.6 The muon tight ID requirements, which are identical to the tight cut-based ID from the CMS Muon Physics Object Group with the requirements on $d_0$ and $d_z$ removed. . . . .	69
3.7 The cumulative efficiency for simulated $\tilde{t}\tilde{t} \rightarrow \bar{l}b\bar{l}b$ signal events to pass the 2018 inclusive signal region selection, for several choices of $\tilde{t}$ mass and $c\tau$ . The corrections described in Section 3.4 are applied. . . . .	79

3.8	The average $\sigma_{align}$ for electrons and muons, for the 2017 and 2018 analyses. . . . .	83
3.9	The unprescaled $p_T^{\text{miss}}$ triggers used to create an orthogonal data sample for the trigger efficiency calculation. . . . .	86
3.10	The trigger efficiency scale factors in each channel and year. . . . .	87
3.11	The $p_T$ boundaries between the low- and high- $p_T$ bins of SR I in each channel. . . . .	94
3.12	Closure test results in data and background simulation in the 100–500 $\mu\text{m}$ region. The average extrapolated ratios and their statistical uncertainties are given. For each test, the A, B, C, and D regions are defined as follows: A is 20–30 $\mu\text{m}$ in prompt lepton $ d_0 $ and 20–100 $\mu\text{m}$ in displaced lepton $ d_0 $ , B is 20–30 $\mu\text{m}$ in prompt lepton $ d_0 $ and 100–500 $\mu\text{m}$ in displaced lepton $ d_0 $ , C is always 20–100 $\mu\text{m}$ in displaced lepton $ d_0 $ , D (the test region) is always 100–500 $\mu\text{m}$ in displaced lepton $ d_0 $ , and we perform repeated tests while simultaneously varying the C and D prompt lepton $ d_0 $ within the 30–100 $\mu\text{m}$ range. . . . .	96
3.13	Closure test results in data and background simulation in the 500 $\mu\text{m}$ –10 cm region. The ratios of the actual to the estimated yield and their statistical uncertainties are given. The A, B, C, and D regions are defined as follows: A is 20–30 $\mu\text{m}$ in prompt lepton $ d_0 $ and 20–100 $\mu\text{m}$ in displaced lepton $ d_0 $ , B is 20–30 $\mu\text{m}$ in prompt lepton $ d_0 $ and 500 $\mu\text{m}$ –10 cm in displaced lepton $ d_0 $ , C is 30–100 $\mu\text{m}$ in prompt lepton $ d_0 $ and 20–100 $\mu\text{m}$ in displaced lepton $ d_0 $ , and D (the test region) is 30–100 $\mu\text{m}$ in prompt lepton $ d_0 $ and 500 $\mu\text{m}$ –10 cm in displaced lepton $ d_0 $ . . . . .	98
3.14	The correction factors and the uncorrected and corrected background estimates in SR I. The correction factor uncertainties include both the uncertainty in the average and the additional uncertainty obtained from varying the fit extrapolation point. The total uncertainty (statistical plus systematic) is given for the corrected background estimates.	103
3.15	The systematic uncertainty and the background estimates in SRs II, III, and IV. The total uncertainty (statistical plus systematic) is given for each estimate. . . . .	104

3.16 Closure test results in background simulation in the SRs with all background estimate corrections and uncertainties applied. The estimated number of events, the actual number of events, and their total uncertainties (statistical plus systematic) are given. In cases where the actual number of events is zero, the uncertainty is given by the product of the average background simulation event weight and the upper bound of the 68% Poisson interval given by a single observation of zero events. . . . .	105
3.17 Some properties of the seven events found in data with the material interactions selection inverted. . . . .	106
3.18 Background estimates in data while applying the 2018 $\mu\mu$ preselection and the additional requirement of at least one $b$ -tagged jet. The estimates with at least one $b$ -tagged jet are about an order of magnitude below the nominal prediction. . . . .	107
3.19 A closure test of the ABCD method in 2018 QCD simulation in the $\mu\mu$ channel with the muon isolation criterion inverted. The estimates from the ABCD method, the actual yields in simulation, and the ratios of the actual to the estimated yields are shown. . . . .	109
3.20 Systematic uncertainties in the signal efficiency for all three years and the three channels. The mean is provided in cases where the uncertainty varies by signal sample. Uncertainties in the same row are treated as correlated among the years of data taking, except for the displaced tracking and muon pixel hit efficiencies, where the 2016 uncertainty is treated as uncorrelated with the 2017 and 2018 uncertainties.	113
3.21 The number of estimated background and observed events in each channel and SR. For each estimate, the total uncertainty is given. The $p_T$ boundaries that separate the low- and high- $p_T$ bins of SR I are listed in Table 3.11. . . . .	118
3.22 The pre- and post-fit predictions for each signal region bin. . . . .	127
C.1 Cosmic-ray muon arrival time requirements used when measuring displaced tracking efficiency in data and simulation. . . . .	142

C.2 Mean measured efficiency to reconstruct both lepton tracks in simulated $\tilde{t}\bar{t} \rightarrow \bar{l}b\bar{l}b$ events in data and simulation and the resulting systematic uncertainty. The top squark mass and proper decay length are assumed to be 1800 GeV and 100 cm. . . . .	146
--	-----

## List of Figures

Figure	Page
1.1 The Standard Model particle content. . . . .	3
1.2 Summary of Standard Model production cross section measurements from the CMS experiment [2]. . . . .	8
1.3 The Higgs boson mass corrected by a fermion loop (left) and a fermion mass corrected by photon loop (right). . . . .	10
1.4 Corrections to the Higgs boson mass from the top quark (left) and top squark (right) cancel in exact SUSY. The top quark and top squark contributions are enhanced by the large coupling between the large Higgs-top quark coupling. . . . .	11
1.5 Mass limits at 95 % CL for a simplified model of gluino pair production with gluino decays to pairs of top quarks and the LSP (left) and top squark pair production with squark decays to a top quark and the LSP (right) from several CMS analyses [3]. . . . .	12
1.6 Masses and proper decay lengths of many Standard Model particles. Particles with proper decay lengths above approximately $10^{-4}$ m will be noticeably long-lived in collider detectors such as CMS [4]. . . . .	13
1.7 Long-lived decays of the neutron (left) and muon (right). . . . .	14
1.8 Pair-produced top squarks that each decay to a bottom quark and a lepton through an R-parity-violating $LQD$ vertex. . . . .	17
2.1 Layout of the LHC experiments [5]. . . . .	20

2.2	A diagram of the CERN accelerator complex. The analysis presented in Chapter 3 utilizes protons accelerated by LINAC 2, BOOSTER (also known as PSB), PS, SPS, and finally the LHC before their ultimate collision inside CMS [6]. . . . .	21
2.3	The peak instantaneous (top) and integrated (bottom) luminosity delivered by the LHC during proton operation between 2011 and 2018 [7]. . . . .	24
2.4	Diagram of an LHC dipole magnet in cross-section [8]. . . . .	25
2.5	The CMS detector [9]. . . . .	28
2.6	The stored-energy-over-mass ratio, $E/M$ , for several detector magnets (left), and a cross-sectional view of the four-layer winding of reinforced conductor in the CMS superconducting solenoid (right) [10]. . . . .	30
2.7	Measured single hit efficiency per layer as a function of the instantaneous luminosity (left) and pileup interactions (right) in data taken with the original CMS pixel detector in 2016 [11]. . . . .	33
2.8	Comparison of the original and Phase-1 CMS pixel detector layouts in $y$ - $z$ plane [12]. . . . .	34
2.9	Layout of the CMS silicon tracker. TIB, TOB, TID, and TEC refer to subdetectors of the strip detector while PIXEL refers to the original pixel detector. The Phase-1 pixel detector is contained within the same volume [10]. . . . .	35
2.10	The observed local p-value for the five decay modes and the overall combination as a function of the SM Higgs boson mass showing the importance of the ECAL mass resolution in the discovery of the Higgs boson by the CMS experiment. The dashed line shows the expected local p-values for a SM Higgs boson with a mass $m_H$ [13]. . . . .	36
2.11	Layout of the hadron calorimeter barrel (HB), outer (HO), endcap (HE), and forward (HF) subdetectors [10]. . . . .	38
2.12	Muon momentum resolution as a function of momentum when using the CMS muon system, the CMS inner tracker, and the combination of the two subdetectors in two different $\eta$ ranges [14]. . . . .	40

2.13 Sketch of a CMS muon system drift cell showing drift lines and isochrones.	41
The plates at the top and bottom of the cell are at ground potential while the voltages applied to the electrodes are +3600 V for wires, +1800 V for strips, and -1200 V for cathodes [10]. . . . .	
2.14 A sketch of a transverse slice of the CMS detector showing representative particle interactions used to identify and reconstruct particles with the CMS Particle Flow algorithm [15]. . . . .	47
3.1 Illustration of several possible experimental signatures of long-lived particles [16]. . . . .	51
3.2 Illustration of the displaced leptons signature showing the definition of $d_0$ in a transverse view of the CMS detector. $X$ denotes a new long-lived particle, $\ell$ denotes an electron or muon, and $Y$ denotes any other decay products of the new long-lived particle. When interpreting the results of the Displaced Leptons analysis with the Displaced SUSY model, $X$ refers to a top squark and $Y$ refers to a b or d quark. . . . .	53
3.3 Distribution of data (colors) and simulated Displaced SUSY events (black boxes) in the plane defined by electron $ d_0 $ and muon $ d_0 $ . The size of the black boxes are proportional to the bin content, and the bins along the x and y axes include underflow. All events are required to pass the $e\mu$ preselection defined in Section 3.3. . . . .	56
3.4 Comparison of the the muon isolation pileup correction term in the standard muon isolation and the modified muon isolation in simulated $t\bar{t}$ events that pass the 2018 $e\mu$ preselection. Muon $ d_0 $ is constrained to be less than 100 $\mu\text{m}$ in the plot on the left and between 500 and 1000 $\mu\text{m}$ in the plot on the right. . . . .	70
3.5 The distribution of $t\bar{t}$ simulated events in the plane defined by electron $ d_0 $ and muon $ d_0 $ . The standard isolation is applied in the plot on the left, and the modified isolation is applied in the plot on the right, and the events in both plots are required to pass the remaining 2018 $e\mu$ preselection criteria and the additional constraint that the parent of at least one lepton is a heavy-flavor meson. . . . .	71
3.6 The muon modified isolation distribution for simulated $t\bar{t}$ background and $\tilde{t}\tilde{t} \rightarrow \bar{l}b\bar{l}b$ signal events that pass the 2018 $e\mu$ preselection with no isolation criterion applied. . . . .	71

3.7	The electron $\eta$ - $\phi$ distribution in a prompt-muon, displaced-electron control region in 2017 (left) and 2018 (right) data before vetoing the regions affected by pixel power-supply issues. . . . .	72
3.8	The di-muon $\cos(\alpha)$ distribution of 2018 NoBPTX data and simulated $\tilde{t}\tilde{t} \rightarrow \bar{l}b\bar{l}b$ events (left) and the di-muon $\Delta t$ distribution in simulated cosmic-ray muon events in 2016 conditions (center) and $\tilde{t}\tilde{t} \rightarrow \bar{l}b\bar{l}b$ (right) events in 2018 conditions. In each case, all $\mu\mu$ preselection criteria except those relating to cosmic rejection are applied. . . . .	73
3.9	The electron (left) and muon (right) $ d_0 $ distributions for 2018 simulation events that pass the $e\mu$ preselection criteria. The upper two plots show $\tilde{t}\tilde{t} \rightarrow \bar{l}b\bar{l}b$ simulation for a single $\tilde{t}$ mass and four different proper decay lengths; each histogram is normalized to unity. The lower two plots show the background simulation normalized to the integrated luminosity. In all of the histograms, the last bin includes the overflow. All of the corrections from Section 3.4 are applied. . . . .	75
3.10	The cumulative number of simulated $\tilde{t}\tilde{t} \rightarrow \bar{l}b\bar{l}b$ events that pass each criterion in the 2018 $e\mu$ (top), $ee$ (middle), and $\mu\mu$ (bottom) preselection. Several $\tilde{t}$ proper decay lengths are shown. The jet criteria do not exclude any events and are simply an artifact of the analysis framework.	76
3.11	The electron (top) and muon (bottom) $p_T$ (left), $\eta$ (center), and $ d_0 $ (right) distributions in the $e\mu$ prompt control region for 2016 data and simulated background events. The rightmost bin in each plot contains the overflow entries. . . . .	77
3.12	The electron $p_T$ (left), $\eta$ (center), and $ d_0 $ (right) distributions in the $ee$ prompt control region for 2016 data and simulated background events. The rightmost bin in each plot contains the overflow entries. . . . .	78
3.13	The muon $p_T$ (left), $\eta$ (center), and $ d_0 $ (right) distributions in the $\mu\mu$ prompt control region for 2016 data and simulated background events. The rightmost bin in each plot contains the overflow entries. . . . .	78
3.14	The uncorrected lepton $ d_0 $ distributions in the $e\mu$ prompt control region, for electrons (left) and muons (right), for 2017 data and simulation (top), and 2018 data and simulation (bottom). The rightmost bin in each plot contains the overflow entries. . . . .	81

3.15 The average lepton $ d_0 $ as a function of $\phi$ in the $e\mu$ prompt control region, for electrons (left) and muons (right), for 2017 data and simulation.	82
3.16 The lepton $d_0$ distributions with Gaussian fits in the 2017 $e\mu$ prompt control region for (working from left to right) electrons in data, electrons in background simulation, muons in data, and muons in background simulation.	83
3.17 The lepton $d_0$ distributions with Gaussian fits in the 2018 $e\mu$ prompt control region for (working from left to right) electrons in data, electrons in background simulation, muons in data, and muons in background simulation.	83
3.18 The corrected lepton $ d_0 $ distributions in the $e\mu$ prompt control region, for electrons (left) and muons (right), for 2017 data and simulation (top), and 2018 data and simulation (bottom). The rightmost bin in each plot contains the overflow entries.	84
3.19 Trigger efficiency as a function of leading electron (left) or leading muon (right) $p_T$ in the $e\mu$ channel in 2016 (top), 2017 (middle), and 2018 (bottom) in data and simulated background $t\bar{t}$ events.	88
3.20 The fraction of electrons (left) and muons (right) from different parents as a function of lepton $ d_0 $ in simulated $t\bar{t}$ events that pass the 2018 $e\mu$ channel preselection. Note that the vast majority of leptons whose parent is a W boson are produced in prompt decays.	90
3.21 The fraction of muons from different parents as a function of muon $ d_0 $ in simulated Drell-Yan events that pass the 2018 $\mu\mu$ channel preselection and the additional constraint that the leading and subleading muon both come from the same type of parent particle.	92
3.22 A diagram of the ABCD method overlaid on simulated background events passing the 2018 $e\mu$ preselection. A, B, and C are control regions, and D corresponds to the inclusive SR, which includes SRs I, II, III, and IV. Underflow events are included in the bins along the left and bottom edges. When performing the background estimate, regions B and C are further subdivided to coincide with the SR for which the estimate is being performed.	93

3.23 Background estimation closure tests in data, in 100–500 $\mu\text{m}$ subregions of regions B (left) and C (right) in the $e\mu$ channel. Each plot shows the ratio of the actual to the estimated number of events as a function of the prompt lepton $ d_0 $ in 2016 (top) and 2017–18 (bottom). A linear fit is shown in black along with the 68 % and 95 % confidence intervals of the extrapolated fit value. . . . .	100
3.24 Background estimation closure tests in data, in 100–500 $\mu\text{m}$ subregions of regions B (left) and C (right) in the $ee$ channel. Each plot shows the ratio of the actual to the estimated number of events as a function of the prompt lepton $ d_0 $ in 2016 (top) and 2017–18 (bottom). A linear fit is shown in black along with the 68 % and 95 % confidence intervals of the extrapolated fit value. . . . .	101
3.25 Background estimation closure tests in data, in 100–500 $\mu\text{m}$ subregions of regions B (left) and C (right) in the $\mu\mu$ channel. Each plot shows the ratio of the actual to the estimated number of events as a function of the prompt lepton $ d_0 $ in 2016 (top) and 2017–18 (bottom). A linear fit is shown in black along with the 68 % and 95 % confidence intervals of the extrapolated fit value. . . . .	102
3.26 The di-muon invariant mass distribution in data and QCD multijet simulation events that pass the 2018 $\mu\mu$ preselection with the muon isolation criterion inverted. . . . .	108
3.27 The di-muon invariant mass distribution in data events that pass the 2018 $\mu\mu$ prompt control region (black), SR I (blue), and SR IV (red) criteria with the muon isolation and di-muon $\Delta R$ criteria inverted. The equivalent distribution in the prompt control region is also shown in green. . . . .	110
3.28 The pixel hit efficiency as a function of muon $ d_0 $ in simulated cosmic ray events and NoBPTX data in 2016 (left), 2017 (center), and 2018 (right) conditions. . . . .	116
3.29 The number of estimated background and observed events in each channel and SR, with a representative signal overlaid, for 2016 (top) and 2017–2018 (bottom). For each background estimate and signal yield, the total uncertainty is given. . . . .	119

3.30 The number of estimated background and observed events in each channel and SR, with a representative signal overlaid, for 2016–2018. For each background estimate and signal yield, the total uncertainty is given.	120
3.31 Two-dimensional distributions of $ d_0^a $ and $ d_0^b $ , for the events in data that pass the $e\mu$ (left), $ee$ (center), and $\mu\mu$ (right) preselection. The bins along the x and y axes contain underflow. The inclusive signal region covers the region between 100 $\mu\text{m}$ and 10 cm in each $ d_0 $ variable shown.	120
3.32 Two-dimensional distributions of $ d_0^a $ and $ d_0^b $ , for data events in the inclusive SR in the $e\mu$ (left), $ee$ (center), and $\mu\mu$ (right) channels.	121
3.33 Muon $\phi$ and di-muon invariant mass distributions for data and composite background simulation in the $\mu\mu$ channel in the inclusive SR. The background simulation is normalized to the ABCD method background prediction.	122
3.34 The 95% CL upper limits on the top squark mass ( $m_{\tilde{t}}$ ) as a function of its lifetime ( $c\tau$ ), for the $e\mu$ , $ee$ , and $\mu\mu$ channels. The $\tilde{t}\bar{t} \rightarrow \bar{l}b\bar{l}b$ (top) and $\tilde{t}\bar{t} \rightarrow \bar{l}d\bar{l}d$ (bottom) processes are shown.	124
3.35 The 95% CL upper limits on the top squark mass ( $m_{\tilde{t}}$ ) as a function of its lifetime ( $c\tau$ ). The colors indicate the observed 95% CL upper limit on the cross section. The $\tilde{t}\bar{t} \rightarrow \bar{l}b\bar{l}b$ (left) and $\tilde{t}\bar{t} \rightarrow \bar{l}d\bar{l}d$ (right) processes are shown.	125
3.36 The distribution of pulls for each signal region bin, where pulls are calculated as the difference between the post-fit background yield and the pre-fit background yield divided by the pre-fit background uncertainty (left). The distribution of pulls for each background nuisance parameter, where pulls are calculated as the difference between the post-fit value and the pre-fit value divided by the pre-fit uncertainty (right).	128
3.37 The observed asymptotic significances for the $\tilde{t}\bar{t} \rightarrow \bar{l}b\bar{l}b$ process as a function of $\tilde{t}$ mass and lifetime using the combined results.	129
3.38 The observed asymptotic significances for the $\tilde{t}\bar{t} \rightarrow \bar{l}b\bar{l}b$ process as a function of $\tilde{t}$ mass and lifetime in the $ee$ (left), $e\mu$ (center), $\mu\mu$ channels (right).	129

A.1 Transverse decay length distribution of reconstructed $K_S^0 \rightarrow \pi^+\pi^-$ candidates for various runs in 2016 (top left), 2017 (top right) and 2018 (bottom). The peak instantaneous luminosity of each run is indicated in the legend, and each distribution is normalized to the integrated luminosity of the run. In the 2016 plot, runs taken before (after) the APV25 saturation effect was mitigated are shown by solid (dashed) lines. In the 2017 plot, the run with lowest (highest) instantaneous luminosity examined in each data-taking era is plotted with a dashed (solid) line. Towards the end of 2017 (orange and black lines) the LHC ran with approximately 20% fewer proton bunches, meaning that the instantaneous luminosity per bunch crossing was higher than one might naively expect from the instantaneous luminosities shown in the legend.	136
B.1 The standard deviation of the leading muon $d_0$ as a function of the leading muon $\eta$ for simulated background events (left). To ensure that the variation in width is purely due to $d_0$ resolution effects, we use a sample of simulated Drell-Yan events from which the $Z \rightarrow \tau\tau \rightarrow ll$ events have been removed. Muon $\eta$ distribution for simulated $\tilde{t}\tilde{t} \rightarrow \bar{l}b\bar{l}\bar{b}$ events (right). The $\mu\mu$ preselection with a loosened $ \eta $ requirement is applied in both plots. . . . .	138
B.2 Electron $\eta$ distribution for simulated background events in which the electron parent particles are required to be SM mesons (left). Electron $\eta$ distribution for simulated $\tilde{t}\tilde{t} \rightarrow \bar{l}b\bar{l}\bar{b}$ events (right). The $e\mu$ preselection with a loosened $\eta$ requirement is applied in both plots. . . . .	138
C.1 Distribution of the arrival time of cosmic rays at their point of closest approach to the beamline as measured by the muon system in 2016 (left), 2017 (center), and 2018 (right) in data and simulation. Only cosmic-ray muons with $ d_0  < 8$ cm and $ z_0  < 20$ cm are considered. . . . .	143
C.2 Measured downward tracking efficiency versus cosmic ray muon arrival time in 2016 (left), 2017 (center), and 2018 (right) in data and simulation. Only cosmic-ray muons with $ d_0  < 8$ cm and $ z_0  < 20$ cm are considered. . . . .	143
C.3 Measured downward tracking efficiency in 2016 (top), 2017 (middle), and 2018 (bottom) versus $ d_0 $ (left) and $ d_z $ (right) in data and simulation. $ d_z $ ( $ d_0 $ ) impact parameter is constrained to less than 20 cm (1.2 cm) when plotting against $ d_0 $ ( $ d_z $ ). . . . .	145

## Chapter 1: Introduction

2 Particle physicists seek to understand the fundamental constituents of nature and  
3 their interactions. At the present moment, the Standard Model of particle physics  
4 (along with the general theory of relativity) represents the most complete understand-  
5 ing humanity has yet achieved. At the same time, the Standard Model cannot explain  
6 gravity or several observed but not yet understood aspects of nature and therefore  
7 must give way to a more complete theory at a higher energy scale. One approach  
8 to understanding what might be hiding beneath the Standard Model is to use high-  
9 energy particle collisions to probe nature at ever smaller length scales. This thesis  
10 presents a search for beyond the Standard Model physics in 13 TeV proton-proton col-  
11 lision data collected by the Compact Muon Solenoid experiment at the Large Hadron  
12 Collider, which is the highest-energy particle collider ever constructed.

13 The search presented in this thesis targets new long-lived particles that produce  
14 displaced leptons, a unique signature that could evade many existing searches for new  
15 physics. In this chapter, I present theoretical context in the form of a brief overview  
16 of the Standard Model and targeted discussion of beyond the Standard Model physics  
17 and long-lived particles. I then present the experimental context with an overview of  
18 the Large Hadron Collider and the Compact Muon Solenoid detector in Chapter 2,  
19 present the search itself in Chapter 3, and conclude in Chapter 4.

20 **1.1 The Standard Model**

21 The Standard Model of particle physics (SM) describes all known particles and  
22 their non-gravitational interactions. Developed and experimentally verified over the  
23 past six decades, the SM posits the existence of twelve spin- $\frac{1}{2}$  particles, the fermions,  
24 that make up all observed matter; twelve spin-1 particles, the gauge bosons, that  
25 communicate the electromagnetic, weak, and strong forces; and one fundamental  
26 scalar, the Higgs boson, which breaks electroweak symmetry, giving mass to the  
27 gauge bosons and fermions.

28 The fermions and gauge bosons can be classified according to the forces with  
29 which they interact. The fermions are divided into six quarks, which carry color and  
30 interact via the strong force, and six leptons, which do not. Furthermore, all six  
31 quarks and three of the leptons carry electric charge and interact electromagnetically.  
32 The charged leptons include the electron, muon, and tau, and the neutral leptons  
33 are called neutrinos. All fermions interact via the weak force. The gauge bosons in-  
34 clude the photon, which communicates the electromagnetic force; the  $W^+$ ,  $W^-$ , and  
35  $Z$  bosons, which communicate the weak force; and eight gluons that communicate the  
36 strong force. Of these, only the  $W^+$  and  $W^-$  bosons are electrically charged and only  
37 the gluons carry color charge. Finally, the fermions are grouped into three genera-  
38 tions, each with two quarks, one charged leptons, and one neutral lepton. Figure 1.1  
39 diagrams the grouping of the SM particles and lists some of their properties.

40 In the SM, the interactions between particles are governed by two theories: quan-  
41 tum chromodynamics, which describes the strong force, and the electroweak theory,  
42 which describes the electromagnetic and weak forces. The following sections provide  
43 a brief overview of these theories.

# Standard Model of Elementary Particles

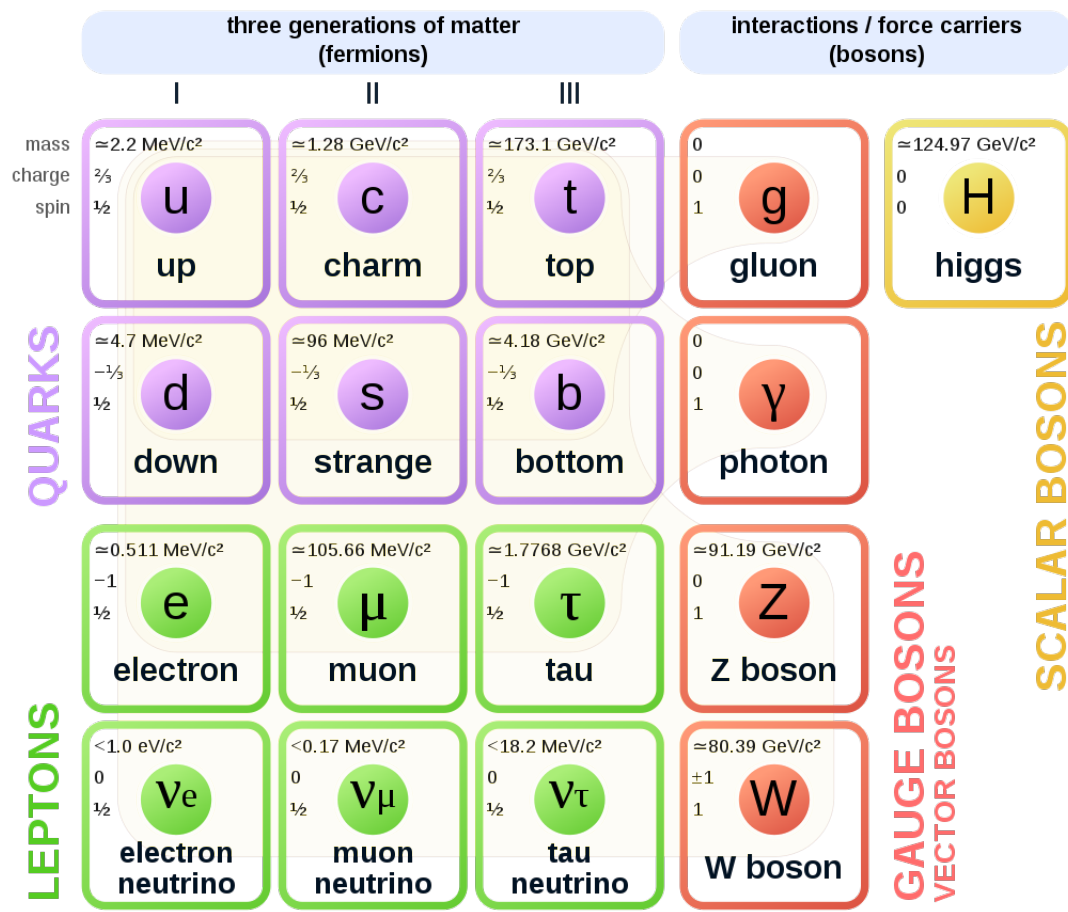


Figure 1.1: The Standard Model particle content.

<sup>44</sup> **1.1.1 Quantum chromodynamics**

<sup>45</sup> Quantum chromodynamics (QCD) describes the strong interactions between  
<sup>46</sup> quarks and gluons and is based on the  $SU(3)_c$  symmetry group, where the subscript c  
<sup>47</sup> refers to color charge. In QCD, all quarks and gluons carry color charge, which allows  
<sup>48</sup> interactions between two quarks of the same generation and a gluon, three gluons,  
<sup>49</sup> or four gluons. QCD is responsible for the formation of all hadrons (such as protons  
<sup>50</sup> and neutrons), and leads to two unique phenomena: confinement and asymptotic  
<sup>51</sup> freedom [17, 18].

<sup>52</sup> Confinement refers to the experimental fact that an isolated particle with color  
<sup>53</sup> charge has never been directly observed. Composite particles composed of quarks  
<sup>54</sup> and gluons are always neutral under color, and attempts to separate the constituent  
<sup>55</sup> particles will only produce new hadrons. This phenomenon is the result of the unique  
<sup>56</sup> running of the strong coupling constant, which increases with decreasing energy (and  
<sup>57</sup> therefore increasing distance).

<sup>58</sup> Asymptotic freedom is the other side of the coin: if the strong coupling constant  
<sup>59</sup> decreases as the interaction energy increases, then the strong interaction becomes  
<sup>60</sup> more and more feeble at high energies. In high energy interactions (such as those  
<sup>61</sup> at the Large Hadron Collider), the strong coupling constant is in fact small enough  
<sup>62</sup> to render the quarks nearly free. In this regime, perturbative calculations become  
<sup>63</sup> possible.

<sup>64</sup> **1.1.2 The electroweak theory**

<sup>65</sup> The electroweak theory unifies the electromagnetic and weak interactions and is  
<sup>66</sup> based on the  $SU(2)_L \otimes U(1)_Y$  symmetry group. It posits two new charges: weak

67 isospin, which has three components  $T_1$ ,  $T_2$ , and  $T_3$ , and hypercharge,  $Y$ .  $T_3$  is  $\pm\frac{1}{2}$  for  
 68 all left-handed fermions and 0 otherwise, while  $Y$  varies according to  $Q = T_3 + \frac{1}{2}Y$ ,  
 69 where  $Q$  is the familiar electric charge. Each generation of left-handed quarks or  
 70 leptons forms an SU(2) doublet. The first generation doublets, for example, are:

$$\begin{pmatrix} \nu_e \\ e^- \end{pmatrix}_L, \begin{pmatrix} u \\ d \end{pmatrix}_L \quad (1.1)$$

71 where, as in  $SU(2)_L$ , the L denotes left-handed chiral states. The three generators  
 72 of  $SU(2)_L$  result in three massless spin-1 bosons:  $W^1$ ,  $W^2$ , and  $W^3$ , while  $U(1)_Y$   
 73 gives rise to one massless spin-1 boson,  $B^0$ . After electroweak symmetry is broken  
 74 by the mechanism explained in the following subsection, the physical  $W^\pm$  bosons are  
 75 identified as superpositions of  $W^1$  and  $W^2$  while the Z boson and the photon are  
 76 identified as superpositions of  $W^3$  and  $B^0$  [19].

77 Terms in the electroweak Lagrangian involve either two left-handed fermions and a  
 78  $W^\pm$  or Z boson, two electrically charged particles and a photon, or charge-conserving  
 79 combinations of  $W^\pm$  bosons, Z bosons, and photons that include three or four par-  
 80 ticles. Conspicuously missing, however, are mass terms for the electroweak gauge  
 81 bosons or fermions.

### 82 **1.1.3 The Higgs mechanism**

83 As shown in Fig. 1.1, the fermions and  $W^\pm$  and Z bosons all have nonzero mass.  
 84 Accounting for this fact within the context of the electroweak theory is difficult be-  
 85 cause explicit mass terms violate the gauge and chiral symmetry of  $SU(2)_L \otimes U(1)_Y$ .  
 86 For example, a term such as

$$\frac{1}{2}m_A^2 A^\mu A_\mu, \quad (1.2)$$

<sup>87</sup> which assigns mass  $m_A$  to gauge boson  $A$ , becomes

$$\frac{1}{2}m^2(A^\mu - \partial^\mu\alpha)(A_\mu - \partial_\mu\alpha) \neq \frac{1}{2}m^2A^\mu A_\mu \quad (1.3)$$

<sup>88</sup> under a  $U(1)_Y$  gauge transformation, and a term such as

$$m_f\bar{f}f = m_f(\bar{f}_R f_L + \bar{f}_L f_R), \quad (1.4)$$

<sup>89</sup> which assigns mass  $m_f$  to fermion  $f$ , breaks chiral symmetry by coupling the right-  
<sup>90</sup> and left-handed components of the fermion.

<sup>91</sup> If the gauge and chiral symmetries of  $SU(3)_c \otimes SU(2)_L \otimes U(1)_Y$  truly are symmetries  
<sup>92</sup> of nature and the fermions and  $W^\pm$  and  $Z$  bosons truly have nonzero mass, then  
<sup>93</sup> another mechanism must be at work. Spontaneous symmetry breaking, which occurs  
<sup>94</sup> when the vacuum state does not exhibit all of the symmetries of the underlying  
<sup>95</sup> theory. In such a situation, each spontaneously broken continuous symmetry gives  
<sup>96</sup> rise to a massless scalar particle [20]. In the case of spontaneously broken continuous  
<sup>97</sup> *gauge* symmetries, however, there exists a mechanism by which the massless bosons  
<sup>98</sup> are removed and some of the gauge bosons associated with the generators of the  
<sup>99</sup> symmetries acquire mass [21, 22, 23]. In the SM, this mechanism, known as the  
<sup>100</sup> Higgs mechanism, breaks electroweak symmetry, gives mass to the fermions and  $W^\pm$   
<sup>101</sup> and  $Z$  bosons, and results in one massive scalar particle, the Higgs boson.

<sup>102</sup> The Higgs mechanism adds the scalar doublet

$$\Phi = \begin{pmatrix} \phi^+ \\ \phi^0 \end{pmatrix}, \quad (1.5)$$

<sup>103</sup> whose potential is given by

$$V(\Phi^\dagger\Phi) = \mu^2\Phi^\dagger\Phi + \lambda(\Phi^\dagger\Phi)^2, \quad (1.6)$$

104 to the SM. If  $\mu^2 < 0$  and  $\lambda > 0$ , then  $\Phi^\dagger \Phi = -\frac{\mu^2}{2\lambda}$  defines a circle of minima in the  
105  $\phi^+ - \phi^0$  plane. Even though the potential remains invariant under  $SU(2)_L \otimes U(1)_Y$ ,  
106 nature must spontaneously choose a vacuum state somewhere along this circle. Be-  
107 cause the vacuum state does not respect  $SU(2)_L \otimes U(1)_Y$ , the symmetry is said to be  
108 spontaneously broken.

109 This procedure has three significant consequences. First, three of the four degrees  
110 of freedom originally associated with  $\Phi$  are now associated with the longitudinal  
111 components of the  $W^\pm$  and  $Z$  bosons, which causes them to acquire mass while the  
112 photon remains massless. Second,  $\Phi$ 's remaining degree of freedom adds a single  
113 massive scalar, the Higgs boson, to the theory. Third, the interaction between the  
114 fermions and the nonzero vacuum state of the scalar field produces fermion mass  
115 terms that obey chiral symmetry.

#### 116 1.1.4 Current status

117 The SM is remarkably successful. It describes all known particles and their non-  
118 gravitational interactions, and it has passed countless experimental tests over the last  
119 several decades. Figure 1.2 gives an idea of the scale of this success by comparing  
120 theoretical predictions of SM production cross sections with measurements performed  
121 by the CMS experiment: theory and experiment agree across 41 different SM processes  
122 at 7, 8, and 13 TeV. In 2012, the CMS and ATLAS experiments independently  
123 discovered an approximately 125 GeV scalar particle with properties consistent with  
124 the SM Higgs boson [13, 24]. Further measurements in 7, 8, and 13 TeV proton-proton  
125 collisions at the Large Hadron Collider continue to agree with SM predictions of the  
126 Higgs boson properties [25, 26]. We finally have meaningful evidence as to the origin

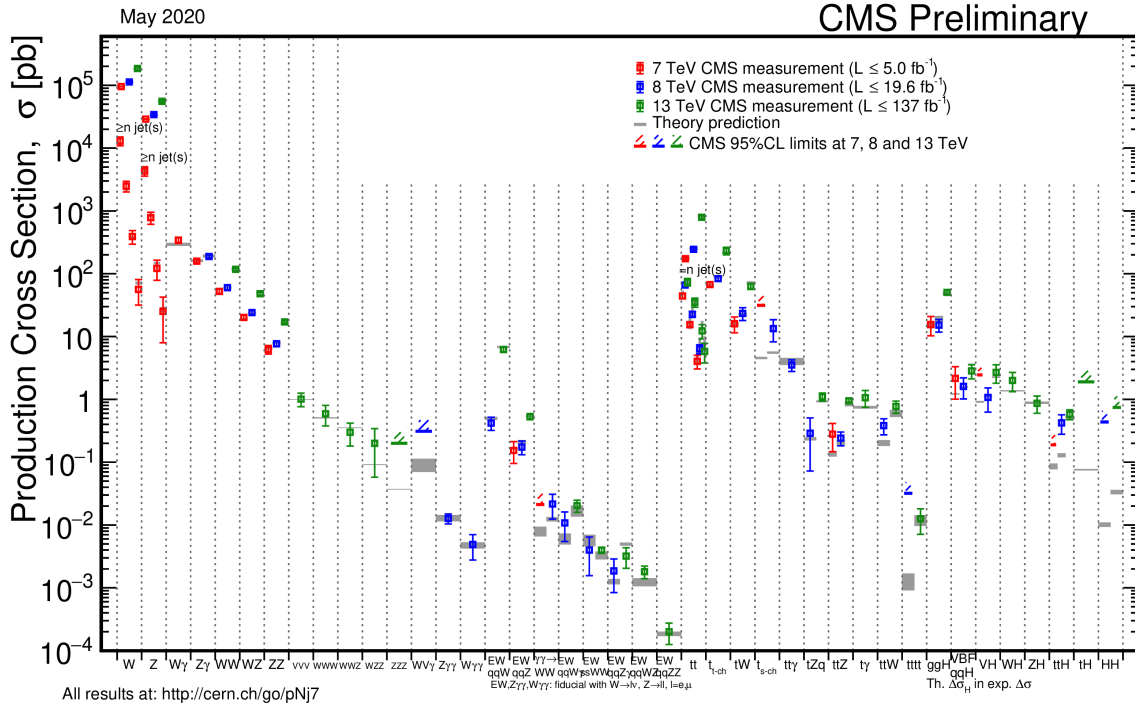


Figure 1.2: Summary of Standard Model production cross section measurements from the CMS experiment [2].

<sup>127</sup> of electroweak symmetry breaking, and all current evidence indicates that the SM  
<sup>128</sup> Higgs mechanism is indeed responsible.

Despite this remarkable success, the SM is not without problems. For one, it cannot be the whole story: it says nothing on the subjects of gravity, dark matter, or dark energy, which implies that it only describes about 5% of the energy content of the universe [27] and that a more complete theory must take over at or below the energy scale where gravity becomes important ( $M_P \approx 10^{19}$  GeV) [28]. Furthermore, many aspects of the SM seem arbitrary and unmotivated. It offers no explanation, for example, for why three generations of fermions are necessary or why its many parameters take the values they do. It could be that these unmotivated values are

137 simply experimental facts of nature without explanation, but the history of science  
138 implies that a deeper understanding is likely hiding beneath the surface. Finally, the  
139 observed value of the Higgs boson mass is not only unexplained, it is unnatural. This  
140 final issue, which is explained in the following paragraphs, is a powerful motivation  
141 to search for new physics at currently accessible energy scales.

142 **Naturalness**

143 The naturalness criterion states that an effective theory such as the SM must  
144 not be overly sensitive to the details of the underlying higher energy theory. Put  
145 another way, it requires that any dimensionless parameter much smaller than one  
146 must be protected by a custodial symmetry [29]. Such a criterion may or may not be  
147 respected by nature, but history and simple probability are on its side.

148 The dimensionless parameter in question is the mass of the Higgs boson, which is  
149 quadratically sensitive to  $\Lambda$ , the energy scale at which a new theory takes over. All SM  
150 parameters are affected by interactions with virtual particles through loop diagrams  
151 such as those shown in Fig. 1.3, but the Higgs boson mass is particularly sensitive. As  
152 a fundamental scalar, the Higgs boson lacks the chiral and gauge symmetries enjoyed  
153 by the fermions and gauge bosons. These symmetries, known as custodial symmetries,  
154 protect the fermion and gauge boson masses by guaranteeing that all corrections are  
155 proportional to the bare masses themselves. If the SM is indeed valid up to  $M_P$ ,  
156 then the bare mass of the Higgs boson must be coincidentally equal and opposite to  
157 the sum of the terms that correct it to approximately one part in  $10^{32}$  [28]. Such  
158 miraculous fine tuning is technically possible, but it could also be strong evidence  
159 that a deeper physical mechanism is at work.

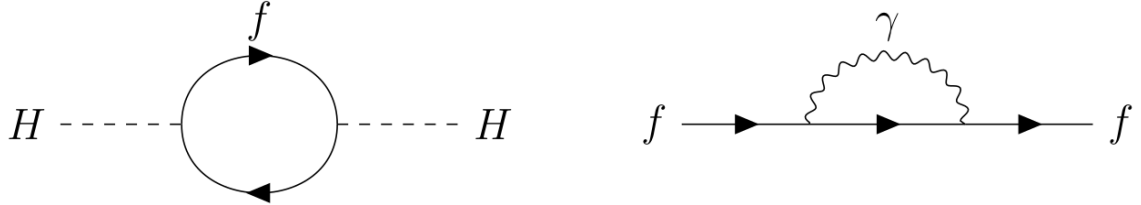


Figure 1.3: The Higgs boson mass corrected by a fermion loop (left) and a fermion mass corrected by photon loop (right).

## 160 1.2 Beyond the Standard Model

161 Many beyond the SM (BSM) theories have been proposed to address the issues  
162 discussed in Section 1.1.4. Theories such as large extra dimensions address the unnat-  
163 ural Higgs boson mass by allowing gravity to spread across more than three spatial  
164 dimensions, which lowers  $M_P$  and therefore the size of the Higgs boson mass correc-  
165 tions [30]. Other theories posit new symmetries that protect the Higgs boson mass  
166 from large corrections. The following section explains supersymmetry, which protects  
167 the Higgs boson mass with a new symmetry between bosons and fermions.

### 168 1.2.1 Supersymmetry

169 Supersymmetry (SUSY) introduces a new symmetry in which every SM particle  
170 fits into a larger multiplet with an inherent symmetry between bosons and fermions.  
171 In its simplest form, SUSY predicts one new boson for every SM fermion, one new  
172 fermion for every SM boson, and one new Higgs doublet. The increase in particle  
173 multiplicity necessitates a new naming convention: the spin-0 superpartners of the SM  
174 fermions are called sfermions (e.g. sleptons or squarks) while the spin- $\frac{1}{2}$  superpartners

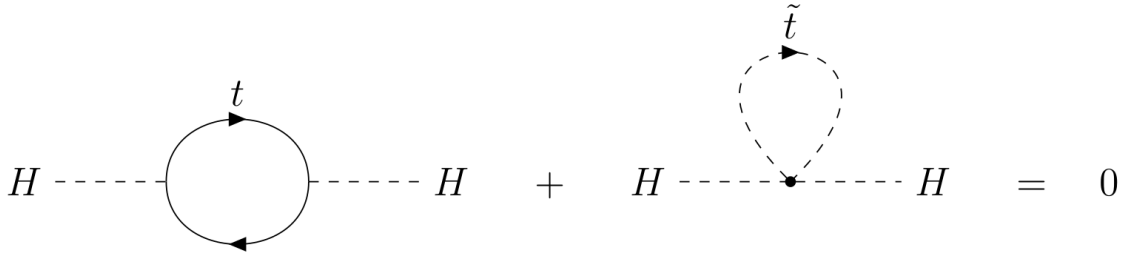


Figure 1.4: Corrections to the Higgs boson mass from the top quark (left) and top squark (right) cancel in exact SUSY. The top quark and top squark contributions are enhanced by the large coupling between the large Higgs-top quark coupling.

175 to the SM bosons add “ino” to the end of their SM counterpart (e.g. Higgsino or  
176 wino).

177 When calculating contributions to the Higgs boson mass from loop diagrams, one  
178 finds that fermion loops differ in sign from boson loops, which means that in SUSY  
179 every bosonic correction to the Higgs boson mass is cancelled by a fermionic correction  
180 and vice versa. If SUSY were an exact symmetry of nature, the cancellation would  
181 be perfect, and the observed Higgs boson mass would match the bare Higgs boson  
182 mass exactly [31]. Figure 1.4 shows a sample leading-order cancellation.

183 Exact SUSY also requires that SUSY particles have the same mass as their SM  
184 counterparts, so the uniformly null results in collider searches imply that if SUSY  
185 exists, it must be a broken symmetry. In broken SUSY, the diagrams in Fig. 1.4 no  
186 longer exactly cancel. Instead, the resulting correction is proportional to the mass of  
187 the top squark [32], which means that broken SUSY can still resolve the naturalness  
188 problem if the masses of the SUSY particles that correct the Higgs boson mass are  
189 themselves approximately at the weak scale (say  $\mathcal{O}(250 \text{ GeV})$ ). Many natural SUSY  
190 scenarios are therefore excluded as collider experiments set increasingly large lower

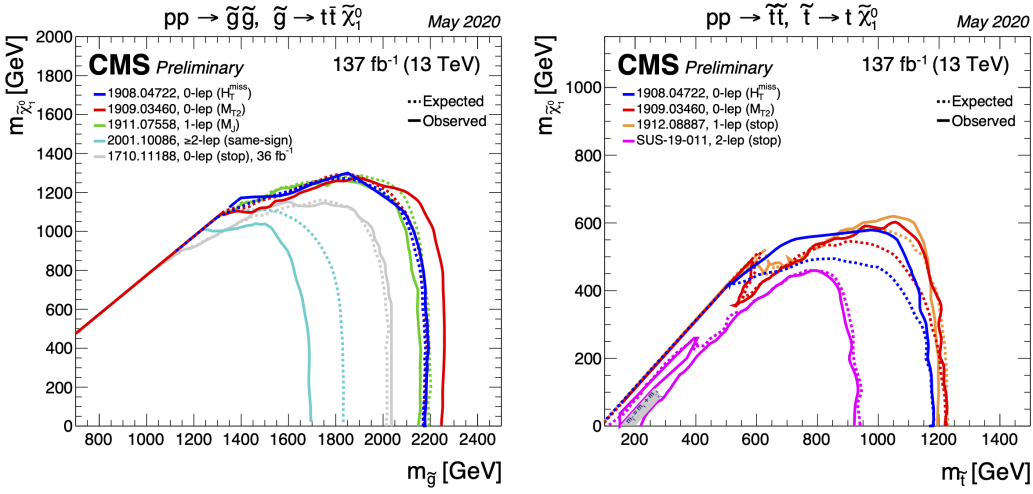


Figure 1.5: Mass limits at 95 % CL for a simplified model of gluino pair production with gluino decays to pairs of top quarks and the LSP (left) and top squark pair production with squark decays to a top quark and the LSP (right) from several CMS analyses [3].

<sup>191</sup> bounds on SUSY particle masses. Figure 1.5, for example, shows that the exclusion  
<sup>192</sup> bounds on top squark and gluino masses extend above 1 TeV in several recent CMS  
<sup>193</sup> analyses.

<sup>194</sup> As the available natural SUSY parameter space is further constricted, it is im-  
<sup>195</sup> portant to investigate signatures of new physics that conventional analyses may be  
<sup>196</sup> missing. One possibility, new long-lived particles, is presented in the following section.

### <sup>197</sup> 1.2.2 Long-lived particles

<sup>198</sup> In the context of collider physics, long-lived particles (LLPs) are particles whose  
<sup>199</sup> lifetimes are such that they decay a measurable distance from the collision point. This  
<sup>200</sup> category includes everything from particles that decay less than 1 mm away from the

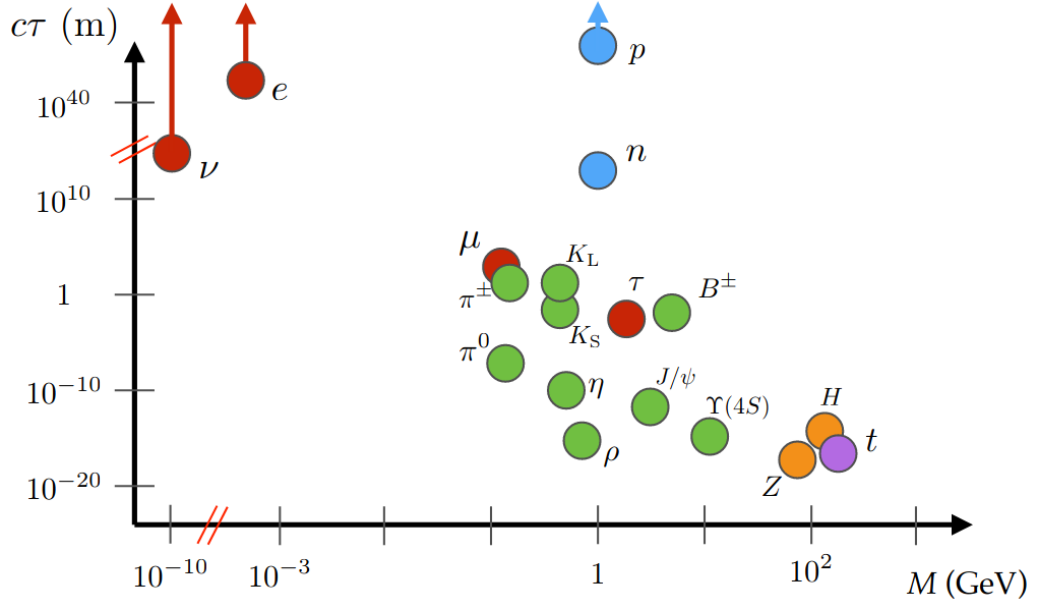


Figure 1.6: Masses and proper decay lengths of many Standard Model particles. Particles with proper decay lengths above approximately  $10^{-4}$  m will be noticeably long-lived in collider detectors such as CMS [4].

201 collision to particles that propagate through the entire detector. As shown in Fig 1.6,  
 202 LLPs are common in the SM.

203 Long-lived SM particles arise from several mechanisms. First, symmetries such as  
 204 charge and baryon number conservation ensure that particles such as electrons and  
 205 protons are absolutely stable. Second, small coupling constants and highly virtual  
 206 intermediate states decrease the decay rate of particles such as muons, whose  $2.2\ \mu\text{s}$   
 207 lifetime is the product of a weak decay through a virtual W boson (the W boson mass  
 208 is about 760 times that of the muon). Finally, limited decay phase space increases  
 209 the lifetime of particles such as the neutron, whose decay into a proton, an electron,  
 210 and an electron neutrino is slowed by the near mass degeneracy of the neutron and

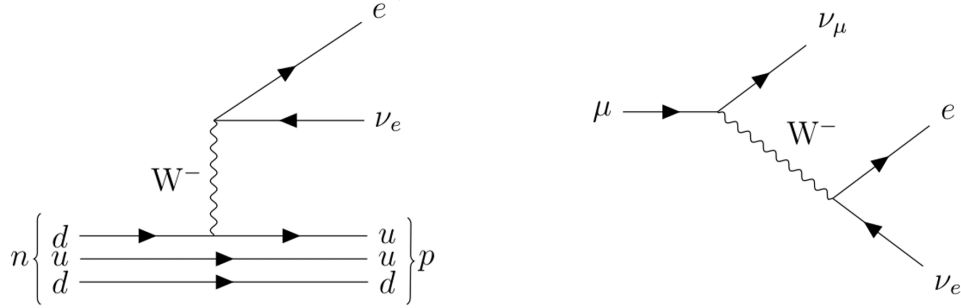


Figure 1.7: Long-lived decays of the neutron (left) and muon (right).

the proton. The mass difference between the neutron and its decay products is less than 1 MeV. The muon and neutron decays are diagrammed in Fig. 1.7.

In BSM physics, the same fundamental mechanisms could very well produce new LLPs. Many SUSY scenarios, for example, introduce a symmetry known as R-parity that prevents proton decay. In models with exact R-parity conservation, SM particles are assigned R-parity 1 and SUSY particles are assigned R-parity  $-1$ . Conserving the product of R-parity at each vertex has two phenomenological consequences: SUSY particles must be produced in pairs, and the lightest SUSY particle (LSP) must be absolutely stable. A neutral, weakly interacting LSP would therefore pass through most detectors (including the CMS detector described in Section 2.2) without interacting. The resulting momentum imbalance is a standard signature in many SUSY searches [33].

On the other hand, SUSY models with weakly coupled R-parity-violating (RPV) terms produce long-lived but not perfectly stable LSPs. The following section will give a detailed overview of one such model. A similar situation arises in gauge-mediated SUSY breaking models where the gravitino is the LSP. The strength of the

227 coupling between the next-to-LSP (NLSP) and the gravitino is inversely proportional  
228 to the energy scale at which SUSY is broken. A high SUSY breaking scale therefore  
229 suppresses the NLSP decay rate, making it long lived [34].

230 LLPs also arise from particular SUSY mass spectra. Models in the Split SUSY  
231 paradigm, for example, propose that the spin-0 SUSY particles are significantly more  
232 massive than the spin- $\frac{1}{2}$  SUSY particles. In these models, the gluino becomes long  
233 lived when its decay to two quarks and a neutral spin- $\frac{1}{2}$  SUSY particle is suppressed  
234 by a highly virtual intermediate squark [35]. Other SUSY models produce LLPs  
235 by limiting decay phase space. Some anomaly-mediated SUSY breaking models, for  
236 example, predict that the NLSP and LSP are nearly degenerate in mass. Just like  
237 the neutron decaying into a proton, the lack of available phase space suppresses the  
238 decay and produces a long-lived NLSP [36].

239 In summary, LLPs are a general feature of the SM, and it is reasonable to assume  
240 that the same mechanisms that produce SM LLPs will also manifest in BSM physics.  
241 The following subsection gives an overview of the phenomenology of the SUSY model  
242 most relevant to the analysis presented in Chapter 3, while the experimental details  
243 of this model and LLP searches at the Large Hadron Collider will be saved until after  
244 describing the Large Hadron Collider and the CMS experiment in Chapter 2.

### 245 1.2.3 Displaced supersymmetry

246 As mentioned in Section 1.2.1, weak-scale SUSY has the potential to explain the  
247 seemingly unnatural observed value of the Higgs boson mass. With this appealing  
248 outcome in mind, experimental physicists have been searching for signs of SUSY  
249 in high-energy particle collisions for the last few decades. In particular, searches

250 at the Large Hadron Collider, where the 7, 8, and 13 TeV proton-proton collisions  
 251 could potentially be producing SUSY particles with masses above 1 TeV, are actively  
 252 excluding large swaths of the natural SUSY parameter space. By examining the  
 253 common assumptions behind a majority of these searches, the proponents of the  
 254 Displaced SUSY model find an approach that avoids proton decay constraints while  
 255 naturally producing long-lived SUSY particles that would be undetected by most  
 256 collider searches [37].

257 Displaced SUSY is an RPV SUSY model that respects proton lifetime constraints  
 258 by allowing terms that violate lepton number but not baryon number. The Minimal  
 259 Supersymmetric Standard Model, which is a simple supersymmetric extension of the  
 260 SM, allows the following baryon and lepton violating operators:

$$\frac{1}{2}\lambda''_{ijk}U_iD_jD_k, \frac{1}{2}\lambda'_{ijk}L_iL_jE_k, \lambda'_{ijk}L_iQ_jD_k, \epsilon_iL_iH_u \quad (1.7)$$

261 where the first term violates baryon number and the remaining terms violate lepton  
 262 number. The  $i$ ,  $j$ , and  $k$  indices run over the three generations of fermions and  
 263  $U$ ,  $D$ ,  $L$ ,  $E$ ,  $Q$ , and  $H$  refer to the SUSY multiplets whose SM components are  
 264 right-handed up-type quarks, right-handed down-type quarks, left-handed leptons,  
 265 right-handed leptons, left-handed quarks, and Higgs bosons, respectively [31]. Most  
 266 SUSY models introduce R-parity to forbid all of these terms and therefore disallow  
 267 proton decay, but this approach may be overkill: separately conserving either lepton  
 268 number or baryon number is sufficient to prevent proton decay.

269 Such a situation can arise naturally if a gauge-unifying, R-parity-conserving  $SU(5)$   
 270 theory exists at high energies but is broken at lower energies [38]. In this scenario, the  
 271 baryon-number-violating terms are suppressed and mixing between  $L$  and  $H$  becomes  
 272 possible. The final term in expression (1.7) then dominates, and we are left with the

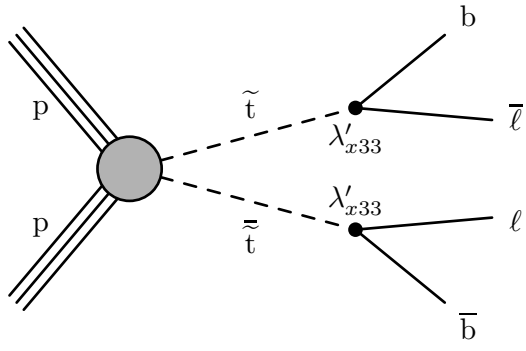


Figure 1.8: Pair-produced top squarks that each decay to a bottom quark and a lepton through an R-parity-violating  $LQD$  vertex.

<sup>273</sup> following lepton-number-violating terms after rotating to the mass basis:

$$\epsilon_i y_{jk}^d L_i Q_j D_k, \quad \epsilon_i y_{jk}^e L_i L_j E_k \quad (1.8)$$

<sup>274</sup> where the  $\epsilon$  factors are lepton-Higgs mixing angles and the  $y$  factors are the Yukawa  
<sup>275</sup> coupling constants associated with the interactions between the fermions and the SM  
<sup>276</sup> Higgs field. Because these  $y$  factors are proportional to fermion mass, the lepton-  
<sup>277</sup> violating processes will favor third-generation fermions.

<sup>278</sup> The dimensionless lepton-Higgs mixing angles are protected by the custodial R-  
<sup>279</sup> parity conservation of the higher-energy theory and will therefore naturally be small.  
<sup>280</sup> Just as in the SM, these small coupling constants can lead to macroscopic SUSY  
<sup>281</sup> particle lifetimes that would evade most collider searches. In particular, long-lived  
<sup>282</sup> LSP squarks can decay to a quark and charged lepton though a displaced vertex, as  
<sup>283</sup> in Fig. 1.8.

<sup>284</sup> The unique experimental signature of processes such as the one shown in Fig. 1.8 is  
<sup>285</sup> a major motivating factor behind the analysis presented in Chapter 3. The particular  
<sup>286</sup> experimental consequences of such processes will be further explored in that context.

287 **Chapter 2: The Large Hadron Collider and Compact Muon  
288 Solenoid experiment**

289 **2.1 The Large Hadron Collider**

290 The Large Hadron Collider (LHC) is the highest-energy particle collider ever con-  
291 structed. Located at the European Organization for Nuclear Research (CERN) and  
292 housed in a 27 km ring approximately 100 m below the French/Swiss countryside, the  
293 LHC is designed to accelerate two counter-rotating beams of protons to 7 TeV (and  
294 sometimes beams of heavy ions to 2.8 TeV) and collide them at four points around  
295 the ring. Each collision point is instrumented with a dedicated detector: the ATLAS  
296 (A Toroidal LHC ApparatuS) and CMS (Compact Muon Solenoid) experiments are  
297 general purpose detectors designed to reconstruct the remnants of proton-proton col-  
298 lisions at the highest collision rates offered by the LHC, LHCb (LHC beauty) studies  
299 b-quark decays from proton-proton collisions produced at lower collision rates, and  
300 ALICE (A Large Ion Collider Experiment) studies heavy-ion collisions [5]. Figure 2.1  
301 shows the location of each experiment around the LHC ring. The analysis presented  
302 in Chapter 3 utilizes proton-proton collision data collected by the CMS experiment,  
303 and the following discussion is focused accordingly.

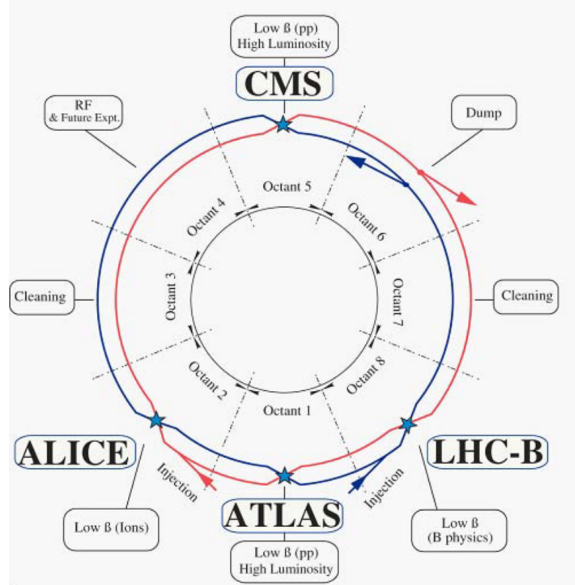


Figure 2.1: Layout of the LHC experiments [5].

### **2.1.1 Injection chain**

The protons ultimately collided by the LHC must first travel through much of the CERN accelerator complex, which is diagrammed in Fig. 2.2. The 6.5 TeV proton beams relevant to this thesis start their journey as the nuclei of hydrogen atoms in a bottle of hydrogen gas. After having their electrons stripped away with an electric field, the protons are accelerated to an energy of 50 MeV with the Linac 2 linear accelerator [39]. The Proton Synchrotron Booster (PSB) next accelerates the protons to an energy of 1.4 GeV before injecting them into the Proton Synchrotron (PS) [40]. The PS was the first synchrotron constructed at CERN and was the highest-energy particle accelerator in the world at the time of its first operation [41]. Today, it accelerates protons to an energy of 25 GeV before passing them along to the Super Proton Synchrotron (SPS), which is the 7 km proton-antiproton collider at which the

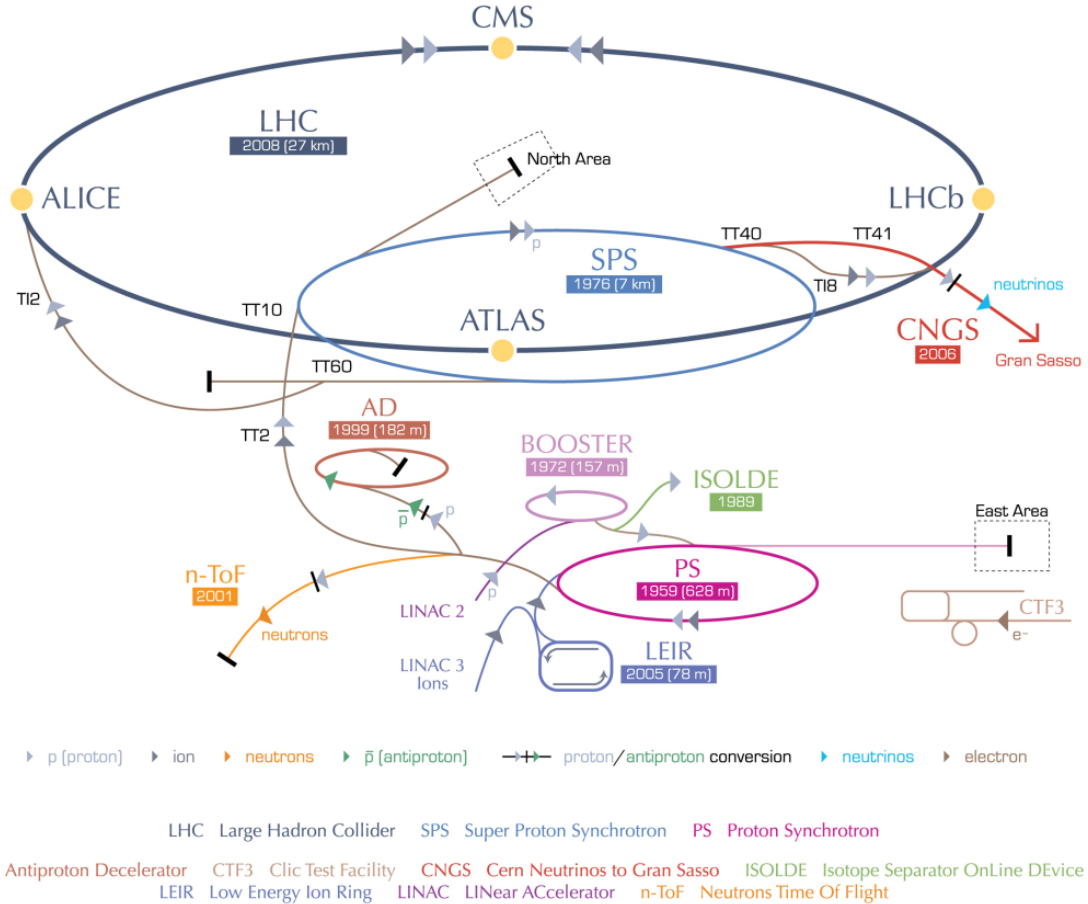


Figure 2.2: A diagram of the CERN accelerator complex. The analysis presented in Chapter 3 utilizes protons accelerated by LINAC 2, BOOSTER (also known as PSB), PS, SPS, and finally the LHC before their ultimate collision inside CMS [6].

<sub>316</sub>  $W^\pm$  and  $Z$  bosons were discovered in 1983 [42]. As the final step in the LHC injection  
<sub>317</sub> chain, SPS accelerates protons to an energy of 450 GeV before injecting them into  
<sub>318</sub> the LHC [5].

### <sub>319</sub> 2.1.2 Main ring

<sub>320</sub> Maximizing the physics potential of the LHC requires simultaneously maximizing  
<sub>321</sub> the collision energy and the number of interesting collisions per unit time. The main

Table 2.1: Luminosity parameters used in Eq. (2.1).

Parameter	Description
$N_b$	Number of particles per bunch
$n_b$	Number of bunches per beam
$f_{rev}$	Revolution frequency
$\gamma_r$	Relativistic gamma factor
$\epsilon_n$	Normalized transverse beam emittance
$\beta^*$	Beta function at collision point
$F$	Geometric luminosity reduction factor

322 LHC ring is therefore designed to accelerate the 450 GeV protons it receives from  
 323 SPS to 7 GeV and collimate them into intense beams to be collided at high rates.  
 324 The number of interesting collisions per unit time is ultimately the product of the  
 325 total cross section of the processes one deems interesting,  $\sigma$ , and the instantaneous  
 326 luminosity,  $L$ , which is given by:

$$L = \frac{N_b^2 n_b f_{rev} \gamma_r}{4\pi \epsilon_n \beta^*} F \quad (2.1)$$

327 where the parameters are defined as in Table 2.1 [5].

328 The LHC is designed to deliver a maximum instantaneous luminosity of  
 329  $10^{34} \text{ cm}^{-2} \text{ s}^{-1}$  to ATLAS and CMS, but operational improvements, most notably a  
 330 reduction in  $\epsilon_n$  and  $\beta^*$ , have allowed the LHC to exceed this goal by up to a factor of  
 331 approximately two in the 2016, 2017, and 2018 data-taking periods [7]. As shown in  
 332 Fig. 2.3, the total integrated luminosity delivered during this period is approximately  
 333 a factor of five times greater than that of the 2011–2012 period.

334 Increasing the number of interesting collisions per unit time comes with the unfor-  
 335 tunate side effect of increasing the total number of collisions in each bunch crossing.  
 336 Due to storage and processing limitations, the CMS and ATLAS detectors only record

337 data from the small subset of bunch crossings whose properties imply that they may  
338 contain interesting processes (see Section 2.2.6). In a given bunch crossing, usually  
339 only one collision is considered interesting. The remaining collisions, referred to as  
340 “pileup”, add a layer of difficulty to collecting and analyzing the data while increasing  
341 the total radiation dose that the detectors must withstand.

342 The ability to produce high-energy proton collisions at such high rates depends  
343 on several impressive technological feats, notably the superconducting magnets that  
344 steer and shape the beams and the superconducting radio-frequency (RF) cavities  
345 that accelerate the protons and determine their bunch structure.

### 346 **Superconducting magnets**

347 The LHC magnet system relies on superconducting NbTi magnets that are cooled  
348 to below 2 K with superfluid helium and are capable of producing fields in excess of  
349 8 T. The design of the main dipole magnets that are responsible for keeping the beams  
350 in a circular trajectory is heavily influenced by the size of the LHC tunnel, which orig-  
351 inally housed the Large Electron-Positron Collider (LEP). Unlike LEP, which collided  
352 particles and antiparticles, the LHC requires two separate beam pipes, each with its  
353 own dipole magnetic field. This requirement, along with the limited tunnel cross  
354 section, motivates the “two-in-one” magnet design in which both superconducting  
355 magnets share a common cold mass and cryostat, as shown in Fig. 2.4 [5].

356 In addition to the main dipole magnets, the LHC also employs quadrupole magnets  
357 for beam focusing and sextupole, octupole, and decapole magnets to correct the field  
358 at the edges of the dipoles [5].

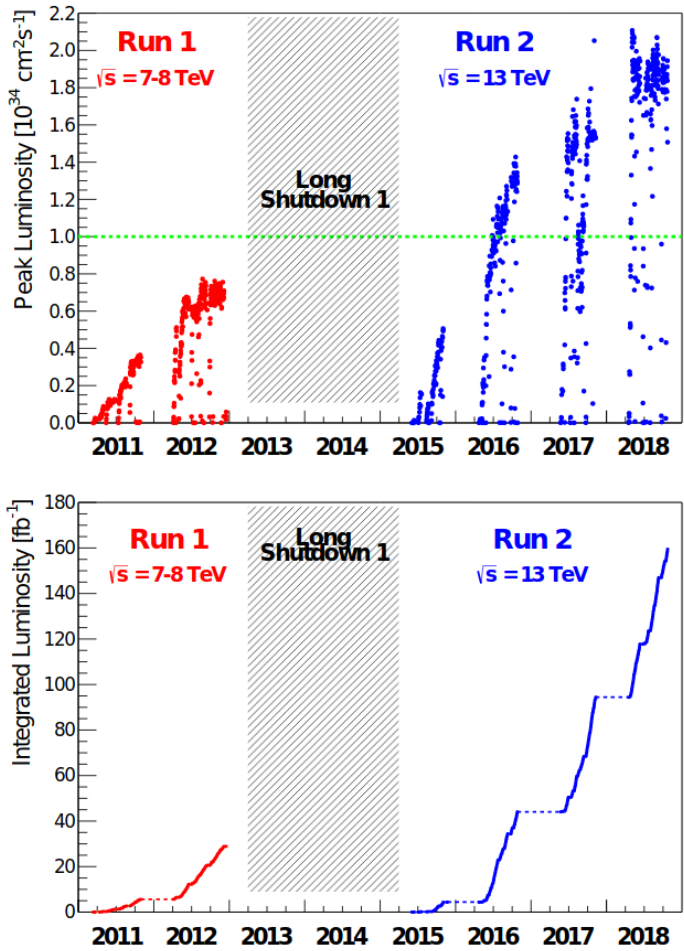


Figure 2.3: The peak instantaneous (top) and integrated (bottom) luminosity delivered by the LHC during proton operation between 2011 and 2018 [7].

## LHC DIPOLE : STANDARD CROSS-SECTION

CERN AC/DI/MM - HE107 - 30.04.1999

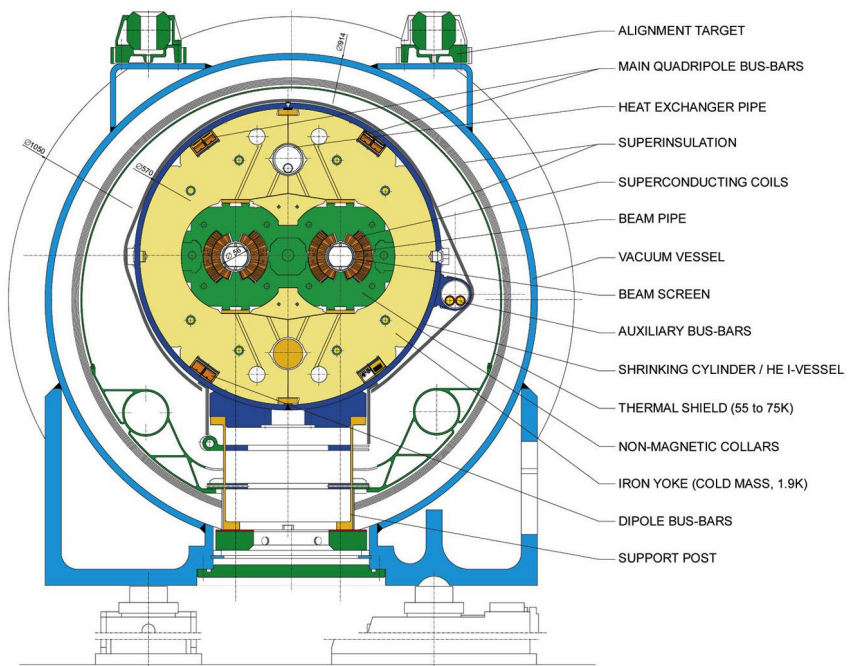


Figure 2.4: Diagram of an LHC dipole magnet in cross-section [8].

359 **Radio-frequency cavities**

360 An RF superconducting cavity system is responsible for capturing the 450 GeV  
361 protons injected into the LHC from SPS, accelerating them to the full collision energy,  
362 defining their bunch structure, and storing them. The main RF system operates  
363 at 400 MHz and is located in Octant 4 (see Fig.2.1). Each RF cavity contains an  
364 oscillating electromagnetic field whose phase is synchronized with the arrival of the  
365 proton bunches such that the protons passing through the cavity always feel a force  
366 in the direction of their motion. The applied force naturally varies for protons that  
367 are slightly out of phase in such a way as to keep the protons tightly bunched in the  
368 longitudinal direction [5].

## **369    2.2 The Compact Muon Solenoid experiment**

**370**       The Compact Muon Solenoid experiment (CMS) is designed for the general study  
**371**       of the highest-energy, highest-luminosity proton-proton (and heavy ion) collisions the  
**372**       LHC can provide. The detector design is driven by the particular goals of explor-  
**373**       ing physics at the TeV scale and discovering the origin of electroweak symmetry  
**374**       breaking [43]. More than 4000 collaborators from institutions across more than forty  
**375**       countries work together to collect and analyze the data using a global computing  
**376**       grid [44].

**377**       To reconstruct the variety of particles that emerge from high-energy proton-proton  
**378**       collisions, CMS uses several complimentary subdetectors nested radially about the  
**379**       collision point. A 4 T superconducting solenoid magnet provides a powerful magnetic  
**380**       field to bend the trajectories of charged particles, thus enabling the determination  
**381**       of their momenta. Working from the center out, the CMS detector consists of an  
**382**       all-silicon tracker, a lead-tungstate scintillating crystal electromagnetic calorimeter,  
**383**       a sampling hadronic calorimeter composed of brass absorber and plastic scintillator  
**384**       tiles, the superconducting solenoid magnet, and a muon system with three varieties  
**385**       of gaseous detectors. Figure 2.5 shows the detector layout, and the remainder of this  
**386**       chapter is devoted to a brief overview of each subsystem as well as the triggering and  
**387**       reconstruction strategies employed by CMS.

**388**       CMS uses a right-handed coordinate system centered on the nominal collision  
**389**       point with positive  $x$  direction pointing towards the center of the LHC ring and the  
**390**       positive  $y$  direction pointing vertically upward. The azimuthal angle in the  $x$ - $y$  plane,  
**391**       denoted  $\phi$ , is measured from the positive  $x$  axis, and the polar angle  $\theta$  is measured  
**392**       from the positive  $z$  axis. The angle from the  $z$  axis is more commonly described

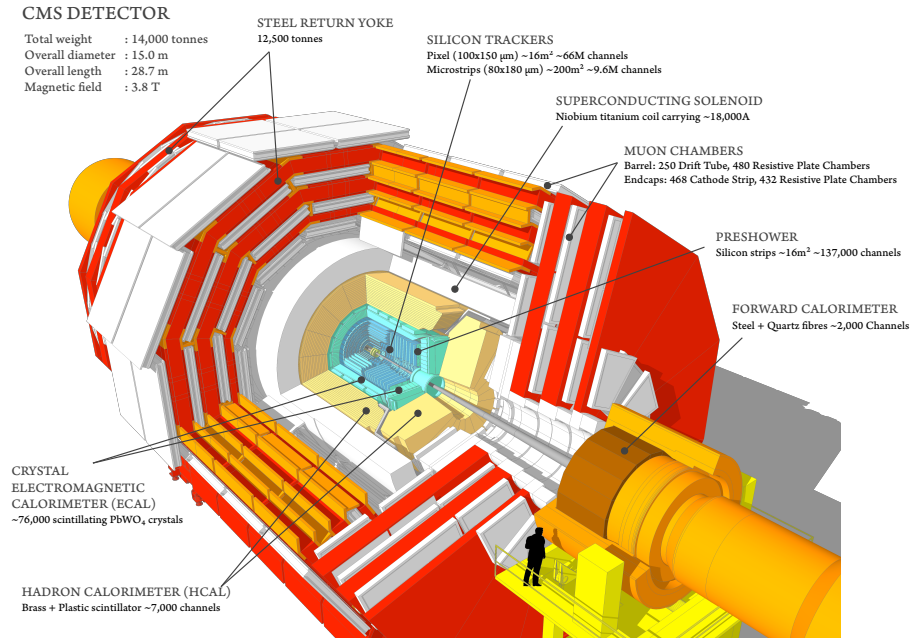


Figure 2.5: The CMS detector [9].

393 in terms of the pseudorapidity  $\eta = -\ln \tan(\theta/2)$ . Distances in the  $\eta$ - $\phi$  plane are  
 394 commonly referred to as  $\Delta R = \sqrt{(\Delta\eta)^2 + (\Delta\phi)^2}$ . The component of the momentum  
 395 that is transverse to the beam direction (i.e., in the  $x$ - $y$  plane) is denoted  $p_T$ , and  
 396 the magnitude of the negative vector sum of the  $p_T$  of all the reconstructed particles  
 397 in an event is denoted  $p_T^{\text{miss}}$ . The magnitude of  $p_T$  is also sometimes referred to as  
 398 transverse energy or  $E_T$  [14, 10].

399 The CMS detector has undergone several upgrades since its initial construction.  
 400 The description presented here will focus on the detector conditions relevant to the  
 401 analysis presented in Section 3.

402    **2.2.1 Solenoid magnet**

403       The superconducting solenoid is designed to produce a 4 T magnetic field through-  
404      out the 6.3 m diameter, 12.5 m long cylindrical volume that contains the tracker and  
405      calorimeters. The magnetic field is produced by running 19 kA through 2168 turns  
406      of NbTi superconducting cable that are cooled with liquid helium. The flux returns  
407      through an iron yoke that also houses the muon system [10].

408       The strong magnetic field is critical to CMS’s ability to unambiguously distinguish  
409      muons and anti-muons with transverse momenta up to 1 TeV [14], and much of the  
410      overall detector design is guided by the choice of a large superconducting solenoid.  
411      The uniform magnetic field alters the trajectories of charged particles immediately  
412      upon their production, which results in significant bending power within a relatively  
413      small radius and therefore enables a compact detector.

414       The CMS solenoid stores a uniquely large amount of energy in its magnetic field  
415      when compared to other collider detector magnets, especially when viewed relative to  
416      its mass. To avoid deformations from the strong magnetic field, the superconducting  
417      coils are reinforced with an aluminium alloy so that the coil layers themselves han-  
418      dle 70% of the magnetic hoop stress. Figure 2.6 compares several collider detector  
419      magnets in the energy/mass vs energy plane and shows a cross-sectional view of the  
420      reinforced conductor coils in cross section. This approach allows for a relatively thin  
421      solenoid that is less likely to scatter muons before they reach the muon system [10].

422    **2.2.2 Tracker**

423       In the region closest to the proton collisions, CMS employs a silicon tracker to re-  
424      construct particle trajectories along with primary and secondary vertices. Efficiently

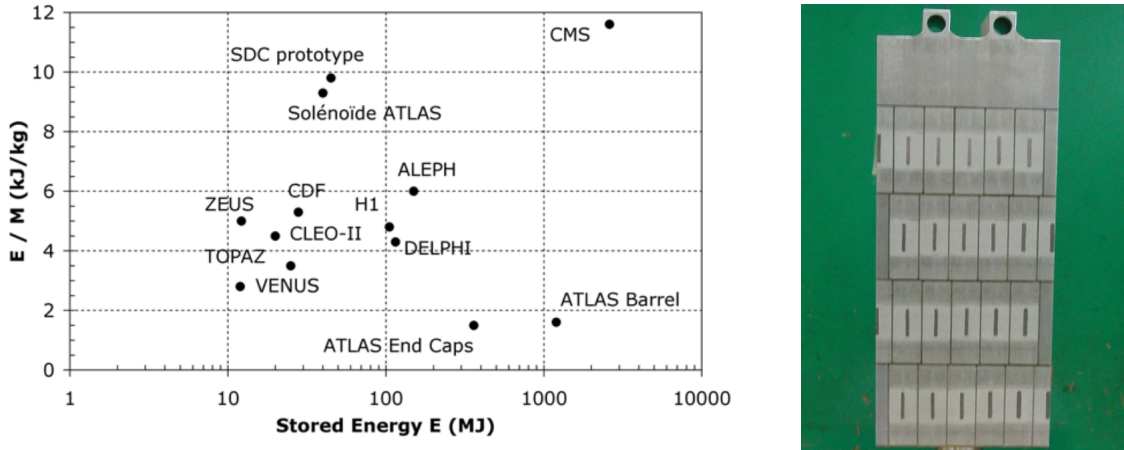


Figure 2.6: The stored-energy-over-mass ratio,  $E/M$ , for several detector magnets (left), and a cross-sectional view of the four-layer winding of reinforced conductor in the CMS superconducting solenoid (right) [10].

and accurately performing these tasks allows CMS to measure charged particle momenta, distinguish between particles from the primary and pileup vertices, and identify heavy-flavor decays. The high particle flux necessitates a highly granular, fast, and radiation hard detector that introduces the smallest possible amount of material to the region inside the calorimeters. The resulting detector contains over  $200\text{ m}^2$  of active silicon, making it the largest silicon tracker ever built. The tracker has a length of 5.8 m, a diameter of 2.5 m, and is divided into two subdetectors. Inside a radius of 20 cm, the particle flux demands the use of silicon pixel detectors, while silicon micro-strip detectors suffice in the region beyond 20 cm [10].

The pixel and strip detectors both utilize the same fundamental detection mechanism: the energy depositions of incident charged particles form electron-hole pairs when passing through the depletion region of a reverse-biased p-n junction, and the resulting induced current signifies the presence of a charged particle. The reverse bias

438 voltage sweeps away charge carriers to reduce thermal noise and maximize the sen-  
439 sitive volume. The fine two-dimensional segmentation of the pixel detector provides  
440 precise two-dimensional position measurements from a single detector layer, while  
441 each strip detector layer only provides a one-dimensional location measurement. In  
442 both cases, the detector planes are tilted to allow the charge liberated by a single  
443 incident particle to spread across multiple pixels or strips. This scheme significantly  
444 improves the position resolution by combining the charge measurements of multiple  
445 adjacent pixels or strips.

446 The original pixel detector was replaced between the 2016 and 2017 data-taking  
447 periods in preparation for higher luminosities [12]. As the analysis presented in Sec-  
448 tion 3 uses data collected in 2016–2018 and is particularly dependent on tracker  
449 measurements, the original pixel detector, 2017–2018 (Phase-1) pixel detector, and  
450 strip detector are described separately below.

#### 451 **Original pixel detector**

452 The original CMS pixel detector covers the  $|\eta| < 2.5$  region and is composed of  
453 three cylindrical barrel layers at  $r = 4.4$ , 7.3, and 10.2 cm and four endcap disks  
454 34.5 and 46.5 cm up and down the beamline from the nominal collision point. Each  
455 layer or disk is instrumented with several pixel modules that are each composed  
456 of a silicon sensor bump bonded to custom ASIC read-out chips (ROCs). Each  
457 sensor is 285  $\mu\text{m}$  thick and typically comprises 66 560  $100 \times 150 \mu\text{m}$  pixels. The nearly  
458 square pixel shape enables approximately 15  $\mu\text{m}$  hit resolution in both the  $r$ - $\phi$  and  $z$   
459 directions [14, 10].

460        The silicon pixel sensors are composed of highly doped n-type silicon implants  
461        in an n-type silicon substrate with a p-n junction on the opposite side. These “n-  
462        on-n” sensors are more expensive than traditional “p-on-n” sensors but are chosen  
463        for their radiation hardness. Specifically, the increased electron contribution to the  
464        signal charge lessens the impact of the radiation-damage-induced reduction in carrier  
465        lifetime [10, 33]. Signals whose analog pulse height exceeds a pre-determined value  
466        (set individually for each pixel) are read out and amplified by the bump-bonded  
467        ROCs. The resulting hit location and pulse height information are read out at each  
468        L1 trigger (see Section 2.2.6).

469        The original pixel detector was designed for a maximum instantaneous luminosity  
470        of  $10^{34} \text{ cm}^{-2} \text{ s}^{-1}$ , which corresponds to approximately 25 pileup collisions per bunch  
471        crossing in CMS. As shown in Fig. 2.3, the LHC first exceeded this instantaneous  
472        luminosity in 2016. Figure 2.7 shows the resulting hit efficiency loss in the inner-  
473        most layer of the pixel detector as a function of instantaneous luminosity and pileup.  
474        While the higher-radius pixel layers are less affected, important quantities such as the  
475        transverse impact parameter resolution are highly dependent on the measurements of  
476        the layer closest to the interaction. To mitigate this effect, CMS replaced the original  
477        pixel detector between the 2016 and 2017 data-taking periods.

478        **Phase-1 pixel detector**

479        The Phase-1 pixel detector represents an incremental improvement over the orig-  
480        inal CMS pixel detector: the same fundamental technology fills the same physical  
481        footprint and reuses many of the existing services but nevertheless achieves higher  
482        rate capabilities, improved radiation tolerance, and more robust tracking [12]. This

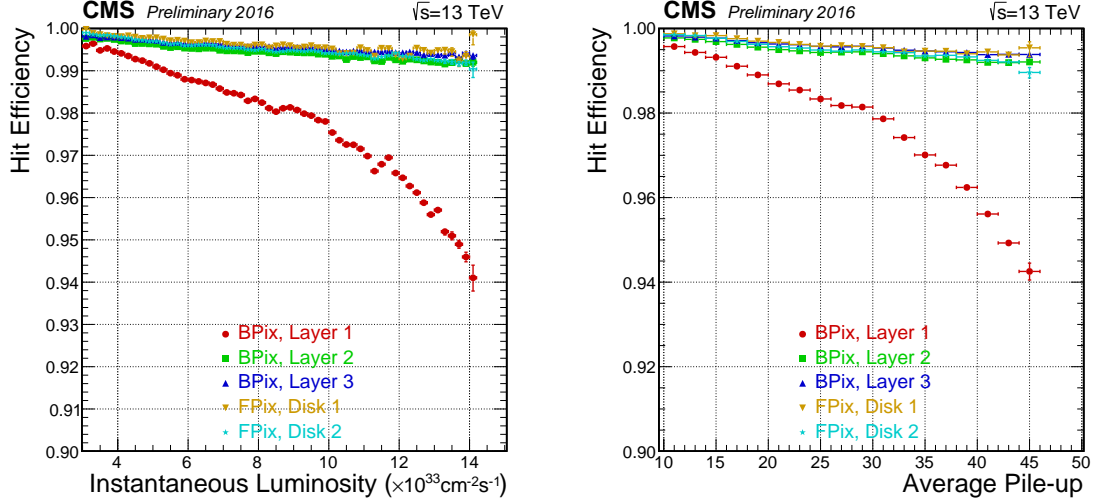


Figure 2.7: Measured single hit efficiency per layer as a function of the instantaneous luminosity (left) and pileup interactions (right) in data taken with the original CMS pixel detector in 2016 [11].

483 is accomplished by adding one additional layer to the barrel and each endcap, de-  
 484 creasing the radius of the innermost barrel layer to 2.9 cm, upgrading the ROCs, and  
 485 reducing the material budget of the cooling system and mechanical structure [12, 45].

486 Figure 2.8 compares the geometries of the original and Phase-1 pixel detectors.

487 The loss of hit efficiency at high instantaneous luminosity observed in the origi-  
 488 nal pixel detector is significantly reduced in the Phase-1 pixel detector. Despite the  
 489 higher particle flux that accompanies the shift to a smaller radius, the Phase-1 in-  
 490 nermost pixel layer maintains a single hit efficiency well over 98 % when operating at  
 491 an instantaneous luminosity of  $1.4 \times 10^{34} \text{cm}^{-2} \text{s}^{-1}$  during the 2017 data-taking pe-  
 492 riod [46]. Looking at Fig. 2.7, the equivalent quantity for the original pixel detector  
 493 is approximately 94 %.

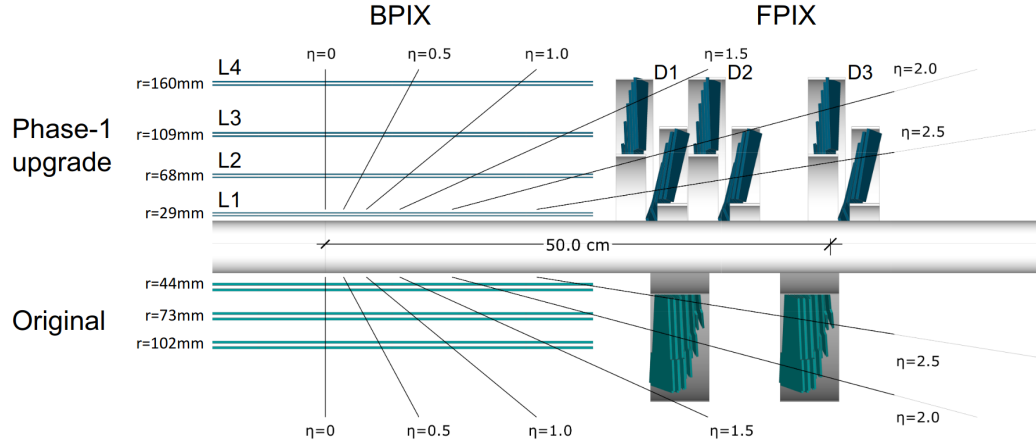


Figure 2.8: Comparison of the original and Phase-1 CMS pixel detector layouts in  $y$ - $z$  plane [12].

#### 494    Strip tracker

495    The strip tracker surrounds the pixel detector with silicon micro-strip sensors in  
 496    10 cylindrical barrel layers between  $r = 20\text{ cm}$  and  $r = 110\text{ cm}$  and 12 disks on each  
 497    side of the barrel detector that extend to  $|z| = 282\text{ cm}$  and cover up to  $|\eta| < 2.5$ .  
 498    The strip pitch generally increases with radius and results in hit resolutions that vary  
 499    from 23 to  $530\text{ }\mu\text{m}$  [10]. Figure 2.9 shows the layout of the entire silicon tracker.

500    Sitting farther from the interaction point allows the strip tracker to utilize more  
 501    typical p-on-n type sensors that are composed of highly doped p-type silicon strips  
 502    embedded in an n-type silicon substrate with a layer of highly doped n-type silicon  
 503    on the side opposite the strips. As the n-type silicon substrate is slowly converted  
 504    to p-type silicon by bulk radiation damage, the p-n junction moves from the strips  
 505    to the back side of the sensor. Custom integrated circuits amplify, shape, and store  
 506    the analog signals from each strip sensor. At each L1 trigger, the analog signals are

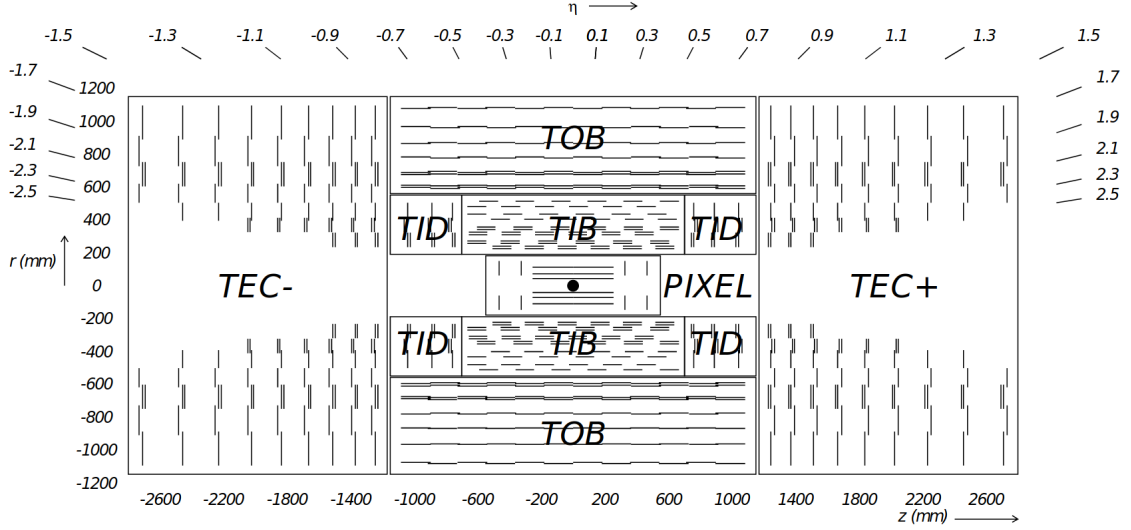


Figure 2.9: Layout of the CMS silicon tracker. TIB, TOB, TID, and TEC refer to subdetectors of the strip detector while PIXEL refers to the original pixel detector. The Phase-1 pixel detector is contained within the same volume [10].

507 transferred off-detector by optical fibers to be processed. Reading out the full analog  
 508 information reduces the tracker material budget and need for custom radiation-hard  
 509 electronics by performing analog-to-digital conversion, pedestal subtraction, and other  
 510 processing outside the detector volume [10].

### 511 2.2.3 Electromagnetic calorimeter

512 After traversing the inner tracker, particles next encounter the electromagnetic  
 513 calorimeter (ECAL). As a homogeneous scintillation calorimeter, ECAL uses 61 200  
 514 lead tungstate crystals in the barrel and 7324 in each endcap to reconstruct the en-  
 515 ergy deposited during electromagnetic showers. Lead tungstate crystals allow for  
 516 a fast (80 % of light emitted within 25 ns), compact (radiation length = 0.89 cm),

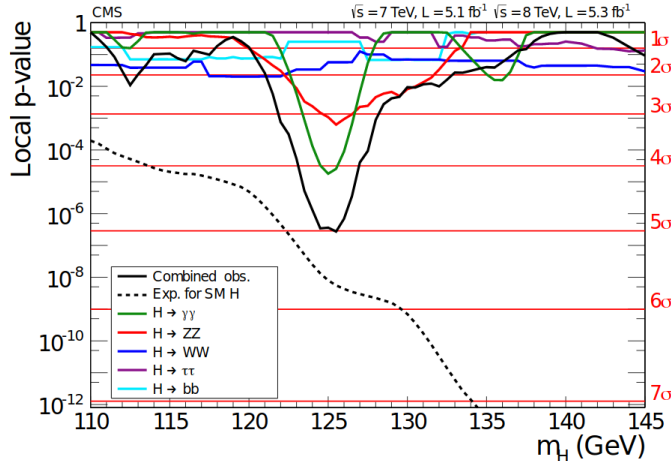


Figure 2.10: The observed local p-value for the five decay modes and the overall combination as a function of the SM Higgs boson mass showing the importance of the ECAL mass resolution in the discovery of the Higgs boson by the CMS experiment. The dashed line shows the expected local p-values for a SM Higgs boson with a mass  $m_H$  [13].

517 fine-grained (Molière radius = 2.2 cm), and radiation hard (up to 10 Mrad) calorime-  
 518 ter. The main drawback is the relatively low light yield (30 photon/MeV), which  
 519 necessitates photodetectors with intrinsic gain that work in magnetic fields [10, 14].

520 The ECAL performance requirements were heavily influenced by the possibility  
 521 to reconstruct the decay of a Higgs boson to two photons [43]. Despite the small  
 522 branching fraction and irreducible background, this decay channel provides a clean  
 523 signature of a narrow mass peak on top of a smoothly falling background. Thanks in  
 524 large part to the excellent ECAL energy resolution, the di-photon channel provided  
 525 the largest significance and best mass resolution (approximately 1 GeV resolution at  
 526 125 GeV) in the CMS Higgs boson discovery in 2012, as shown in Fig. 2.10 [13].

527 The barrel section extends radially from 129 to 177 cm and covers up to  $|\eta| < 1.479$ .  
 528 The crystals are tapered to approximately project back to the nominal collision point

529 but not so perfectly that likely particle trajectories align with cracks. Each crystal is  
530 approximately one Molière radius wide and 25 radiation lengths deep. The crystals  
531 in each endcap section are arranged in an  $x$ - $y$  grid that starts at  $|z| = 315$  cm and  
532 covers  $1.479 < |\eta| < 3.0$ .

### 533 2.2.4 Hadronic calorimeter

534 Particles that survive the ECAL will next encounter the hadronic calorimeter  
535 (HCAL). As the ECAL constitutes approximately 25 radiation lengths but only one  
536 interaction length, all but the particles that decay through the strong force will be  
537 filtered out before reaching the HCAL. In addition to reconstructing the decays of  
538 hadrons, the HCAL plays a particularly important role in measuring  $p_T^{\text{miss}}$ . By max-  
539 imizing the coverage in  $\eta$  and overall amount of material in terms of interaction  
540 lengths, HCAL ensures that nearly all particles (other than muons, neutrinos, and  
541 hypothetical BSM particles) decay and deposit all their energy before reaching the  
542 solenoid. Muon momentum is reconstructed with the tracker and muon system, so  
543 only neutrinos and hypothetical BSM particles will contribute to  $p_T^{\text{miss}}$ . Reliable  $p_T^{\text{miss}}$   
544 measurements are particularly important when searching for new weakly interacting  
545 particles with large lifetimes such as potential dark matter candidates or R-parity-  
546 conserving LSPs that can pass through the detector without interacting.

547 With these goals and the constraint of fitting within the solenoid volume in mind,  
548 HCAL is designed as a sampling calorimeter that uses 3.7 mm thick plates of plastic  
549 scintillator interspersed within approximately 5 cm thick brass absorber plates to

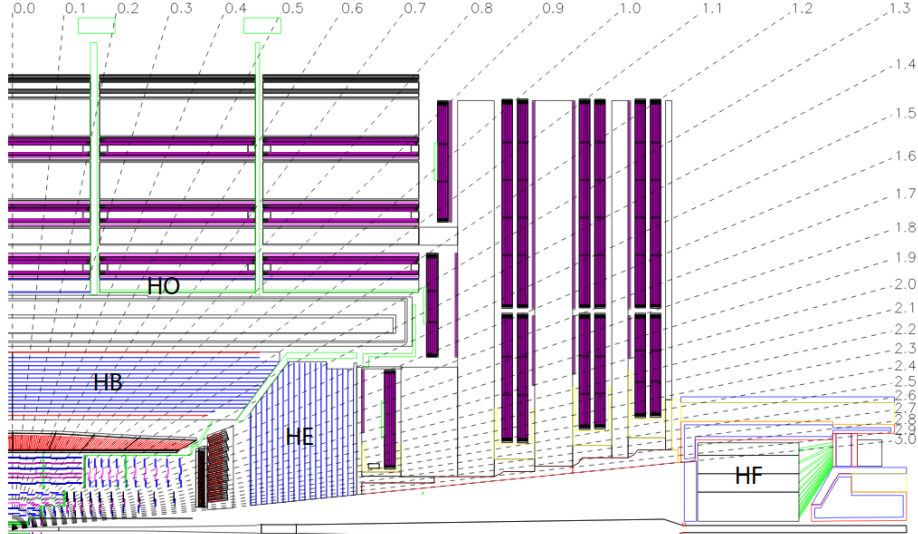


Figure 2.11: Layout of the hadron calorimeter barrel (HB), outer (HO), endcap (HE), and forward (HF) subdetectors [10].

550 reconstruct the energy deposited during hadronic showers. Embedded wavelength-  
 551 shifting fibers capture the scintillation light and transfer it to clear fibers to be read  
 552 out by hybrid photodiodes.

553 The barrel section ( $|\eta| < 1.4$ ) is segmented into 32 towers in  $\eta$  and 64 in  $\phi$  that  
 554 each contain 17 active scintillator layers. In the  $|\eta| < 1.26$  range, an extra layer of  
 555 scintillator tiles (or two at  $\eta = 0$ ) sits just outside the solenoid and increases the  
 556 minimum effective HCAL interaction length to greater than 11.8. Each endcap spans  
 557 a pseudorapidity range of 1.3 to 3.0 with 14 towers in  $\eta$  and 5 to 10°  $\phi$  segmentation.  
 558 Also, a steel and quartz fiber forward calorimeter (HF) sits 11.2 m from the interac-  
 559 tion point and covers  $3 < |\eta| < 5$ . In HF, particles produce Cherenkov light when  
 560 traversing the quartz fibers that run parallel to the beamline. Figure 2.11 shows the  
 561 layout of the barrel, endcap, and forward HCAL subdetectors.

562    **2.2.5 Muon system**

563       The CMS muon system is composed of three varieties of gaseous detectors em-  
564       bedded in the iron return yoke outside the superconducting solenoid. In the central  
565       region ( $|\eta| < 1.2$ ), the low muon and neutron rates along with the lower magnetic field  
566       allow the use of drift tube (DT) chambers. At higher  $\eta$  ( $0.9 \leq |\eta| < 2.4$ ), cathode  
567       strip chambers (CSCs) are required to handle the higher rates and larger magnetic  
568       field. Finally, resistive plate chambers (RPCs), which provide more accurate time  
569       measurements and worse spatial resolution than the DTs and CSCs, complement the  
570       other detectors out to  $|\eta| < 1.9$  [14, 47].

571       As shown in Fig. 2.12, the muon momentum resolution of the inner tracker is about  
572       an order of magnitude better than that of the muon system for low- $p_T$  muons. The  
573       muon system is critical, however, for maintaining the  $< 10\%$  momentum resolution  
574       that is necessary to unambiguously differentiate muons and anti-muons up to 1 TeV.  
575       In addition to improving muon reconstruction, the muon system provides information  
576       to the L1 trigger (see Section 2.2.6) and is capable of triggering on muons with good  
577       efficiency, high background rejection, and about 15–25%  $p_T$  resolution without input  
578       from the rest of the detector.

579       The DTs are organized into four stations, each of which contain up to 70 DT  
580       chambers that each measure the muon hit position in either the  $r$ - $\phi$  or  $z$  direction.  
581       Each chamber is composed of two or three collections of four-layer groupings of 13  
582       by 42 mm drift cells. As diagrammed in Fig. 2.13, a 2–4 m anode wire runs down the  
583       center of each drift cell while electrode and cathode strips line the top, bottom,  
584       and walls of the cell. The cells are filled with an Ar/CO<sub>2</sub> gas mixture that is ionized

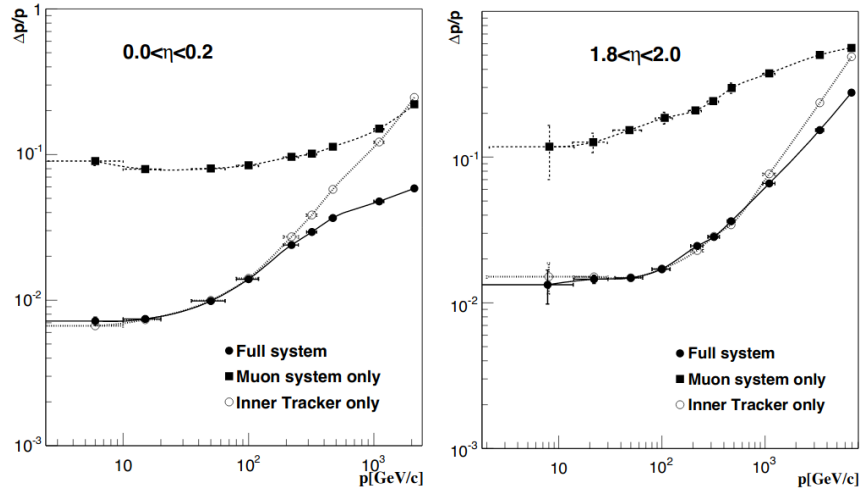


Figure 2.12: Muon momentum resolution as a function of momentum when using the CMS muon system, the CMS inner tracker, and the combination of the two subdetectors in two different  $\eta$  ranges [14].

585 by charged particles traversing the cell. The liberated electrons cause avalanches in  
 586 the large electric fields before being collected by the anode wire.

587 Each endcap contains four CSC stations, each with six layers of CSCs whose cath-  
 588 ode strips run radially outward to provide muon hit position measurements in the  $r\phi$   
 589 plane while the anode wires run in the azimuthal direction to provide measurements  
 590 in  $\eta$ . As in the DTs, charged particles ionize a gas mixture inside each chamber (this  
 591 time an Ar/CO<sub>2</sub>/CF<sub>4</sub> mixture), which leads to an avalanche of electrons that are col-  
 592 lected by an anode wire. In the CSCs, however, several anode wires share the same  
 593 chamber and a two-coordinate position measurement is obtained by also reading out  
 594 the induced charge on the perpendicular cathode strips.

595 The barrel and endcap regions also contain several RPC planes that ensure muons  
 596 are associated with the correct bunch crossing and serve as a complementary muon

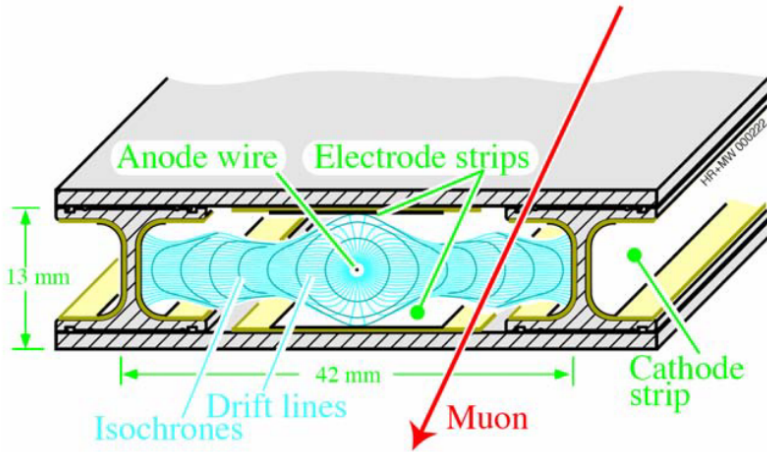


Figure 2.13: Sketch of a CMS muon system drift cell showing drift lines and isochrones. The plates at the top and bottom of the cell are at ground potential while the voltages applied to the electrodes are +3600 V for wires, +1800 V for strips, and -1200 V for cathodes [10].

597 trigger system. Each RPC plane is composed of parallel resistive plates separated  
 598 by two 2 mm gas gaps. Charged particles ionize the gas, a voltage differential leads  
 599 to an avalanche, and the total induced signal is read out as the sum of the induced  
 600 signal in each gap. The double-gap approach allows for high-efficiency operation  
 601 with lower voltage differentials than would be required for a single gap. At lower  
 602 voltages, the RPCs operate in “avalanche mode”, which allows for stable performance  
 603 and time resolution on the order of 2 ns despite particle fluxes up to hundreds of  
 604 Hz cm<sup>-2</sup> [10, 33, 48].

## 605 2.2.6 Trigger

606 The LHC provides bunch crossings to CMS at a nominal rate of 40 MHz. It is not  
 607 possible to read out and store full event information at anywhere near this rate, so

608 the CMS trigger system is designed to identify the most interesting events to be read  
609 out at approximately 1 kHz. The rate reduction happens in two stages: The Level-1  
610 (L1) trigger and High-Level Trigger (HLT). The L1 trigger uses custom electronics  
611 to analyze input from ECAL, HCAL, and the muon system to analyze each event in  
612 less than 3.8  $\mu$ s and select potentially interesting events at a rate of approximately  
613 100 kHz. The HLT, which is implemented in software on a dedicated processor farm,  
614 uses information from all subdetectors to further reduce the rate to approximately  
615 1 kHz [10, 49].

616 The L1 trigger processes calorimeter and muon system information in two separate  
617 trigger systems before combining the two outputs in a global trigger system that  
618 decides whether to pass a given event along to the HLT. The L1 algorithms are  
619 implemented on field programmable gate arrays housed on boards that communicate  
620 via optical link at  $10 \text{ GB s}^{-1}$ . The L1 Calorimeter Trigger uses coarsely segmented  
621 information from ECAL and HCAL to reconstruct electron, photon, tau lepton, and  
622 jet candidates, and the L1 Muon Trigger combines information from the DTs, CSCs,  
623 and RPCs to reconstruct muon candidates [50].

624 The HLT utilizes more than 400 different algorithms (called “paths”) that run on a  
625 farm of over 26 000 commercial processors. Each path runs a sequence of modules that  
626 either reconstruct or filter physics objects. The modules are ordered such that the  
627 fastest algorithms filter the object collections early, and the most resource-intensive  
628 algorithms only run when necessary. HLT paths generally mimic the selection and  
629 reconstruction algorithms used in CMS analyses, including the Particle Flow concept  
630 described in the following section, but are more aggressively optimized to satisfy the  
631 significant time and computing constraints imposed by the high event rate [49].

632    **2.2.7 Physics object reconstruction**

633       CMS uses a particle-flow (PF) algorithm to reconstruct the properties of individ-  
634       ual particles from the combination of all subdetector measurements. Starting from  
635       charged particle tracks from the tracker and muon system and clusters of energy  
636       deposited in the ECAL and HCAL, CMS’s PF algorithm aims to reconstruct all  
637       final-state electrons, muons, photons, and charged and neutral hadrons in a given  
638       event. In this section, I first describe the reconstruction of tracks and energy clus-  
639       ters before moving on to the individual particle identification and reconstruction. A  
640       complete description of the CMS PF algorithm is available in Ref. [15].

641    **Charged particle tracks**

642       Charged particle tracks are reconstructed with an iterative procedure in which the  
643       highest-purity algorithms are run first, and the hits associated with each reconstructed  
644       track are masked before moving on to the next step. Despite the middling reconstruc-  
645       tion efficiency of each individual step, this approach results in higher efficiency than  
646       could be achieved with any single tracking algorithm and without meaningfully in-  
647       creasing the rate of misreconstruction. This general principle applies to all charged  
648       particle tracks, but the tracks associated with candidate electrons and muons receive  
649       special consideration.

650       To better handle electron trajectories affected by radiative energy loss, CMS  
651       employs a special iterative tracking procedure that includes a Gaussian-sum filter  
652       (GSF) [51]. This approach improves the overall reconstruction efficiency, allows recon-  
653       struction of lower- $p_T$  electrons, and helps identify electrons from photon conversions  
654       and distinguish electrons from charged hadrons.

655 Muon track reconstruction benefits from measurements in the tracker and the  
656 muon system. Candidate muon tracks are placed in one of three categories depending  
657 on which subdetectors are used in their reconstruction: standalone muon tracks only  
658 use muon system hits; tracker muon tracks only use tracker hits and the requirement  
659 of at least one consistent muon system hit; and global muon tracks are reconstructed  
660 from a global fit of tracker and muon system hits.

## 661 **Calorimeter energy clusters**

662 Energy deposits in the calorimeters are clustered separately in ECAL and HCAL  
663 with a Gaussian-mixture model that assumes the energy deposits arise from an arbi-  
664 trary number of Gaussian energy deposits whose amplitude and location are allowed  
665 to vary while the width is determined by the calorimeter properties. The clusters are  
666 first seeded by cells with energy above some threshold and greater than the energy  
667 of the surrounding cells. Nearby clusters are then merged before being fed to the  
668 Gaussian-mixture algorithm. Finally, several corrections are applied to the cluster  
669 energies to ensure accurate responses to photons and hadrons.

## 670 **Particle-flow reconstruction**

671 The tracks and clusters are then identified with and used to reconstruct all in-  
672 dividual particles in an event. The first step is to link tracks and clusters together  
673 into groups that correspond one or a few particles. Tracker tracks are extrapolated  
674 outwards and linked with the nearest ECAL and HCAL clusters that are within a  
675 set radius in the  $\eta$ - $\phi$  plane. In the case of candidate electron tracks, tracker tracks  
676 and ECAL deposits consistent with electron radiative losses are also linked with the  
677 candidate electron track. ECAL and HCAL clusters are similarly linked together by

678 proximity in the  $\eta$ - $\phi$  plane. Due to the high granularity of CMS subdetectors, the  
679 number of tracks and clusters in a linked group is largely independent of the total  
680 number of particles in an event.

681       Each group of linked tracks and clusters is then processed by the PF particle  
682 identification and reconstruction algorithm. As in track reconstruction, particle re-  
683 construction is an iterative process in which the tracks and clusters are masked after  
684 being associated with a particle. Figure 2.14 diagrams the basic concept used to  
685 identify muons, electrons, photons, and charged and neutral hadrons. Each step of  
686 the PF algorithm is summarized below.

687       Muons are reconstructed first from isolated global muon candidates, then non-  
688 isolated global muon candidates, and finally tracker muon (standalone muon) can-  
689 didate tracks that are particularly well measured and consistent with hits in the  
690 muon system (tracker). Muon momentum is taken from the tracker track when  
691  $p_T < 200 \text{ GeV}$  and from the combination of tracker and muon system hits that yields  
692 the best fit otherwise.

693       Electron and isolated photon reconstruction, which occur together after muon  
694 reconstruction, are necessarily interrelated by the high probability that an electron  
695 radiates a photon or a photon pair-produces electrons when interacting with tracker  
696 material. Electrons are identified from GSF tracks with a corresponding ECAL cluster  
697 while isolated photons are identified from isolated ECAL clusters. The total electron  
698 energy accounts for radiative losses that show up as ECAL clusters, and both electrons  
699 and isolated photons require a high ratio of ECAL cluster energy to nearby HCAL  
700 cluster energy.

701        Next, nonisolated photons and charged and neutral hadrons are reconstructed  
702        from the remaining tracks and clusters. Within the tracker acceptance ( $|\eta| < 2.5$ ),  
703        ECAL (HCAL) clusters without associated tracks are identified as photons (neutral  
704        hadrons). At higher  $\eta$ , nearby ECAL and HCAL clusters are assumed to arise from the  
705        same hadron shower and ECAL clusters without nearby HCAL clusters are identified  
706        as photons. Discrepancies between track momenta and associated HCAL cluster  
707        energy are also used to identify neutral hadrons and muons. Finally, a post-processing  
708        step corrects for rare failure modes that can potentially produce inaccurately large  
709         $p_T^{\text{miss}}$  measurements.

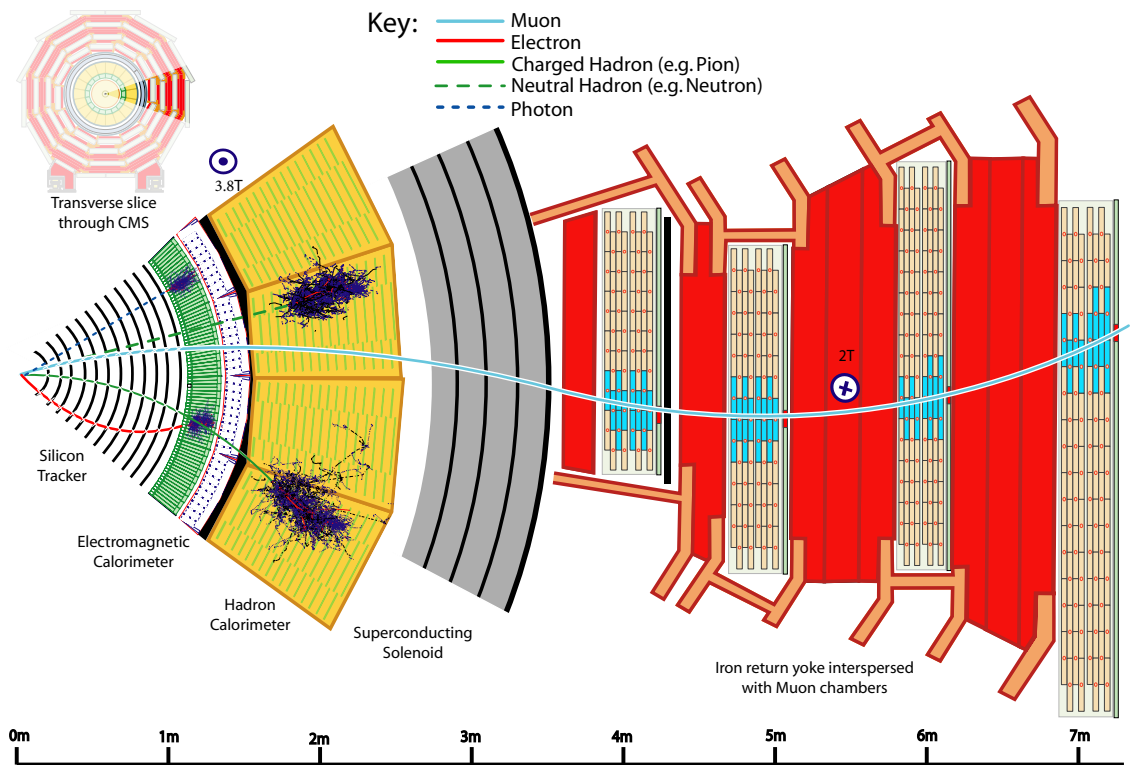


Figure 2.14: A sketch of a transverse slice of the CMS detector showing representative particle interactions used to identify and reconstruct particles with the CMS Particle Flow algorithm [15].

710

## Chapter 3: Search for displaced leptons

711 In this chapter, I present a search for new long-lived particles (LLPs) that could  
712 be produced in proton-proton collisions at a center-of-mass energy of 13 TeV at the  
713 LHC and detected by the CMS experiment. The search targets the unique signature  
714 of “displaced leptons” that could be produced when LLPs decay to leptons after  
715 propagating a measurable distance from the location of the proton-proton collision.

716 The candidate signal events include at least two leptons (one electron and one muon,  
717 two electrons, or two muons) whose transverse impact parameters are between 0.01  
718 and 10 cm. Choosing transverse impact parameter as the main discriminating variable  
719 allows us to target pairs of displaced leptons without requiring that they form a  
720 common vertex. We apply an otherwise minimal event selection to retain sensitivity  
721 to a wide range of new physics models.

722 The Ohio State CMS group has previously performed two related searches for  
723 displaced leptons in the electron-muon final state: one in  $19.7 \text{ fb}^{-1}$  of 8 TeV data and  
724 another in  $2.6 \text{ fb}^{-1}$  of 13 TeV data [52, 53]. The search presented here is the most  
725 sensitive to date. Some of the most significant improvements include:

- 726
- adding sensitivity to the electron-electron and muon-muon final states

727

  - simplifying the event selection to reduce model dependence

- 728     • introducing a custom lepton isolation definition to significantly reduce the back-  
729         ground from heavy-flavor meson decays
- 730     • implementing a new, fully data-driven background estimation procedure
- 731     • expanding the signal region to include leptons with smaller transverse impact  
732         parameters
- 733     • adding a second signal interpretation
- 734     • analyzing more than a factor of 40 times more data than the previous 13 TeV  
735         analysis [53]

736         Also, the ATLAS collaboration has recently submitted a paper in which they  
737         target displaced leptons with transverse impact parameters between 0.3 and 30 cm.  
738         They observe no significant excess and set upper limits on the production cross section  
739         of long-lived sleptons in a gravity-mediated SUSY breaking model [54].

740         The remainder of this chapter is organized as follows: Section 3.1 introduces the  
741         displaced leptons experimental signature in the context of LLPs at the LHC and  
742         gives an overview of the analysis strategy, Section 3.2 defines the data and simulated  
743         SM and signal samples used in the analysis, Section 3.3 describes the event selection  
744         criteria and defines the signal and control regions, Section 3.4 describes the various  
745         corrections applied to the SM and signal simulation, Section 3.5 investigates the  
746         sources of background and defines the procedure for estimating their contribution to  
747         the signal region, Section 3.6 describes the sources of systematic uncertainty in the  
748         efficiency for simulated signal events to pass the signal region selection, and Section 3.7  
749         presents the results.

750 **3.1 Overview**

751 **3.1.1 Long-lived particles at the LHC**

752 As discussed in Section 1.2.2, LLPs are common in the SM and naturally arise in  
753 many BSM scenarios. When produced in proton-proton collisions at the LHC, new  
754 LLPs have the potential to produce striking experimental signatures that differentiate  
755 them from SM backgrounds. As diagrammed in Fig. 3.1, new LLPs that decay within  
756 the detector volume can produce displaced vertices, physics objects whose trajectories  
757 do not point back to the location of the proton-proton collision, or particle tracks  
758 that vanish before reaching the outer edge of the tracker. Neutral LLPs that decay  
759 farther out can pass undetected through the tracker before producing signals in the  
760 calorimeters or muon system, and heavy, charged LLPs that are stable on detector  
761 length scales can be identified by their unusually large charge depositions.

762 The identification of any of these LLP signatures above the expected background  
763 rates would be a clear sign of new physics, but their atypical nature adds an inherent  
764 layer of difficulty to studying such signatures. In fact, standard reconstruction algo-  
765 rithms and event selections frequently discard such unusual signatures and render the  
766 majority of LHC analyses insensitive to many BSM scenarios that include LLPs [55].  
767 As a solution to the naturalness problem may require new physics at the LHC energy  
768 scale, it is critical that physicists face the challenges posed by LLP analyses and look  
769 everywhere BSM physics may be hiding.

770 Interest in LLPs is growing as evidence of BSM physics continues to evade LHC  
771 physicists. Recent CMS searches in 13 TeV proton-proton collisions target disappear-  
772 ing tracks [56] or use the ECAL timing capabilities to target photons or jets whose

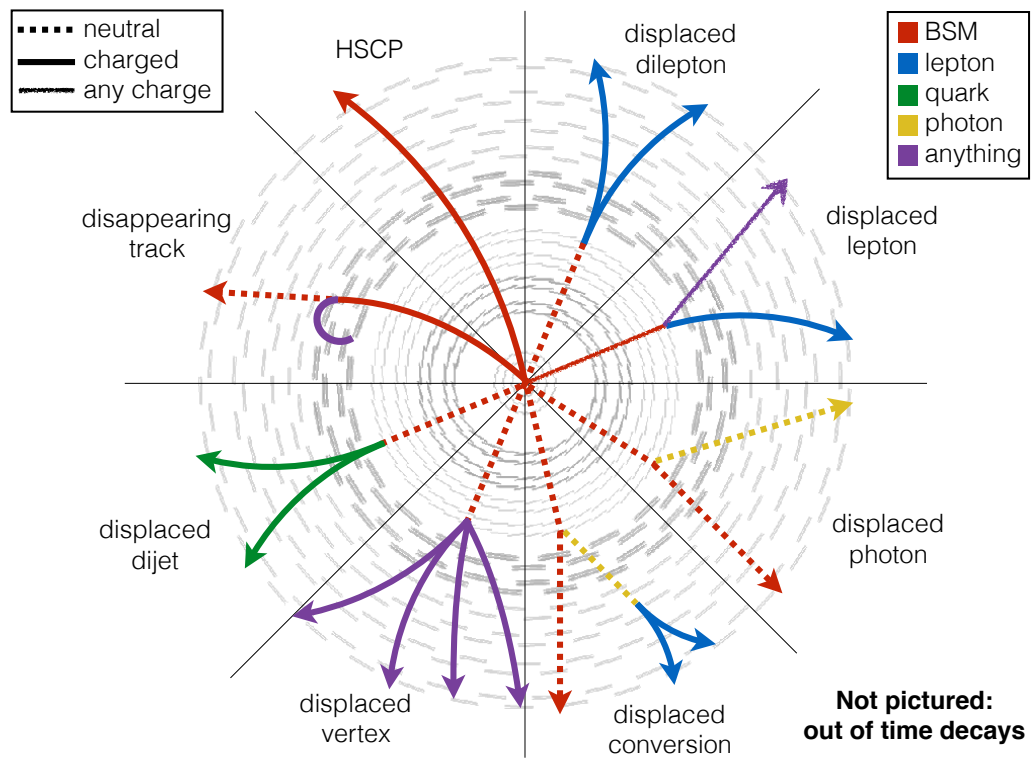


Figure 3.1: Illustration of several possible experimental signatures of long-lived particles [16].

773 production at a displaced vertex delays the time of their detection [57, 58]. All ob-  
774 servations thus far agree with SM predictions, but these and other LLP analyses are  
775 probing regions of BSM parameter space that are untested by conventional analyses.

### 776 3.1.2 Displaced leptons signature

777 The Displaced Leptons analysis targets electrons and muons produced in the de-  
778 cays of new, LLPs. Inspired by models such as Displaced SUSY (see Section 1.2.3), we  
779 take care to maintain sensitivity to leptons that are produced in separate long-lived  
780 decays as well as those that share a common displaced vertex. This goal is achieved  
781 by selecting pairs of leptons with large transverse impact parameters and setting no  
782 constraints on the presence or absence of displaced vertices. Figure 3.2 shows the  
783 benefit of such an approach: the pair-produced new LLPs, labeled  $X$ , each decay to  
784 a single lepton and an unspecified second particle. The lepton transverse impact pa-  
785 rameter, which is labeled  $d_0$  in the figure and defined explicitly below, is then used to  
786 identify the displaced nature of the lepton decays without explicitly constraining the  
787 other decay products in any way. Note also that the same strategy would successfully  
788 identify two leptons from a single long-lived particle decay.

789 Lepton transverse impact parameter,  $d_0$ , is defined as the distance of closest ap-  
790 proach in the transverse plane of the helical trajectory of the lepton track to the CMS  
791 beamspot, which is the center of the region in which the proton bunches cross.  $d_0$  is  
792 commonly measured with respect to the primary vertex, but in the case of leptons  
793 produced in displaced decays, the association between a given primary vertex and  
794 the resulting leptons is unreliable. We determine  $d_0$  from measured properties of the

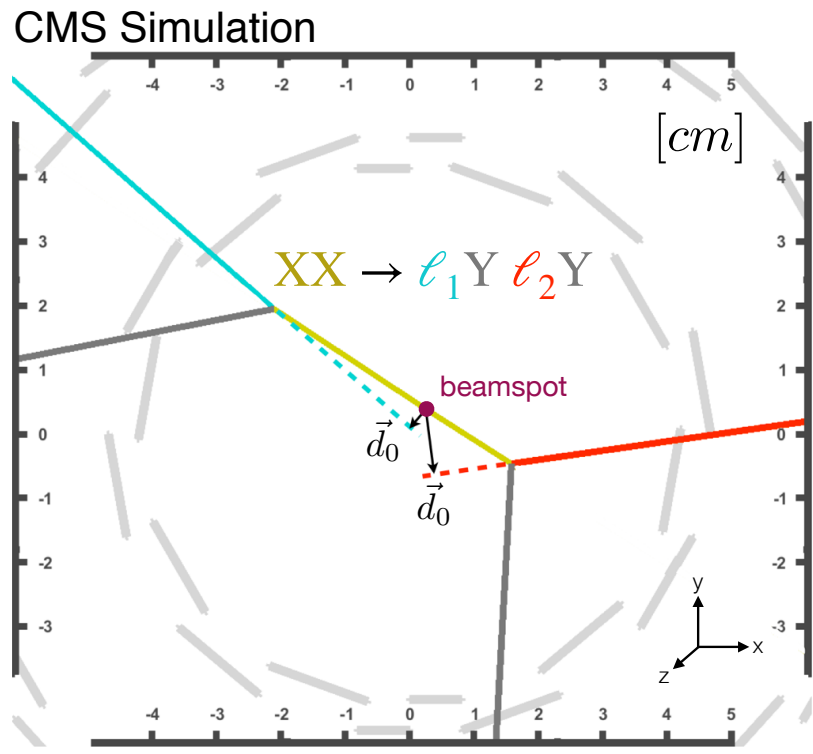


Figure 3.2: Illustration of the displaced leptons signature showing the definition of  $d_0$  in a transverse view of the CMS detector.  $X$  denotes a new long-lived particle,  $\ell$  denotes an electron or muon, and  $Y$  denotes any other decay products of the new long-lived particle. When interpreting the results of the Displaced Leptons analysis with the Displaced SUSY model,  $X$  refers to a top squark and  $Y$  refers to a b or d quark.

795 lepton track using the following equation:

$$d_0 = \frac{(v_x - x_0)p_y - (v_y - y_0)p_x}{p_T} \quad (3.1)$$

796 where  $v_x$  and  $v_y$  refer to the  $x$  and  $y$  coordinates of the lepton track reference point,  
797 which is usually chosen to be the point of closest approach to the center of CMS,  $x_0$   
798 and  $y_0$  refer to the  $x$  and  $y$  coordinates of the beamspot, and  $p_x$ ,  $p_y$ , and  $p_T$  refer to the  
799 magnitudes of the  $x$ ,  $y$ , and transverse components of the lepton's momentum.  $|d_0|$   
800 is commonly used throughout the Displaced Leptons analysis because we generally  
801 care about the magnitude of  $d_0$  but not its direction.

802 If we are to use lepton  $|d_0|$  as the discriminating variable in an LLP search, we  
803 must ensure it scales appropriately with the parent LLP lifetime. Typically, a particle  
804 with lifetime  $\tau$  will travel a distance  $d = \beta\gamma c\tau$ , where  $\beta$  and  $\gamma$  are relativistic factors  
805 and  $c$  is the speed of light, so  $d$  and  $\tau$  are directly correlated. Figure 3.2 shows that  
806 lepton  $|d_0|$  is determined by the distance travelled by the new LLP in the transverse  
807 plane and the angle between the transverse momenta of the new LLP and the lepton.  
808 Unless this angle is pathologically constrained to zero,  $|d_0|$  and  $\tau$  will be directly  
809 correlated as well. In fact, the maximum value of lepton  $|d_0|$ , which occurs when  
810 the angle between the transverse momenta of the new LLP and the lepton is  $\frac{\pi}{2}$ , is  
811 exactly equal to the transverse distance between the beamspot and location of the  
812 LLP decay.

813 Figure 3.3 shows the distribution of data and simulated Displaced SUSY events  
814 in the plane defined by electron and muon  $|d_0|$ . As expected, the data events, which  
815 are dominated by leptons from promptly decaying parent particles, are concentrated  
816 at low  $|d_0|$  values while the Displaced SUSY events are spread across the entire plane.  
817 This figure shows the power of  $|d_0|$  as a discriminating variable: requiring two leptons

818 with  $|d_0| > 100 \mu\text{m}$  eliminates nearly all the SM background without requiring that  
819 the leptons form a common vertex.

820 Another possible discriminating variable could be  $|d_0|/\sigma_{|d_0|}$ , where  $\sigma_{|d_0|}$  is the  
821 uncertainty in  $|d_0|$ . Such a discriminating variable could potentially reduce the back-  
822 ground from leptons with poorly measured  $|d_0|$ , but we choose to use  $|d_0|$  because of  
823 its straightforward correspondence to the parent particle lifetime. We also find that  
824  $\sigma_{|d_0|}$  is often underestimated, which reduces the potential benefit of using  $|d_0|/\sigma_{|d_0|}$ .

### 825 3.1.3 Analysis strategy

826 Having seen that  $|d_0|$  can be used to identify leptons from long-lived particle decays  
827 without requiring that the leptons form a common vertex, we now define a strategy  
828 to target such a signature. The basic analysis strategy is outlined here and described  
829 in detail in the following sections.

830 In addition to maximizing our sensitivity to models such as Displaced SUSY,  
831 we also strive to develop an analysis that is model independent, signature based,  
832 and easy to reinterpret. With these goals in mind, we perform a relatively simple  
833 cut-and-count analysis in which our main event selection sets no constraints on any  
834 non-lepton physics object. Unlike previous displaced leptons analyses [52, 53], we  
835 allow final states with more than two leptons and set no constraints on the lepton  
836 charge. As explained in Section 3.3, we select events in three analysis channels:  
837 electron-electron ( $ee$ ), electron-muon ( $e\mu$ ), and muon-muon ( $\mu\mu$ ). We then divide  
838 the events into different regions of the plane defined by the  $|d_0|$  of the two leptons  
839 that define the analysis channel. Figure 3.3, for example, shows this plane in the

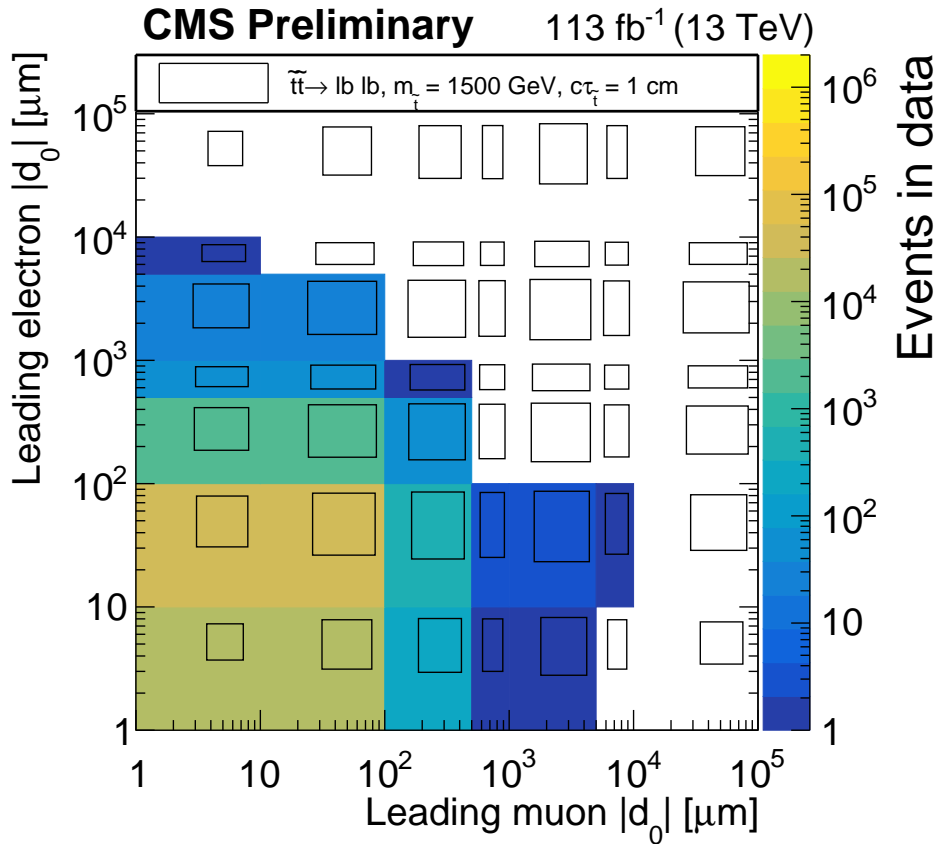


Figure 3.3: Distribution of data (colors) and simulated Displaced SUSY events (black boxes) in the plane defined by electron  $|d_0|$  and muon  $|d_0|$ . The size of the black boxes are proportional to the bin content, and the bins along the x and y axes include underflow. All events are required to pass the  $e\mu$  preselection defined in Section 3.3.

840  $e\mu$  channel. The signal region is defined as the region in which both leptons have  
841  $|d_0| > 100 \mu\text{m}$ .

842 Following the procedure defined in Section 3.5, we use the data in the non-signal  
843 regions to estimate the SM background in the signal region. Finally, we compare  
844 the background estimates and data yields in the signal region. In the absence of a  
845 significant excess, we use simulated signal events to constrain the available parameter  
846 space of the Displaced SUSY model. To avoid biasing the result, we blind ourselves  
847 to the data in the signal region and wait to observe the signal-region data until after  
848 we define and test the entire analysis procedure and receive pre-approval from the  
849 CMS Exotica Physics Analysis Group.

850    **3.2 Data and simulated samples**

851    **3.2.1 Experimental data**

852       This analysis uses proton-proton collision data taken in 2016, 2017, and 2018 at  
853       a center-of-mass energy of 13 TeV. In 2016, we use only the last two run periods due  
854       to lower displaced tracking efficiency caused by an analog pipeline voltage saturation  
855       problem in the silicon strip detector during the earlier run periods (see Appendix A).  
856       In 2017, we use all run periods in the  $ee$  channel and all but the earliest run period  
857       in the  $e\mu$  and  $\mu\mu$  channels because the  $e\mu$  and  $\mu\mu$  triggers are not available in the  
858       earliest run period. In 2018, we use all available run periods in all three channels.  
859       Ultimately, this analysis uses an integrated luminosity of  $16.1 \pm 0.4 \text{ fb}^{-1}$  from 2016 in  
860       all three channels,  $41.5 \pm 1.0 \text{ fb}^{-1}$  ( $36.7 \pm 0.8 \text{ fb}^{-1}$ ) from 2017 in the  $ee$  channel ( $e\mu$   
861       and  $\mu\mu$  channels), and  $59.7 \pm 1.5 \text{ fb}^{-1}$  from 2018 in all three channels.

862       The search is performed in the MuonEG, DoubleEG (in 2016–2017), EGamma (in  
863       2018), and DoubleMu primary datasets. We also use the MET dataset to study the trig-  
864       ger efficiency and the Cosmics and NoBPTX datasets to study the displaced tracking ef-  
865       ficiency. All data are reconstructed in the 07Aug17, 31Mar2018, 17Sep2018 reprocess-  
866       ing campaigns with software versions CMSSW\_8\_0\_31, CMSSW\_9\_4\_8, and CMSSW\_10\_2\_0,  
867       respectively. The sole exception is data-taking era D of the 2018 EGamma dataset,  
868       which is reconstructed in the 22Jan2019 campaign. In all cases, we use the CMS  
869       MiniAOD event format.

870    **3.2.2 Simulated background events**

871       This analysis employs a fully data-driven background estimation technique that  
872       does not rely on simulated SM events. We do, however, use simulated SM events

873 to study possible sources of background and verify the validity of the background  
874 estimation technique. The samples corresponding to 2016, 2017, and 2018 data con-  
875 ditions are from the `PdmVMCcampaignRunIISummer16`, `PdmVMCcampaignRunIIFall17`,  
876 and `PdmVMCcampaignRunIIAutumn18` production campaigns and were reconstructed  
877 in `CMSSW_8_0_31`, `CMSSW_9_4_8`, `CMSSW_10_2_0` with the MiniAODSIM event format.  
878 The samples simulating Z+jets, W+jets, and  $t\bar{t}$  production are generated using MAD-  
879 GRAPH5\_aMC@NLO [59, 60, 61], while the samples simulating diboson (WW, WZ,  
880 and ZZ with leptonic and semi-leptonic decays) and single-top-quark production are  
881 simulated with POWHEG v2 [62, 63, 64, 65, 66]. PYTHIA 8.2 [67] is used to simulate  
882 the parton showering and hadronization for all processes. The modeling of the under-  
883 lying event is generated using the CUETP8M1 [68] and CP5 tunes [69] for simulated  
884 samples corresponding to the 2016 and 2017–18 data sets, respectively.

### 885 3.2.3 Simulated signal events

886 We use simulated signal events to guide the analysis strategy and interpret our  
887 results. Samples of simulated  $pp \rightarrow \tilde{t}\tilde{t}$  events in which the top squarks decay to a lep-  
888 ton and a  $b$  quark or  $d$  quark are produced at leading order using PYTHIA 8.2. For  
889 simplicity, all lepton flavors are generated with equal branching fractions. The top  
890 squarks can form strongly-produced hadronic states called R-hadrons, which are gen-  
891 erated with PYTHIA. The interactions of the R-hadrons with matter are not simulated  
892 in GEANT4 [70], but they are expected to have a negligible impact on the analysis  
893 because the lepton identification requirements effectively require the R-hadron to de-  
894 cay in the middle of the tracker volume. Each R-hadron therefore traverses  $\lesssim 1$   
895 interaction length, making it unlikely to produce a high quality track, come to a stop

896 in the detector, or flip its charge. To generate the samples, we start with a SUSY  
897 Les Houches Accord file [71] corresponding to Snowmass Points and Slopes point  
898 1a [72] and modify the mass and width of the top squark according to the sample  
899 being produced. We generate samples with top squark masses from 100 to 1800 GeV  
900 at 100 GeV intervals and with top squark lifetimes at each decade from 0.1 mm to  
901 1 m. After producing these samples, we also employ a lifetime reweighting technique  
902 to effectively produce eight additional lifetime points between each pair of adjacent  
903 lifetimes. In the case of the 1 m samples, we also use an equivalent technique to ef-  
904 fectively produce nine additional lifetime points between 1 and 10 m. The production  
905 cross sections for each top squark mass hypothesis are taken from the website of the  
906 LHC SUSY Cross Section Working Group and reproduced in Table 3.1. The signal  
907 samples are reconstructed in the same campaigns and with the same conditions as  
908 the SM background samples described in 3.2.2.

Table 3.1: The top squark production cross sections used when generating the simulated  $\tilde{t}\tilde{t} \rightarrow \bar{l}b\bar{l}b$  and  $\tilde{t}\tilde{t} \rightarrow \bar{l}d\bar{l}d$  events. Cross sections are calculated at NLO + NLL by the LHC SUSY Cross Section Working Group.

$\tilde{t}$ mass [GeV]	Cross section [pb]	Cross section uncertainty
100	$1.52 \times 10^3$	15 %
200	$6.45 \times 10^1$	14 %
300	$8.52 \times 10^0$	14 %
400	$1.84 \times 10^0$	14 %
500	$5.18 \times 10^{-1}$	13 %
600	$1.75 \times 10^{-1}$	13 %
700	$6.70 \times 10^{-2}$	13 %
800	$2.83 \times 10^{-2}$	14 %
900	$1.29 \times 10^{-2}$	15 %
1000	$6.15 \times 10^{-3}$	16 %
1100	$3.07 \times 10^{-3}$	17 %
1200	$1.60 \times 10^{-3}$	19 %
1300	$8.50 \times 10^{-4}$	20 %
1400	$4.61 \times 10^{-4}$	22 %
1500	$2.56 \times 10^{-4}$	24 %
1600	$1.41 \times 10^{-4}$	27 %
1700	$8.08 \times 10^{-5}$	29 %
1800	$4.67 \times 10^{-5}$	31 %

909    **3.3 Event selection**

910    **3.3.1 Triggers**

911       The events are required to pass different triggers in each channel. Standard CMS  
912       electron and muon triggers are not designed for displaced objects, so we use non-  
913       standard triggers for both electrons and muons. For muons, we remove all trigger  
914       requirements relating to the muon  $d_0$ , longitudinal impact parameter ( $d_z$ ), or the ver-  
915       tex from which the muon originates. For electrons, we actually use photon triggers,  
916       which collect events with electrons as well as photons but do not rely on any tracking  
917       information. See Section 2.2.6 for a brief overview of the CMS trigger system.

918       In the  $e\mu$  channel, 2016 data and corresponding simulated events are required to  
919       pass the logical OR of two HLT paths (`HLT_Mu38NoFiltersNoVtx_Photon38_CaloI`  
920       `dL_v*` OR `HLT_Mu28NoFiltersNoVtxDisplaced_Photon28_CaloIdL_v*`) that were  
921       both originally designed for the 2015 CMS displaced leptons analysis [53]. The first  
922       trigger requires at least one muon with  $p_T > 38 \text{ GeV}$  and places no constraints on the  
923       vertex,  $d_0$ , or  $d_z$ . The second trigger requires at least one muon with  $p_T > 28 \text{ GeV}$   
924       and  $|d_0| > 0.01 \text{ cm}$ . Each of these two triggers also requires at least one photon that  
925       passes a loose calorimeter-based identification. The first (second) trigger requires  
926       that the photon  $E_T$  is greater than 38 GeV (28 GeV). The signal efficiency with these  
927       dedicated triggers is significantly higher than that of standard muon-photon HLT  
928       paths.

929       In 2017 and 2018, data and corresponding simulated events in the  $e\mu$  channel are  
930       required to pass `HLT_Mu43NoFiltersNoVtx_Photon43_CaloIdL_v*`. The muon  $p_T$   
931       and photon  $E_T$  thresholds are raised with respect to 2016 due to increased pileup. A

932 version of the 2016 trigger that requires displaced muons is not available in 2017 and  
933 2018.

934 In the  $ee$  channel, 2016 data and corresponding simulated events are required to  
935 pass the logical OR of two HLT paths (`HLT_Diphoton30_18_R9Id_OR_IsoCaloId_A`  
936 `ND_HE_R9Id_Mass90_v*` OR `HLT_DoublePhoton60_v*`). The first requires a leading  
937 photon with  $E_T > 30$  GeV and a subleading photon with  $E_T > 18$  GeV. Photons must  
938 pass calorimeter identification criteria involving isolation, the ratio of HCAL to ECAL  
939 energy, and shower shape, and the di-photon invariant mass must be  $> 90$  GeV. This  
940 path is highly efficient at low top squark mass. The second trigger simply requires at  
941 least two photons with  $E_T > 60$  GeV. This path is highly efficient at large top squark  
942 mass and lifetime.

943 In 2017 and 2018, data and corresponding simulated events in the  $ee$  channel are  
944 required to pass `HLT_Diphoton30_22_R9Id_OR_IsoCaloId_AND_HE_R9Id_Mass90_v*`  
945 OR `HLT_DoublePhoton70_v*`. The photon  $E_T$  thresholds are raised with respect to  
946 2016 due to increased pileup.

947 In the  $\mu\mu$  channel, 2016 data and corresponding simulated events are required to  
948 pass the logical OR of two HLT paths (`HLT_DoubleMu33NoFiltersNoVtx_v*` OR  
949 `HLT_DoubleMu23NoFiltersNoVtxDisplaced_v*`) that were both designed for this  
950 analysis. The first trigger requires at least two muons with  $p_T > 33$  GeV and sets no  
951 constraints on the vertex,  $d_0$ , or  $d_z$ . The second trigger requires at least two muons  
952 with  $p_T > 23$  GeV and  $|d_0| > 0.01$  cm. The signal efficiency with these dedicated  
953 triggers is significantly higher than that of standard di-muon HLT paths.

954 In 2017 and 2018, data and corresponding simulated events in the  $\mu\mu$  channel are  
955 required to pass `HLT_DoubleMu43NoFiltersNoVtx_v*`. The muon  $p_T$  threshold is

956 raised with respect to 2016 due to increased pileup. A version of the 2016 trigger that  
957 requires displaced muons is not available in 2017 and 2018.

958 **3.3.2 Preselection**

959 Starting from the events collected with the triggers described above, we next apply  
960 a set of preselection criteria to select the events to be analyzed. The preselection  
961 criteria vary by channel and year, but the fundamental goal is always to select events  
962 with at least one good reconstructed lepton of each flavor required by the channel.

963 Specifically, the  $e\mu$  preselection selects events with at least one PF electron and  
964 at least one global PF muon, the  $ee$  preselection selects events with at least two PF  
965 electrons, and the  $\mu\mu$  preselection selects events with at least two global PF muons  
966 (see Section 2.2.7 for a discussion of the PF algorithm). We set requirements on these  
967 electrons and muons as shown in Tables 3.2, 3.3, and 3.4. The electron and muon  
968  $p_T$  requirements are chosen such that the trigger efficiency is independent of lepton  
969  $p_T$  (see Section 3.4.4), while electron and muon  $|\eta|$  requirements are chosen to reduce  
970 the fraction of leptons with poorly measured  $d_0$  (see Appendix B). Electrons that  
971 traverse the gap between the endcap and barrel detectors are also rejected due to the  
972 known decrease in reconstruction performance in this region.

973 We use a tight cut-based identification (ID) on the electrons and muons to select  
974 well-reconstructed leptons, but unlike the standard ID definitions used in many CMS  
975 analyses, we do not place any requirements on  $d_0$  or  $d_z$ . In all other respects, we  
976 follow the cut-based ID recommendations of the CMS EGamma and Muon Physics  
977 Object Groups. The electron ID corresponds to `egmGsfElectronIDs:cutBasedElectron`  
978 `tronID-Summer16-80X-V1-tight` in 2016, `egmGsfElectronIDs:cutBasedElectron`

Table 3.2: The  $e\mu$  preselection criteria. The electron and muon  $p_T$  thresholds increase in 2017 in accordance with the increased HLT electron and muon  $p_T$  thresholds.

Selection variable	Number	Object-level selections		Muon
		Electron	Muon	
$p_T$				$\geq 1$
		$> 42 \text{ GeV}$ (2016)		$> 40 \text{ GeV}$ (2016)
		$> 45 \text{ GeV}$ (2017 and 2018)		$> 45 \text{ GeV}$ (2017 and 2018)
$ \eta $				$< 1.5$
		not in ECAL gap		-
		veto ( $1.0 < \eta < 1.5$ and $\phi > 2.7$ ) (2017)		veto ( $1.0 < \eta < 1.5$ and $\phi > 2.7$ ) (2017)
		veto ( $0.3 < \eta < 1.2$ and $0.4 < \phi < 0.8$ ) (2018)		veto ( $0.3 < \eta < 1.2$ and $0.4 < \phi < 0.8$ ) (2018)
ID		Tight (cut-based)		Tight (cut-based)
Custom isolation		Tight		Tight
			Event-level selections	
			Zero $\mu\mu$ pairs with $\cos \alpha < -0.99$	
			Reject $\Delta t < -20$ , if both timing ndof $> 7$	
			At least one $e\mu$ pair with $\Delta R(e, \mu) > 0.2$	
			Reject events with candidate leptons form a displaced vertex in the tracker material	

Table 3.3: The  $ee$  preselection criteria. The electron  $p_T$  threshold increases in 2017 and 2018 in accordance with the increased HLT electron  $p_T$  threshold.

Selection variable	Object-level selections	
	Electron	
Number	$\geq 2$	
$p_T$		$> 65 \text{ GeV (2016)}$ $> 75 \text{ GeV (2017 and 2018)}$
$ \eta $	$< 1.5$	not in ECAL gap
$\eta - \phi$ (pixel power supply issue)		veto ( $1.0 < \eta < 1.5$ and $\phi > 2.7$ ) (2017) veto ( $0.3 < \eta < 1.2$ and $0.4 < \phi < 0.8$ ) (2018)
ID		Tight (cut-based)
Custom isolation		Tight
	Event-level selections	
	At least one $ee$ pair with $\Delta R(e, e) > 0.2$	
	Reject events with candidate leptons from a displaced vertex in the tracker material	
	Reject events with displaced muons in the $e\mu$ channel inclusive signal region	

Table 3.4: The  $\mu\mu$  preselection criteria. The muon  $p_T$  threshold increases in 2017 and 2018 in accordance with the increased HLT muon  $p_T$  threshold.

Selection variable	Object-level selections	
	Muon	$\geq 2$
$p_T$		$> 35 \text{ GeV (2016)}$ $> 45 \text{ GeV (2017 and 2018)}$
$ \eta $		$< 1.5$
		veto ( $1.0 < \eta < 1.5$ and $\phi > 2.7$ ) (2017) veto ( $0.3 < \eta < 1.2$ and $0.4 < \phi < 0.8$ ) (2018)
ID	Tight (cut-based)	
Custom isolation	Tight	
Event-level selections		
		Zero $\mu\mu$ pairs with $\cos \alpha < -0.99$
		Reject $\Delta t < -20$ , if both timing ndof $> 7$
		At least one $\mu\mu$ pair with $\Delta R(\mu, \mu) > 0.2$
		Reject events with candidate leptons from a displaced vertex in the tracker material
		Reject events with displaced electrons in the $e\mu$ channel inclusive signal region

Table 3.5: The electron tight ID requirements, which are identical to the tight cut-based ID from the CMS EGamma Physics Object Group with the  $d_0$  and  $d_z$  requirements removed. Electron ID quantity definitions are available in Ref. [1].

Electron ID requirements	
full5x5 $\sigma_{in\eta} <$	0.0104 (2018, 2017) 0.00998 (2016)
$ \delta\eta_{\text{Seed}}  <$	0.00255 (2018) 0.00353 (2017) 0.00308 (2016)
$ \delta\phi_{\text{In}}  <$	0.022 (2018) 0.0499 (2017) 0.0816 (2016)
H/E <	0.026 + 1.15/E + 0.0324 $\rho$ /E (2018) 0.026 + 1.12/E + 0.0368 $\rho$ /E (2017) 0.0414 (2016)
PF isolation <	0.0287 + 0.506/ $p_T$ (2018) 0.0361 (2017) 0.0588 (2016)
$ 1/E - 1/p  <$	0.159 (2018) 0.0278 (2017) 0.0129 (2016)
expected missing inner hits $\leq$	1
pass conversion veto	yes

979 ID-Fall17-94X-V1-tight in 2017, and `egmGsfElectronIDs:cutBasedElectronID`  
 980 -Fall17-94X-V2-tight in 2018. The electron and muon tight ID requirements are  
 981 summarized in Tables 3.5 and 3.6.

982 We also require that electrons and muons are isolated. Specifically, we use a  
 983 modified isolation definition that accounts for the fact that displaced leptons may  
 984 be associated with the wrong primary vertex. The standard PF isolation assumes  
 985 all energy from primary vertices other than the leading primary vertex is due to

Table 3.6: The muon tight ID requirements, which are identical to the tight cut-based ID from the CMS Muon Physics Object Group with the requirements on  $d_0$  and  $d_z$  removed.

Muon ID requirements
Is a global muon
Is a PF muon
$\chi^2/n_{\text{dof}}$ of the global-muon track fit is $< 10$
At least one muon-chamber hit included in the global-muon track fit
Muon segments in at least two muon stations
At least 1 valid pixel hit
At least 6 tracker layers with hits

986 pileup, which is not true when the primary vertex ordering is altered by an incorrectly  
 987 associated lepton. We have therefore modified the isolation definition to be agnostic  
 988 to the primary vertex ordering by allowing PF candidates from any primary vertex  
 989 to contribute to the isolation sum and by using a simple  $\rho$ -based pileup correction,  
 990 where  $\rho$  is the total transverse energy of all the PF candidates in an event divided by  
 991 the total detector area. The modified isolation is calculated as:

$$\text{relative isolation} = \frac{\max(0, p_T^{h^\pm} + E_T^{h^0} + E_T^\gamma - \rho\pi R^2)}{p_T^\ell} \quad (3.2)$$

992 where  $R$  is the radius of a cone in the  $\eta$ - $\phi$  plane that is centered on the lepton,  $p_T^{h^\pm}$  is  
 993 the total  $p_T$  of charged hadrons in the cone,  $E_T^{h^0}$  is the total  $E_T$  of neutral hadrons in  
 994 the cone,  $E_T^\gamma$  is the total contribution of photons in the cone,  $\rho$  is defined as above,  
 995 and  $p_T^\ell$  is the lepton  $p_T$ .  $R$  is set to 0.3 for electrons and 0.4 for muons.

996 Figure 3.4 shows how the size of the pileup correction term depends on lepton  
 997 displacement in the standard isolation but not in the modified isolation described here.  
 998 We use the modified isolation definition for both electrons and muons while keeping  
 999 the original tight working point for electrons and slightly tightening the tight working

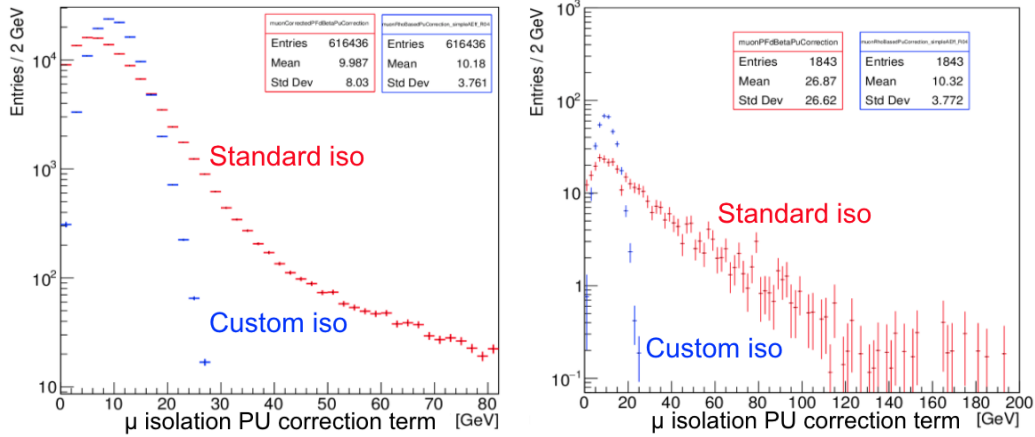


Figure 3.4: Comparison of the the muon isolation pileup correction term in the standard muon isolation and the modified muon isolation in simulated  $t\bar{t}$  events that pass the 2018  $e\mu$  preselection. Muon  $|d_0|$  is constrained to be less than 100  $\mu\text{m}$  in the plot on the left and between 500 and 1000  $\mu\text{m}$  in the plot on the right.

1000 point for muons. In the end, we require that the relative isolation is  $< 0.10$  for muons  
 1001 and  $< 0.0588$  for electrons in 2016 and  $< 0.0287 + 0.506/p_T$  for electrons in 2017 and  
 1002 2018. As shown in Figs. 3.5 and 3.6, this modified PF isolation rejects substantially  
 1003 more background when the leptons are displaced but does not significantly alter the  
 1004 signal yield. We note, however, that there may still be some minor dependence on the  
 1005 primary vertex selection in the PF muon requirement because the PF muon selection  
 1006 includes some loose isolation requirements where the charged hadron component is  
 1007 constrained to the selected primary vertex.

1008 We also reject electrons and muons in certain regions of the  $\eta$ - $\phi$  plane where lepton  
 1009  $d_0$  is more likely to be mismeasured. We identify these regions as highly populated  
 1010 bins in the electron  $\eta$ - $\phi$  distribution in a prompt-muon, displaced-electron control  
 1011 region in 2017 and 2018 data (see Fig.3.7). No such bins are present in 2016 data.  
 1012 The identified regions coincide with regions found by a previous CMS analysis [56] to

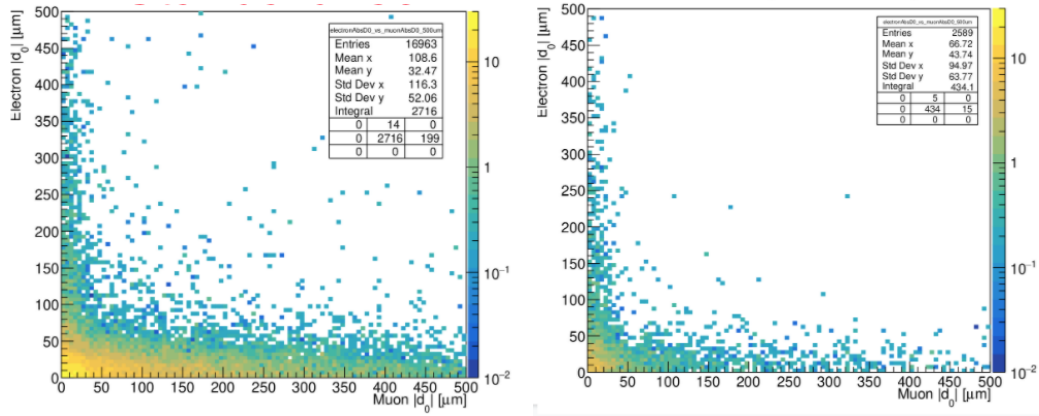


Figure 3.5: The distribution of  $t\bar{t}$  simulated events in the plane defined by electron  $|d_0|$  and muon  $|d_0|$ . The standard isolation is applied in the plot on the left, and the modified isolation is applied in the plot on the right, and the events in both plots are required to pass the remaining 2018  $e\mu$  preselection criteria and the additional constraint that the parent of at least one lepton is a heavy-flavor meson.

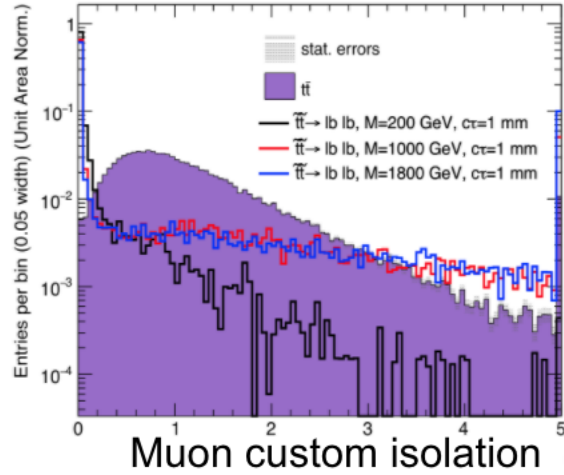


Figure 3.6: The muon modified isolation distribution for simulated  $t\bar{t}$  background and  $\tilde{t}\tilde{t} \rightarrow l b \bar{l} \bar{b}$  signal events that pass the 2018  $e\mu$  preselection with no isolation criterion applied.

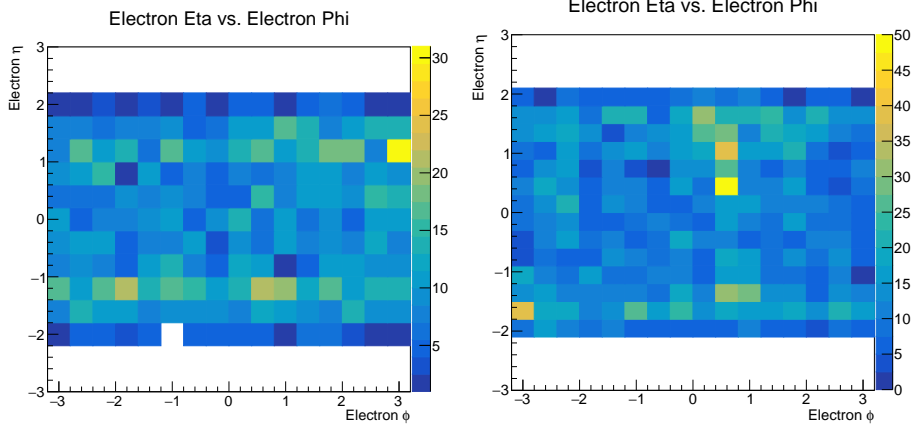


Figure 3.7: The electron  $\eta$ - $\phi$  distribution in a prompt-muon, displaced-electron control region in 2017 (left) and 2018 (right) data before vetoing the regions affected by pixel power-supply issues.

1013 be affected by power supply issues in the pixel detector. The  $\eta$ - $\phi$  variation is more  
 1014 apparent for displaced electrons than displaced muons, so we use data in a prompt  
 1015 muon ( $|d_0| < 40 \mu\text{m}$ ), displaced electron ( $100 < |d_0| < 500 \mu\text{m}$ ) control region to  
 1016 define the regions used for both electrons and muons. In 2017, the rejected region is  
 1017  $1.0 < \eta < 1.5$  AND  $\phi > 2.7$ , and in 2018 the rejected region is  $0.3 < \eta < 1.2$  AND  
 1018  $0.4 < \phi < 0.8$ .

1019 In addition to these object-level selections, we also impose a few event-level se-  
 1020 lections designed to remove potential backgrounds from cosmic rays, material inter-  
 1021 actions, and displaced decays of SM hadrons. To remove cosmic-ray muons in the  
 1022  $\mu\mu$  and  $e\mu$  channels, we require there be zero pairs of muons with  $\cos \alpha < -0.99$ ,  
 1023 where  $\alpha$  is the 3D angle between the muons, and that the relative time between the  
 1024 leading two muons is inconsistent with the timing of cosmic-ray muons. To do this,  
 1025 we look at the muon time measured by the DTs and CSCs, which assume that the

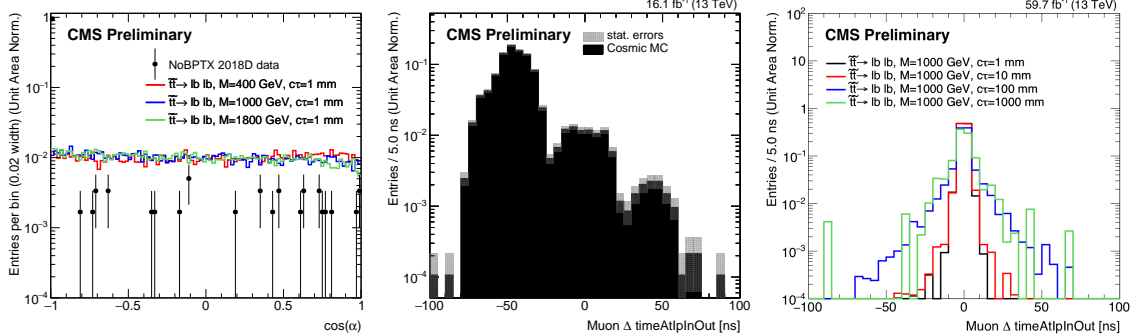


Figure 3.8: The di-muon  $\cos(\alpha)$  distribution of 2018 NoBPTX data and simulated  $\tilde{t}\tilde{t} \rightarrow \bar{l}b\bar{l}b$  events (left) and the di-muon  $\Delta t$  distribution in simulated cosmic-ray muon events in 2016 conditions (center) and  $\tilde{t}\tilde{t} \rightarrow \bar{l}b\bar{l}b$  (right) events in 2018 conditions. In each case, all  $\mu\mu$  preselection criteria except those relating to cosmic rejection are applied.

1026 muons are traveling outwards from the center of the detector. We then use the muon  
 1027  $\phi$  measurements to determine which muon is above the other and find  $\Delta t$ , the time  
 1028 of the lower muon subtracted from the time of the upper muon. We reject events  
 1029 with  $\Delta t < -20$  if the number of degrees of freedom of the timing measurements for  
 1030 both muons is greater than seven. Figure 3.8 shows the  $\cos \alpha$  and  $\Delta t$  distributions of  
 1031 NoBPTX data and simulated cosmic and  $\tilde{t}\tilde{t} \rightarrow \bar{l}b\bar{l}b$  events.

1032 To remove leptons from decays of SM hadrons, we require that the candidate  
 1033 leptons not be too close together in the  $\eta$ - $\phi$  plane. Specifically, we find that requiring  
 1034  $\Delta R > 0.2$  significantly reduces the contribution from SM hadrons without noticeably  
 1035 affecting the signal acceptance. To remove leptons from material interactions, we  
 1036 reject events in which the candidate leptons form a good displaced vertex that overlaps  
 1037 with the tracker material. The vertices are reconstructed with the Kalman Vertex  
 1038 Fitter, and a ‘‘good’’ vertex is one with  $\chi^2/n_{\text{dof}} < 20$ . The tracker material map is

1039 obtained from the tracker material budget measurements [73, 74]. See Section 3.5.6  
1040 for tests in data that involve inverting the criteria described in this paragraph.

1041 Finally, to ensure that the signal regions of all three channels are orthogonal to  
1042 one another, we reject events in the  $ee$  ( $\mu\mu$ ) channel with at least one muon (electron)  
1043 that passes the  $e\mu$  channel preselection and has  $|d_0| > 100 \mu\text{m}$ .

1044 In contrast to previous displaced leptons analyses [52, 53], we allow for the possi-  
1045 bility of more than one lepton of each type in a given channel and set no requirements  
1046 on the charge product of the lepton pair. These changes were made at the request of  
1047 several theorists, including the authors of Ref. [75].

1048 Figure 3.9 shows the electron and muon  $|d_0|$  distributions in simulated signal and  
1049 background events that pass the 2018  $e\mu$  preselection, and Fig. 3.10 shows the cumu-  
1050 lative number of simulated signal events that pass each 2018 preselection criterion in  
1051 all three channels for several top squark lifetime hypotheses.

### 1052 **3.3.3 Prompt control region**

1053 In order to verify the implementation of our selection and corrections to simula-  
1054 tion (see Section 3.4), we define a prompt control region that is dominated by SM  
1055 background events. Events in each channel’s prompt control region are selected by  
1056 requiring that they pass all of the criteria defined in Section 3.3.2 as well as the  
1057 requirement that the candidate leptons have  $|d_0| < 50 \mu\text{m}$ . We define this region in  
1058 each channel in order to check for reasonable agreement between simulated SM events  
1059 and data after applying the corrections described in Section 3.4. Some examples are  
1060 shown in Figs. 3.11, 3.12, and 3.13, which show the  $p_T$ ,  $\eta$ , and  $|d_0|$  distributions of the  
1061 leptons in the  $e\mu$ ,  $ee$ , and  $\mu\mu$  prompt control regions, respectively, for 2016 data and

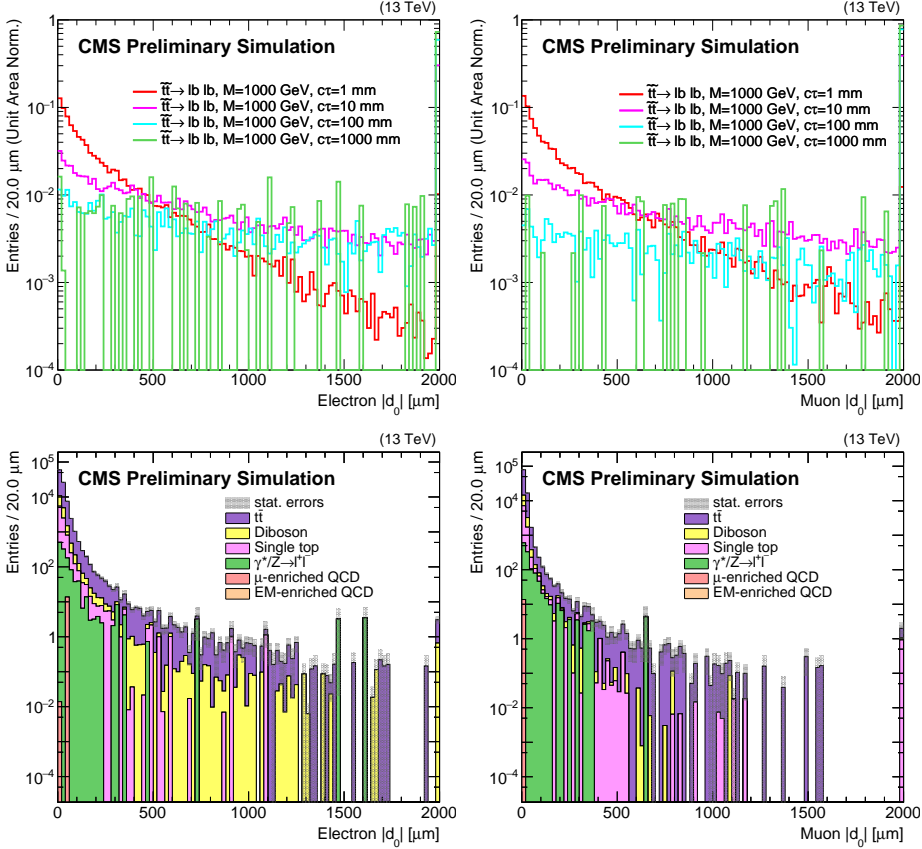


Figure 3.9: The electron (left) and muon (right)  $|d_0|$  distributions for 2018 simulation events that pass the  $e\mu$  preselection criteria. The upper two plots show  $\tilde{t}\tilde{t} \rightarrow \bar{l}b\bar{l}b$  simulation for a single  $\tilde{t}$  mass and four different proper decay lengths; each histogram is normalized to unity. The lower two plots show the background simulation normalized to the integrated luminosity. In all of the histograms, the last bin includes the overflow. All of the corrections from Section 3.4 are applied.

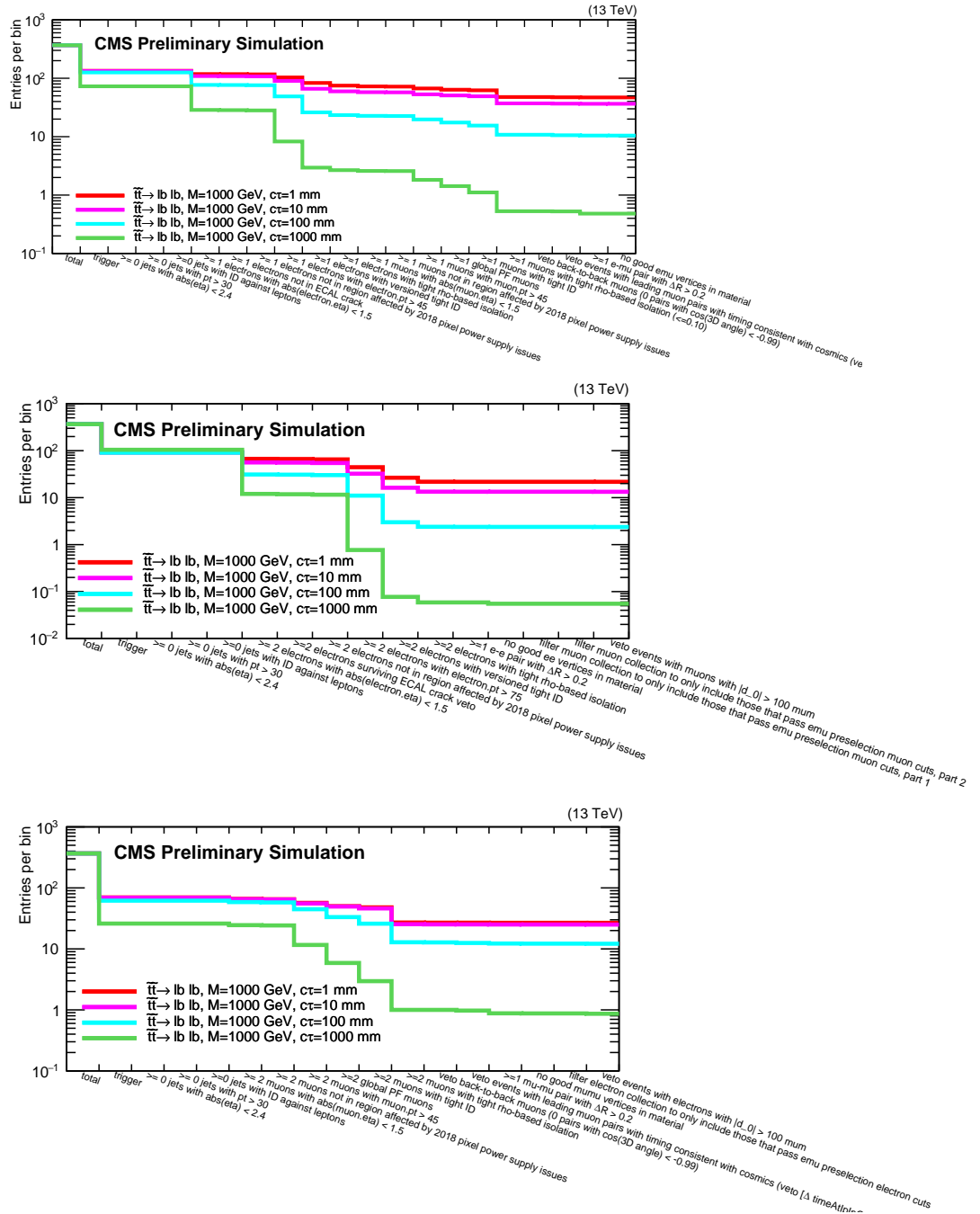


Figure 3.10: The cumulative number of simulated  $\tilde{t}\tilde{t} \rightarrow \bar{l}b\bar{l}b$  events that pass each criterion in the 2018  $e\mu$  (top),  $ee$  (middle), and  $\mu\mu$  (bottom) preselection. Several  $\tilde{t}$  proper decay lengths are shown. The jet criteria do not exclude any events and are simply an artifact of the analysis framework.

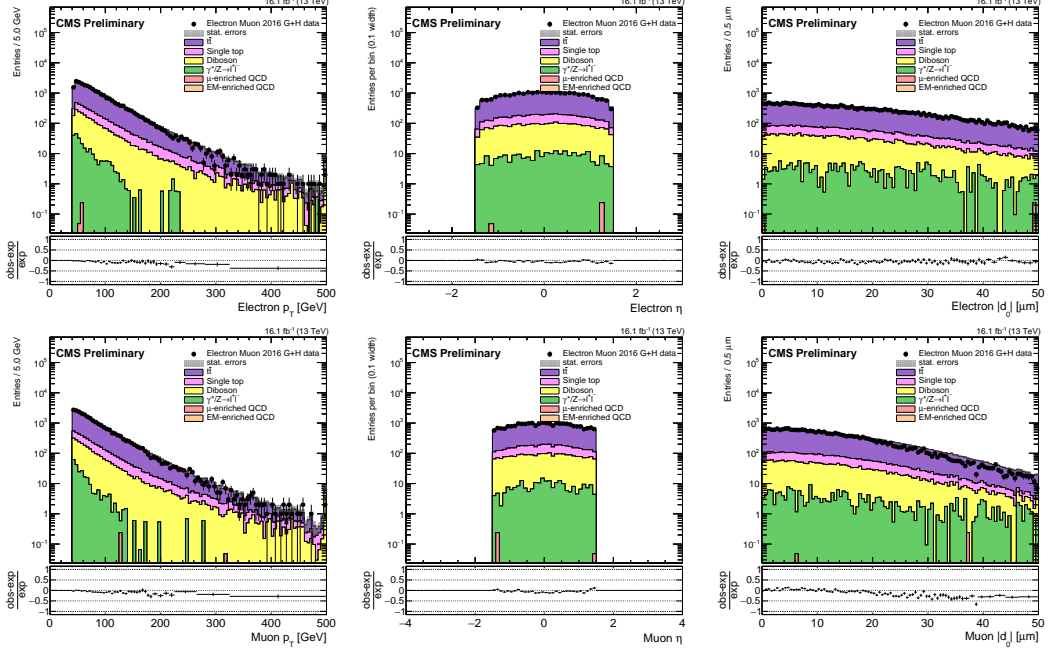


Figure 3.11: The electron (top) and muon (bottom)  $p_T$  (left),  $\eta$  (center), and  $|d_0|$  (right) distributions in the  $e\mu$  prompt control region for 2016 data and simulated background events. The rightmost bin in each plot contains the overflow entries.

background simulation. The data-driven background estimation technique employed in this analysis removes the need for exact agreement between data and simulation, but the absence of any significant discrepancies gives us confidence that we are accounting for the correct sources of prompt SM leptons and that our selection and corrections are functioning as intended.

### 3.3.4 Inclusive signal region

Finally, we define the region to which new physics may contribute significantly. The inclusive signal region is populated by events that pass all of the criteria defined in Section 3.3.2 as well as the requirement that the candidate leptons each have  $100 \mu\text{m} < |d_0| < 10 \text{ cm}$ . We do not select leptons with  $|d_0| > 10 \text{ cm}$  because the tracking

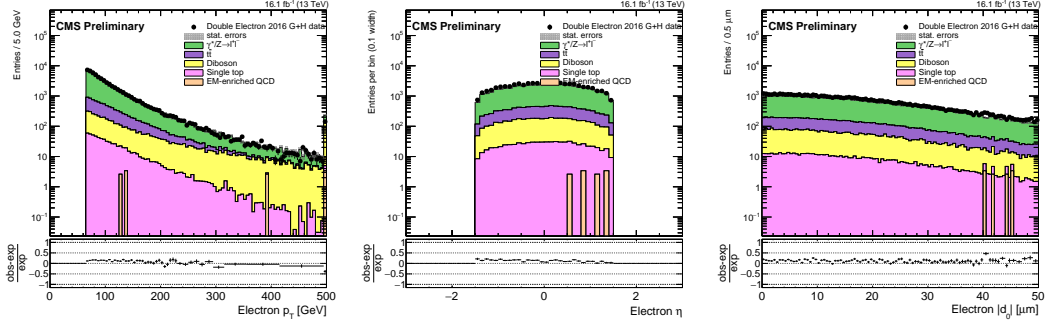


Figure 3.12: The electron  $p_T$  (left),  $\eta$  (center), and  $|d_0|$  (right) distributions in the  $ee$  prompt control region for 2016 data and simulated background events. The rightmost bin in each plot contains the overflow entries.

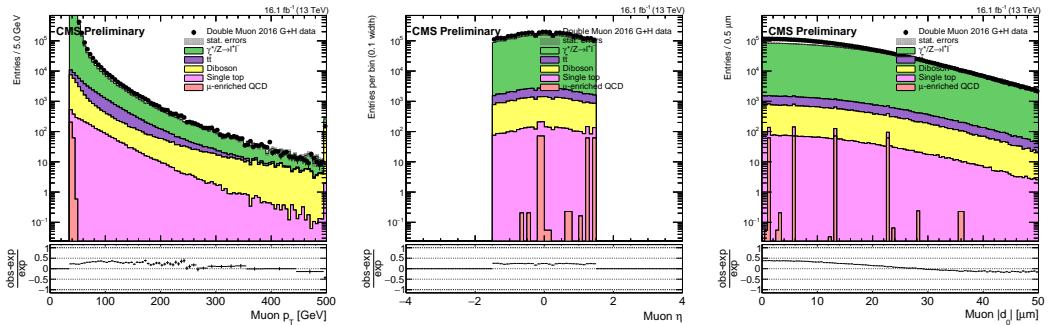


Figure 3.13: The muon  $p_T$  (left),  $\eta$  (center), and  $|d_0|$  (right) distributions in the  $\mu\mu$  prompt control region for 2016 data and simulated background events. The rightmost bin in each plot contains the overflow entries.

Table 3.7: The cumulative efficiency for simulated  $\tilde{t}\tilde{t} \rightarrow \bar{l}b\bar{l}b$  signal events to pass the 2018 inclusive signal region selection, for several choices of  $\tilde{t}$  mass and  $c\tau$ . The corrections described in Section 3.4 are applied.

$e\mu$ inclusive signal region			
	200 GeV	1000 GeV	1800 GeV
0.1 cm	2.1%	4.6%	4.6%
1 cm	3.5%	7.9%	8.8%
10 cm	1.0%	2.7%	3.4%
100 cm	0.047%	0.13%	0.16%

$ee$ inclusive signal region			
	200 GeV	1000 GeV	1800 GeV
0.1 cm	0.47%	2.1%	2.1%
1 cm	0.60%	2.8%	3.3%
10 cm	0.11%	0.59%	0.76%
100 cm	0.003%	0.014%	0.022%

$\mu\mu$ inclusive signal region			
	200 GeV	1000 GeV	1800 GeV
0.1 cm	1.4%	2.6%	2.5%
1 cm	3.1%	5.6%	5.9%
10 cm	1.5%	3.2%	3.7%
100 cm	0.11%	0.23%	0.34%

efficiency drops sharply after this point, as shown in Section C. This requirement also ensures that the leptons originate within the pixel volume, which is effectively required by the pixel hit requirement of the tight lepton IDs. Table 3.7 lists the cumulative efficiency for  $\tilde{t}\tilde{t} \rightarrow \bar{l}b\bar{l}b$  events to pass the full 2018 inclusive signal region selection for several signal points. To ensure sensitivity to a wide range of new particle masses and lifetimes, we further subdivide the inclusive signal region into bins defined by the  $|d_0|$  of each candidate lepton and the  $p_T$  of one candidate lepton. The exact binning is described in Section 3.5.2.

1080 **3.4 Corrections to simulation**

1081 We apply several corrections to the simulated background and signal events in  
1082 order to account for known differences between simulation and data. Each correction  
1083 is described individually in the following sections.

1084 **3.4.1 Pileup**

1085 The simulation is corrected so that its distribution of the number of pileup interac-  
1086 tions matches that of 2016, 2017, and 2018 data. Each simulated sample is reweighted,  
1087 event-by-event, by scale factors derived by dividing the pileup distribution in data by  
1088 the pileup distribution in the given simulated sample.

1089 **3.4.2 Lepton ID**

1090 We apply scale factors provided by the CMS Physics Object Groups to correct for  
1091 known differences in the lepton reconstruction and tight ID performance between data  
1092 and simulation. Although our lepton ID differs from the standard tight ID in that  
1093 we do not set requirements on  $d_0$  or  $d_z$ , the standard scale factors are still sufficient  
1094 because they are derived from leptons from Z boson decays that are representative  
1095 of leptons in the bulk of the  $|d_0|$  distribution, and we apply additional systematic  
1096 uncertainties to account for possible differences at larger  $|d_0|$  (see Section 3.6).

1097 **3.4.3 Lepton  $d_0$  resolution**

1098 As shown in Fig. 3.14, the agreement between data and simulation in the 2017 and  
1099 2018 electron and muon  $|d_0|$  distributions was initially poor. We found that the aver-  
1100 age muon and electron  $d_0$  fluctuated periodically with respect to  $\phi$  in 2017 and 2018  
1101 data but not in background simulation, as can be seen in Fig. 3.15. This periodic

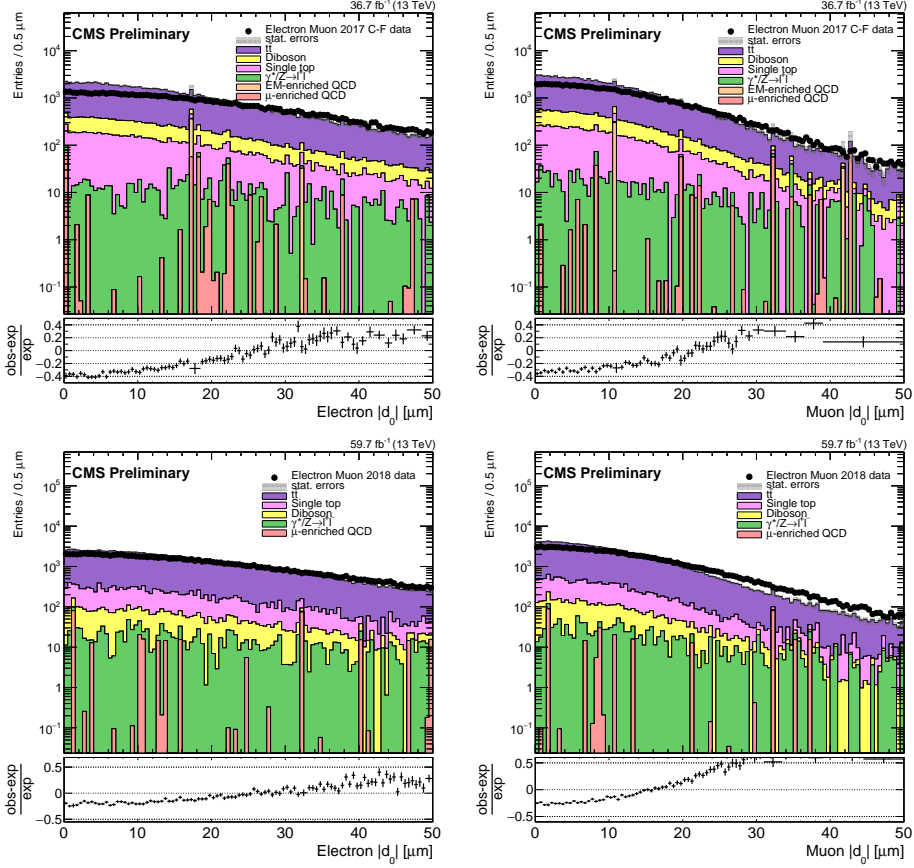


Figure 3.14: The uncorrected lepton  $|d_0|$  distributions in the  $e\mu$  prompt control region, for electrons (left) and muons (right), for 2017 data and simulation (top), and 2018 data and simulation (bottom). The rightmost bin in each plot contains the overflow entries.

fluctuation in data but not in simulation indicates that an overly optimistic simulated tracker alignment is responsible for the unrealistically narrow  $d_0$  distribution in simulation.

To account for the overly optimistic alignment in simulation, we smear the electron and muon  $d_0$  in 2017 and 2018 simulation in each channel's prompt control region to better model the  $d_0$  distribution in data. To do this, we first fit the central regions of the background simulation and data  $d_0$  distributions with Gaussian functions in each

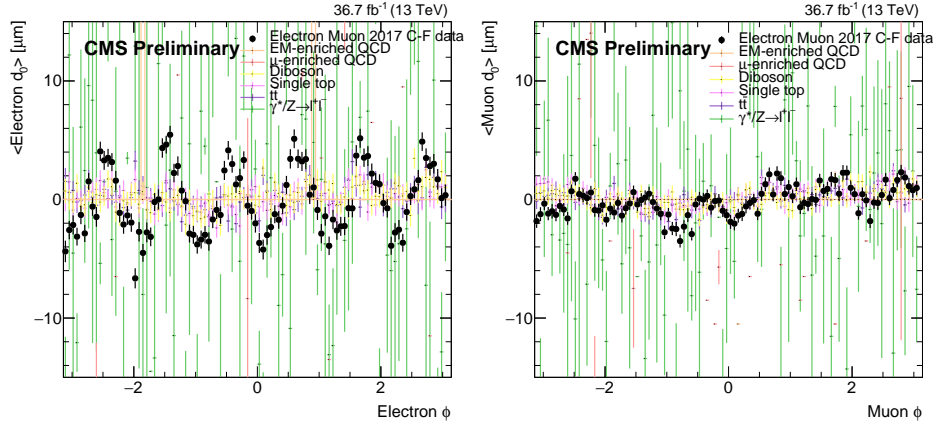


Figure 3.15: The average lepton  $|d_0|$  as a function of  $\phi$  in the  $e\mu$  prompt control region, for electrons (left) and muons (right), for 2017 data and simulation.

1109 channel's prompt control region and then compare the widths of the Gaussian fits.  
 1110 The fitted distributions are shown in Figs. 3.16 and 3.17 for the  $e\mu$  channel. Assuming  
 1111 that the width of each Gaussian fit is mostly determined by the  $d_0$  resolution, we define  
 1112  $\sigma_{data}^2 = \sigma_{bkg}^2 + \sigma_{align}^2$ , where  $\sigma_{data}$  is the data Gaussian width,  $\sigma_{bkg}$  is the uncorrected  
 1113 background simulation Gaussian width, and  $\sigma_{align}$  is the additional component that  
 1114 is needed to make up the difference in  $d_0$  resolution between background simulation  
 1115 and data. We find  $\sigma_{data}$  and  $\sigma_{bkg}$  from the fits and compute  $\sigma_{align}$ . The fit results are  
 1116 similar in the  $e\mu$  channel shown here and in the same-flavor channels. We average  
 1117 the  $\sigma_{align}$  derived in the  $ee$  channel and the  $e\mu$  channel for electrons, and in the  $\mu\mu$   
 1118 channel and the  $e\mu$  channel for muons. The average  $\sigma_{align}$  is shown in Table 3.8. We  
 1119 then smear the simulation  $d_0$  values with values drawn from a Gaussian distribution  
 1120 centered on zero and with a width of the average  $\sigma_{align}$ . The smearing is applied to  
 1121 both background and signal simulation. The corrected  $|d_0|$  distributions are shown  
 1122 in Fig. 3.18.

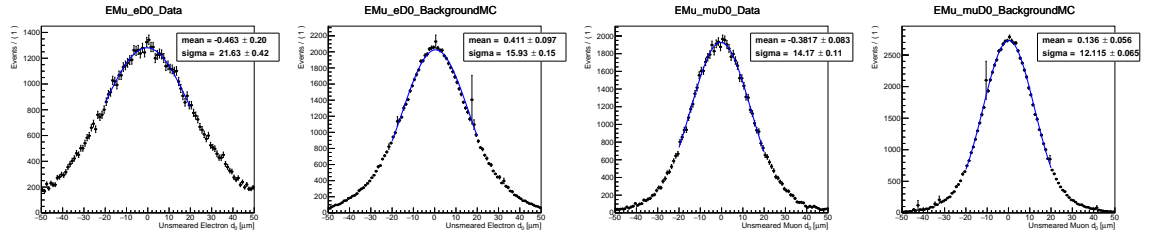


Figure 3.16: The lepton  $d_0$  distributions with Gaussian fits in the 2017  $e\mu$  prompt control region for (working from left to right) electrons in data, electrons in background simulation, muons in data, and muons in background simulation.

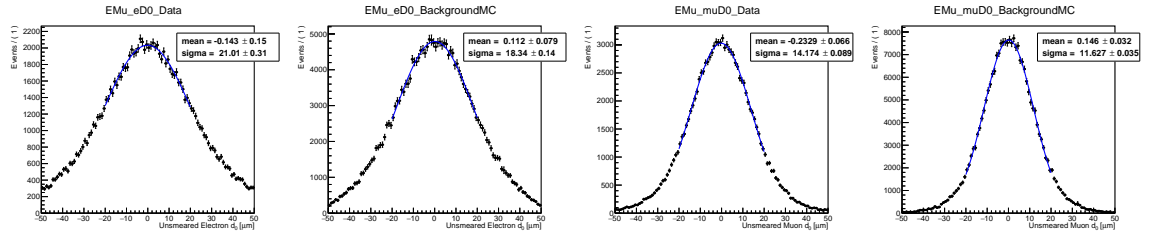


Figure 3.17: The lepton  $d_0$  distributions with Gaussian fits in the 2018  $e\mu$  prompt control region for (working from left to right) electrons in data, electrons in background simulation, muons in data, and muons in background simulation.

Table 3.8: The average  $\sigma_{align}$  for electrons and muons, for the 2017 and 2018 analyses.

	2017	2018
Electrons	$14.75 \pm 0.36 \mu\text{m}$	$9.18 \pm 0.41 \mu\text{m}$
Muons	$7.57 \pm 0.12 \mu\text{m}$	$8.11 \pm 0.08 \mu\text{m}$

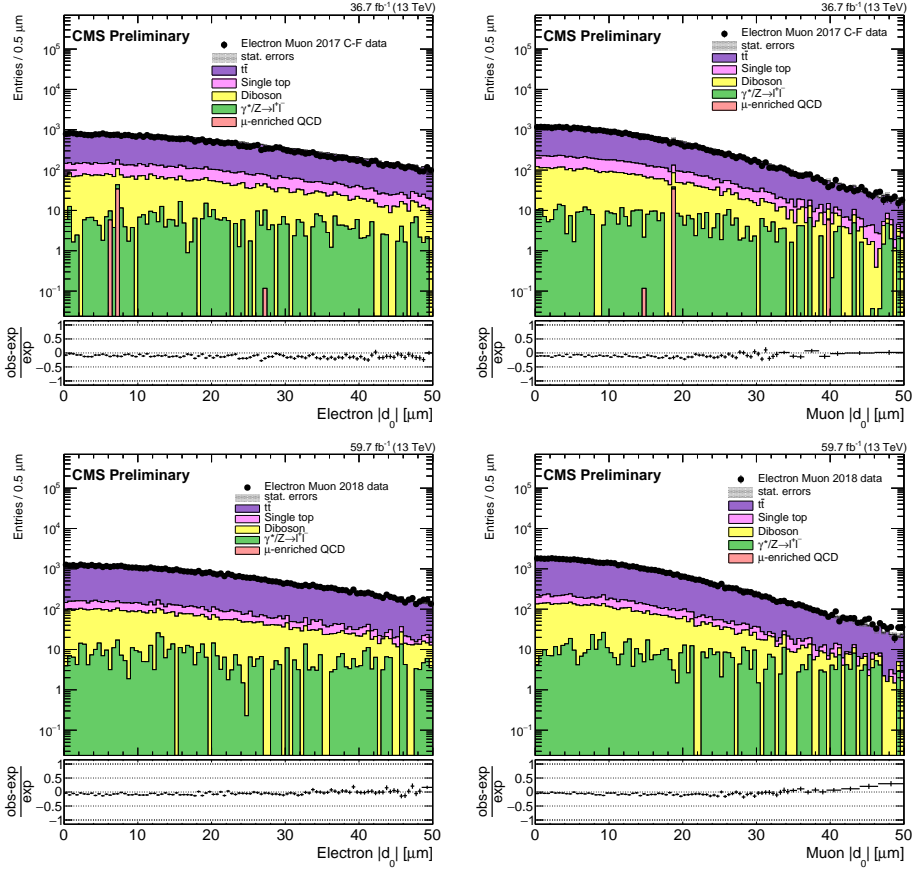


Figure 3.18: The corrected lepton  $|d_0|$  distributions in the  $e\mu$  prompt control region, for electrons (left) and muons (right), for 2017 data and simulation (top), and 2018 data and simulation (bottom). The rightmost bin in each plot contains the overflow entries.

1123     This  $d_0$  smearing has a minimal effect on the final result because the width of the  
1124     Gaussian distribution from which the smearing values are drawn is small relative to  
1125     the size of the signal region bins, but understanding the source of the poor agreement  
1126     between data and simulation was important to validate our understanding of the SM  
1127     background.

### 1128     **3.4.4 Trigger efficiency**

1129     We also apply scale factors to the simulated background and signal events to cor-  
1130     rect for differences in trigger efficiency between data and simulation. To measure the  
1131     trigger efficiency, we first require that events pass an OR of several unprescaled  $p_T^{\text{miss}}$   
1132     triggers (see Table 3.9) and the preselection criteria with the lepton  $p_T$  requirement  
1133     excluded. The  $p_T^{\text{miss}}$  triggers provide a sample of di-lepton events that is unbiased  
1134     with respect to the main triggers used in the analysis, and excluding the lepton  $p_T$   
1135     requirement allows us to study the trigger efficiency as a function of lepton  $p_T$ . In  
1136     the  $e\mu$  channel, the electron (muon)  $p_T$  is required to be greater than 50 GeV when  
1137     plotting against the muon (electron)  $p_T$  to disentangle the effect from the other leg of  
1138     the muon-photon trigger. Data events are taken from the MET primary dataset (which  
1139     contains events that pass  $p_T^{\text{miss}}$  triggers) and simulated background events are taken  
1140     from  $t\bar{t}$  simulation for the  $e\mu$  channel and Drell-Yan simulation for the same-flavor  
1141     channels.

1142     To calculate the efficiency, we divide the lepton  $p_T$  distribution in events that  
1143     pass the standard analysis triggers in addition to the OR of the  $p_T^{\text{miss}}$  triggers and  
1144     the preselection by the lepton  $p_T$  distribution in events that pass the OR of the  
1145      $p_T^{\text{miss}}$  triggers and the preselection. We then compute the scale factor as the ratio of

Table 3.9: The unprescaled  $p_T^{\text{miss}}$  triggers used to create an orthogonal data sample for the trigger efficiency calculation.

---

<b>2016</b>
HLT_MET200
HLT_MonoCentralPFJet80_PFMETNoMu110_PFMHTNoMu110_IDTight
HLT_PFMET120_PFMHT120_IDTight
HLT_PFMET170_HBHECleaned
HLT_PFMET300
HLT_PFMETNoMu120_PFMHTNoMu120_IDTight
<b>2017</b>
HLT_CaloMET350_HBHECleaned
HLT_MonoCentralPFJet80_PFMETNoMu120_PFMHTNoMu120_IDTight
HLT_PFMET120_PFMHT120_IDTight
HLT_PFMET250_HBHECleaned
HLT_PFMETNoMu120_PFMHTNoMu120_IDTight
<b>2018</b>
HLT_CaloMET350_HBHECleaned
HLT_MonoCentralPFJet80_PFMETNoMu120_PFMHTNoMu120_IDTight
HLT_PFMET120_PFMHT120_IDTight
HLT_PFMET200_HBHE_BeamHaloCleaned
HLT_PFMET250_HBHECleaned
HLT_PFMETNoMu120_PFMHTNoMu120_IDTight

---

Table 3.10: The trigger efficiency scale factors in each channel and year.

	2016	2017	2018
$e\mu$ channel, electrons	$0.974 \pm 0.016$	$0.961 \pm 0.013$	$0.965 \pm 0.012$
$e\mu$ channel, muons	$0.975 \pm 0.016$	$0.972 \pm 0.014$	$0.967 \pm 0.012$
$ee$ channel	$1.000 \pm 0.099$	$1.000 \pm 0.131$	$1.000 \pm 0.185$
$\mu\mu$ channel	$0.956 \pm 0.012$	$0.930 \pm 0.010$	$0.935 \pm 0.011$

<sup>1146</sup> the efficiency in data to the efficiency in simulation in the plateau of the efficiency  
<sup>1147</sup> distribution. The  $e\mu$  channel efficiency distributions are shown in Fig. 3.19, and the  
<sup>1148</sup> resulting scale factors for all channels are listed in Table 3.10.

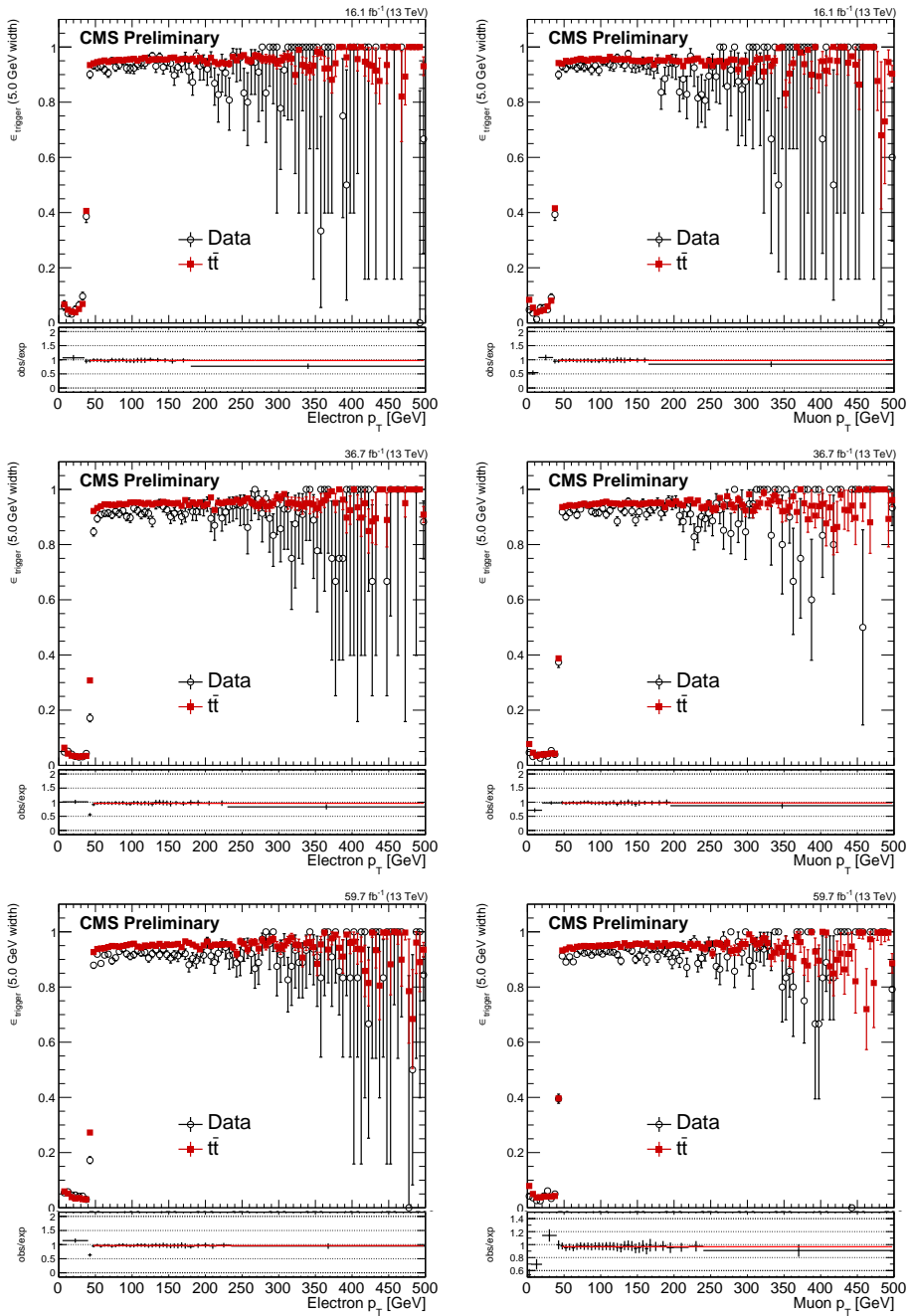


Figure 3.19: Trigger efficiency as a function of leading electron (left) or leading muon (right)  $p_T$  in the  $e\mu$  channel in 2016 (top), 2017 (middle), and 2018 (bottom) in data and simulated background  $t\bar{t}$  events.

1149 **3.5 Background estimation**

1150 **3.5.1 Background sources**

1151 The vast majority of leptons from SM processes are prompt. There are, however,  
1152 a few notable processes that produce leptons with large  $|d_0|$  values that may pass the  
1153 preselection: (1) leptons from prompt decays whose  $|d_0|$  is poorly measured (“mis-  
1154 measurements”), (2) leptons from decays of tau leptons (“taus”), and (3) leptons  
1155 from decays of B or D mesons (“heavy flavor”). Note that the leptons from these  
1156 processes generally do not share a common displaced vertex. We perform several cross  
1157 checks to ensure that processes in which leptons share a common displaced vertex do  
1158 not contribute significantly in the signal regions (SRs). Section 3.5.6 presents several  
1159 additional studies that confirm that the SR contributions of leptons from material  
1160 interactions, cosmic rays, and SM hadrons are either negligible or already accounted  
1161 for by the background estimation procedure outlined in Section 3.5.2.

1162 The  $|d_0|$  distributions of leptons from the three main background sources vary  
1163 according to lepton flavor and parent particle. Tau leptons, B mesons, and D mesons  
1164 have proper decay lengths of 87  $\mu\text{m}$ , approximately 500  $\mu\text{m}$ , and approximately  
1165 100  $\mu\text{m}$ , respectively, so leptons from taus will generally be less displaced than leptons  
1166 from heavy flavor. Furthermore, mismeasurements are more common for electrons  
1167 than for muons due to the superior muon  $d_0$  resolution. Figure 3.20, which shows  
1168 the relative contribution of each source of leptons as a function of  $|d_0|$  in simulated  $t\bar{t}$   
1169 events that pass the  $e\mu$  channel preselection, shows how mismeasurements dominate  
1170 at all  $|d_0|$  values for electrons while taus and heavy-flavor contribute meaningfully for  
1171 muons with  $|d_0| \gtrsim 100 \mu\text{m}$ .

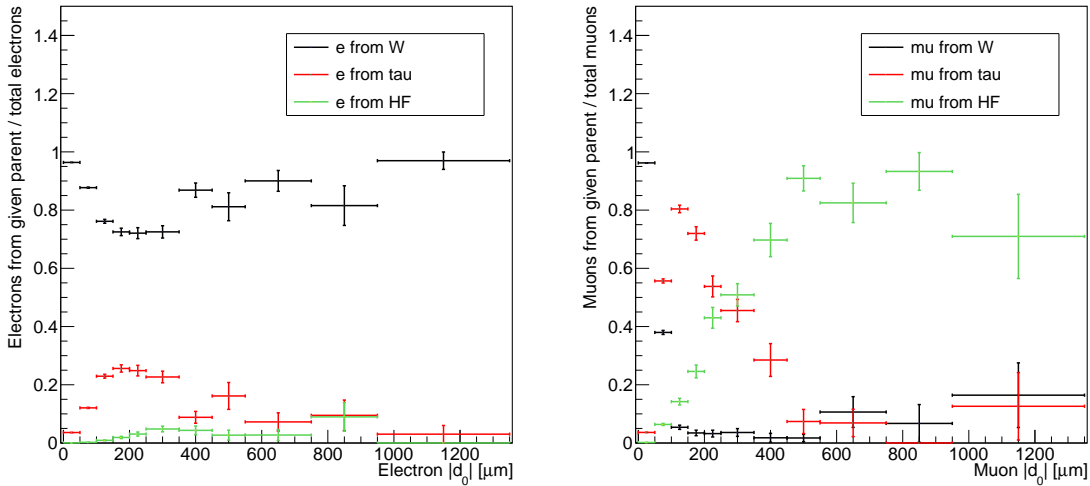


Figure 3.20: The fraction of electrons (left) and muons (right) from different parents as a function of lepton  $|d_0|$  in simulated  $t\bar{t}$  events that pass the 2018  $e\mu$  channel preselection. Note that the vast majority of leptons whose parent is a W boson are produced in prompt decays.

1172        In addition to the  $|d_0|$  behavior of individual leptons, we are also interested in un-  
 1173      derstanding whether any background processes introduce correlation in  $|d_0|$  between  
 1174      pairs of leptons. Having confirmed that the obvious potential source of  $|d_0|$ - $|d_0|$  corre-  
 1175      lation, i.e. pairs of leptons that share a common displaced vertex, do not contribute  
 1176      meaningfully to the SR, we next investigate possible sources of correlation from mis-  
 1177      measurements, taus, and heavy flavor. As the preselection criteria ensure that we are  
 1178      operating in the regime in which lepton  $|d_0|$  resolution does not depend meaningfully  
 1179      on  $p_T$  or  $\eta$ , and because the two candidate leptons in a given event are nearly always  
 1180      from prompt processes and/or independent decays, mismeasurements generally will  
 1181      not introduce  $|d_0|$ - $|d_0|$  correlation.

1182 Taus and heavy flavor, on the other hand, could potentially introduce  $|d_0|$ - $|d_0|$  cor-  
1183 relation through correlation in parentage between the two candidate leptons. As will  
1184 be shown in Section 3.5.3, we find that taus lead to exactly this type of correlation  
1185 through processes such as  $Z \rightarrow \tau\tau \rightarrow ll$  while heavy flavor does not. Figure 3.21 shows  
1186 the fraction of muons from different SM parents as a function of  $|d_0|$  in simulated  
1187 Drell-Yan events that pass the  $\mu\mu$  preselection with the added requirement that both  
1188 muons come from the same type of parent particle. Here, we see the same character-  
1189 istic  $|d_0|$  behavior of leptons from taus and also that the isolation criteria effectively  
1190 eliminates events in which both leptons come from a heavy flavor meson. We there-  
1191 fore conclude that while leptons from mismeasurements, taus, and heavy flavor will  
1192 all contribute in the SR, only leptons from taus will introduce meaningful  $|d_0|$ - $|d_0|$   
1193 correlation. Furthermore, the characteristic  $|d_0|$  behavior of leptons from taus seen  
1194 in Figs. 3.20 and 3.21 implies that this correlation will specifically impact the 100 to  
1195 500  $\mu\text{m}$  region.

### 1196 3.5.2 Data-driven ABCD method

1197 We estimate the SR background yields with a data-driven method in which the lep-  
1198 ton  $|d_0|$  distributions serve as composite models of all background processes. Specif-  
1199 ically, we employ an ABCD method using the  $|d_0|$  of two leptons. We label the two  
1200  $|d_0|$  values in each channel as  $|d_0^a|$  and  $|d_0^b|$ , which correspond to the leading electron  
1201 and leading muon in the  $e\mu$  channel, the leading and subleading electrons in the  $ee$   
1202 channel, and the leading and subleading muons in the  $\mu\mu$  channel. As a first step,  
1203 we categorize the events that pass the preselection criteria into four regions (A, B, C,  
1204 and D) of the  $|d_0^a|$ - $|d_0^b|$  plane, as shown in Fig. 3.22.

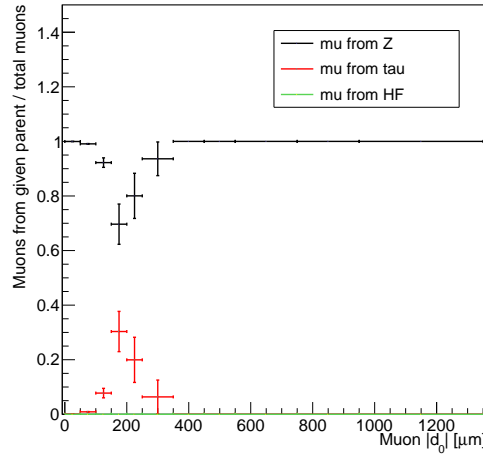


Figure 3.21: The fraction of muons from different parents as a function of muon  $|d_0|$  in simulated Drell-Yan events that pass the 2018  $\mu\mu$  channel preselection and the additional constraint that the leading and subleading muon both come from the same type of parent particle.

1205 In order to maximize sensitivity to a wide range of new particle lifetimes, we  
 1206 subdivide region D into four SRs:

- 1207 • SR I:  $100 \leq |d_0^a| < 500 \mu\text{m}$ ,  $100 < |d_0^b| < 500 \mu\text{m}$
- 1208 • SR II:  $100 \leq |d_0^a| < 500 \mu\text{m}$ ,  $500 \mu\text{m} < |d_0^b| < 10 \text{ cm}$
- 1209 • SR III:  $500 \mu\text{m} \leq |d_0^a| < 10 \text{ cm}$ ,  $100 < |d_0^b| < 500 \mu\text{m}$
- 1210 • SR IV:  $500 \mu\text{m} \leq |d_0^a| < 10 \text{ cm}$ ,  $500 \mu\text{m} < |d_0^b| < 10 \text{ cm}$

1211 The exact boundaries between the four SRs are motivated by the expected contribu-  
 1212 tions of the different background sources, as explained in 3.5.1. This approach also  
 1213 necessitates that the definitions of regions B and C vary in accordance with the SR for  
 1214 which a given estimate is performed (e.g. only the events in the  $100 \leq |d_0^a| < 500 \mu\text{m}$   
 1215 range of region B are considered when estimating the yields of SR I and II). Finally,

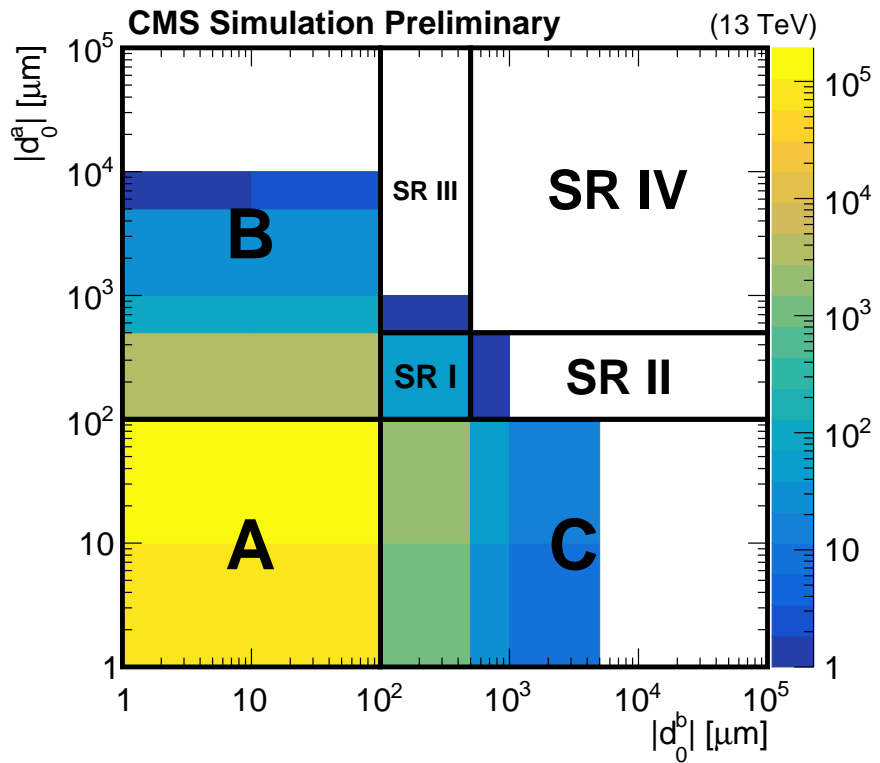


Figure 3.22: A diagram of the ABCD method overlaid on simulated background events passing the 2018  $e\mu$  preselection. A, B, and C are control regions, and D corresponds to the inclusive SR, which includes SRs I, II, III, and IV. Underflow events are included in the bins along the left and bottom edges. When performing the background estimate, regions B and C are further subdivided to coincide with the SR for which the estimate is being performed.

Table 3.11: The  $p_T$  boundaries between the low- and high- $p_T$  bins of SR I in each channel.

	$p_T$ boundary [GeV]
2016 $e\mu$	leading $\mu$ $p_T = 90$
2017+2018 $e\mu$	leading $\mu$ $p_T = 140$
2016 $ee$	leading $e$ $p_T = 300$
2017+2018 $ee$	leading $e$ $p_T = 400$
2016 $\mu\mu$	leading $\mu$ $p_T = 100$
2017+2018 $\mu\mu$	leading $\mu$ $p_T = 100$

1216 we subdivide SR I into two bins using one lepton's  $p_T$  to further increase sensitivity to  
 1217 high-mass, low-lifetime new physics. Table 3.11 lists the  $p_T$  boundary in each channel  
 1218 and year.

1219 We then use the number of events in regions A, B, and C to estimate the expected  
 1220 background in each SR. The basic estimation procedure depends on the assumption  
 1221 that  $|d_0^a|$  and  $|d_0^b|$  are uncorrelated. If this assumption holds, then  $N_B/N_A = N_D/N_C$   
 1222 and the number of background events in D is equal to  $N_B \times N_C/N_A$ , where  $N_X$  is  
 1223 the number of background events in the given region. We find that  $|d_0^a|$  and  $|d_0^b|$  are  
 1224 indeed uncorrelated over much of the  $|d_0|-|d_0|$  plane, but the correlation discussed  
 1225 in Section 3.5.1 renders the simple ABCD method insufficient to estimate the back-  
 1226 ground in SR I. After quantifying the degree of correlation in Section 3.5.3, we define  
 1227 a procedure to correct the simple SR I ABCD estimate in Section 3.5.4.

1228 When performing the background estimate and closure tests, we treat the 2016  
 1229 data and simulation separately from the 2017–2018 data and simulation to avoid  
 1230 any correlations between  $|d_0^a|$  and  $|d_0^b|$  that may arise from the differences between

1231 the original and Phase-1 pixel detectors employed by CMS in 2016 and 2017–2018,  
1232 respectively (see Section 2.2.2).

### 1233 3.5.3 Closure tests in control regions

1234 We perform several closure tests of the background estimation procedure in data  
1235 and simulation to test the method and quantify the degree of  $|d_0^a|$ - $|d_0^b|$  correlation  
1236 from the processes discussed in 3.5.1. Two series of tests are performed, the first in  
1237 the 100–500  $\mu\text{m}$  subregions of regions B and C and the second in the 500  $\mu\text{m}$ –10 cm  
1238 subregions of regions B and C.

#### 1239 100–500 $\mu\text{m}$ tests

1240 We perform closure tests in subregions of regions B and C where one lepton is  
1241 more prompt (20–100  $\mu\text{m}$ ) and the other is more displaced (100–500  $\mu\text{m}$ ). In these  
1242 closure tests, we estimate the background yield using the simple ABCD method and  
1243 use the ratio of the actual number of events to the estimated number of events as  
1244 a measure of nonclosure (and therefore  $|d_0^a|$ - $|d_0^b|$  correlation). With this approach, a  
1245 ratio of 1 corresponds to closure and negligible correlation while ratios greater than  
1246 1 correspond to nonclosure and positive correlation. To understand how the degree  
1247 of correlation varies with  $|d_0|$ , we perform several closure tests in each sideband while  
1248 varying the  $|d_0|$  range of the more-prompt lepton and fit the resulting ratios with a  
1249 first-degree polynomial. We then extrapolate the resulting fit from the closure test  
1250 regions to SR I to estimate the degree of nonclosure in SR I. We perform identical  
1251 procedures in regions B and C and then average the resulting extrapolated ratios.

1252 Table 3.12 shows the average extrapolated ratios for three rounds of closure tests:  
1253 one in background simulation with the  $Z \rightarrow \tau\tau \rightarrow ll$  events removed, one in the full

Table 3.12: Closure test results in data and background simulation in the 100–500  $\mu\text{m}$  region. The average extrapolated ratios and their statistical uncertainties are given. For each test, the A, B, C, and D regions are defined as follows: A is 20–30  $\mu\text{m}$  in prompt lepton  $|d_0|$  and 20–100  $\mu\text{m}$  in displaced lepton  $|d_0|$ , B is 20–30  $\mu\text{m}$  in prompt lepton  $|d_0|$  and 100–500  $\mu\text{m}$  in displaced lepton  $|d_0|$ , C is always 20–100  $\mu\text{m}$  in displaced lepton  $|d_0|$ , D (the test region) is always 100–500  $\mu\text{m}$  in displaced lepton  $|d_0|$ , and we perform repeated tests while simultaneously varying the C and D prompt lepton  $|d_0|$  within the 30–100  $\mu\text{m}$  range.

	Bkg. simulation without $Z \rightarrow \tau\tau \rightarrow ll$	Full bkg. simulation	Data
2016 $e\mu$	$0.9 \pm 0.3$	$1.6 \pm 0.6$	$0.9 \pm 1.3$
2017+2018 $e\mu$	$1.1 \pm 0.4$	$1.6 \pm 0.7$	$3.1 \pm 1.0$
2016 $ee$	$0.8 \pm 0.5$	$0.8 \pm 0.5$	$0.6 \pm 0.6$
2017+2018 $ee$	$0.8 \pm 1.0$	$1.6 \pm 0.9$	$1.5 \pm 0.4$
2016 $\mu\mu$	$1.1 \pm 0.8$	$2.0 \pm 0.8$	$2.5 \pm 1.0$
2017+2018 $\mu\mu$	$2.6 \pm 2.8$	$7.8 \pm 3.7$	$4.2 \pm 1.8$
Average	$1.2 \pm 0.5$	$2.6 \pm 0.7$	$2.1 \pm 0.5$

1254 background simulation, and one in data. The average extrapolated ratios are always  
 1255 compatible with one in background simulation without  $Z \rightarrow \tau\tau \rightarrow ll$  events, but they  
 1256 generally increase when the  $Z \rightarrow \tau\tau \rightarrow ll$  events are included. Furthermore, the average  
 1257 extrapolated ratios from the full background simulation generally describe the average  
 1258 extrapolated ratios in data. From these results, we conclude that within our statistical  
 1259 uncertainties,  $Z \rightarrow \tau\tau \rightarrow ll$  events are the only meaningful source of correlation and that  
 1260 the degree of correlation observed in data is modeled reasonably well in simulation.  
 1261 We also observe that the variation in the degree of correlation across channels matches  
 1262 our expectations: correlation increases with the number of muons in the final state  
 1263 and is greater in 2017–2018 than 2016 because of the improved  $d_0$  resolution made  
 1264 possible by the Phase-1 tracker upgrade (described in Section 2.2.2).

1265 **500  $\mu\text{m}$ –10 cm tests**

1266 We next perform closure tests in more-displaced subregions of regions B and  
1267 C where one lepton is more prompt (20–100  $\mu\text{m}$ ) and the other is more displaced  
1268 (500  $\mu\text{m}$ –10 cm). We again use the ratio of the actual number of events to the esti-  
1269 mated number of events as the measure of nonclosure, but in these tests we expect  
1270 the ratio to be consistent with one because  $Z \rightarrow \tau\tau \rightarrow ll$  events do not contribute mean-  
1271 ingfully beyond 500  $\mu\text{m}$ . Table 3.13 shows that this is indeed the case for background  
1272 simulation (with and without  $Z \rightarrow \tau\tau \rightarrow ll$  events) and for data. These results imply  
1273 that  $|d_0^a|$  and  $|d_0^b|$  are uncorrelated beyond 500  $\mu\text{m}$ , which means that a simple ABCD  
1274 procedure will be adequate for estimating the background yields in SRs II, III, and  
1275 IV.

1276 **3.5.4 ABCD correction and systematic uncertainty**

1277 The closure tests of Section 3.5.3 show that  $|d_0^a|$  and  $|d_0^b|$  are frequently positively  
1278 correlated in the 100–500  $\mu\text{m}$  region but are uncorrelated otherwise. To account for  
1279 this correlation as well as other possible unforeseen sources of nonclosure, we define  
1280 a procedure to correct the simple ABCD estimate in SR I and assign a systematic  
1281 uncertainty to the simple ABCD estimate in all SRs.

1282 **100–500  $\mu\text{m}$  correction and systematic uncertainty**

1283 Figures 3.23, 3.24, and 3.25 show the results of the data closure tests in the  $e\mu$   
1284  $ee$ , and  $\mu\mu$  channels, respectively, in the one-prompt (20–100  $\mu\text{m}$ )/one-displaced (100-  
1285 500  $\mu\text{m}$ ) sidebands. These plots show the ratio of the actual to the estimated number  
1286 of events as a function of the prompt lepton  $|d_0|$ . In all of these plots, the binning of  
1287 the prompt lepton axis is initially 10  $\mu\text{m}$  wide. Starting from most-displaced bin, we

Table 3.13: Closure test results in data and background simulation in the  $500\text{ }\mu\text{m}$ – $10\text{ cm}$  region. The ratios of the actual to the estimated yield and their statistical uncertainties are given. The A, B, C, and D regions are defined as follows: A is  $20$ – $30\text{ }\mu\text{m}$  in prompt lepton  $|d_0|$  and  $20$ – $100\text{ }\mu\text{m}$  in displaced lepton  $|d_0|$ , B is  $20$ – $30\text{ }\mu\text{m}$  in prompt lepton  $|d_0|$  and  $500\text{ }\mu\text{m}$ – $10\text{ cm}$  in displaced lepton  $|d_0|$ , C is  $30$ – $100\text{ }\mu\text{m}$  in prompt lepton  $|d_0|$  and  $20$ – $100\text{ }\mu\text{m}$  in displaced lepton  $|d_0|$ , and D (the test region) is  $30$ – $100\text{ }\mu\text{m}$  in prompt lepton  $|d_0|$  and  $500\text{ }\mu\text{m}$ – $10\text{ cm}$  in displaced lepton  $|d_0|$ .

Region B			
	Bkg. simulation without $Z \rightarrow \tau\tau \rightarrow ll$	Bkg. simulation	Data
2016 $e\mu$	$1.1^{+0.3}_{-0.3}$	$1.1^{+0.3}_{-0.3}$	$0.4^{+1.0}_{-0.4}$
2017+2018 $e\mu$	$0.9^{+0.3}_{-0.2}$	$0.9^{+0.3}_{-0.2}$	$0.7^{+0.3}_{-0.3}$
2016 $ee$	$0.4^{+0.6}_{-0.3}$	$0.4^{+0.6}_{-0.3}$	$1.4^{+1.6}_{-0.9}$
2017+2018 $ee$	$0.5^{+0.8}_{-0.4}$	$0.3^{+0.4}_{-0.2}$	$1.0^{+0.3}_{-0.3}$
2016 $\mu\mu$	$0.7^{+0.3}_{-0.3}$	$0.7^{+0.3}_{-0.3}$	$0.8^{+0.3}_{-0.3}$
2017+2018 $\mu\mu$	$0.8^{+1.8}_{-0.7}$	$0.4^{+1.0}_{-0.4}$	$1.8^{+0.6}_{-0.7}$

Region C			
	Bkg. simulation without $Z \rightarrow \tau\tau \rightarrow ll$	Bkg. simulation	Data
2016 $e\mu$	$0.8^{+0.4}_{-0.3}$	$0.8^{+0.4}_{-0.3}$	$1.0$ (0 vs 0)
2017+2018 $e\mu$	$0.8^{+0.3}_{-0.2}$	$0.8^{+0.3}_{-0.2}$	$0.7^{+1.3}_{-0.7}$
2016 $ee$	$4.0^{+5.8}_{-3.1}$	$4.0^{+5.8}_{-3.1}$	$0.7^{+1.0}_{-0.6}$
2017+2018 $ee$	$3.5^{+2.6}_{-1.8}$	$2.1^{+2.6}_{-1.5}$	$1.0^{+0.3}_{-0.3}$
2016 $\mu\mu$	$1.2^{+0.5}_{-0.4}$	$1.3^{+0.6}_{-0.4}$	$0.6^{+0.4}_{-0.3}$
2017+2018 $\mu\mu$	$0.4^{+0.4}_{-0.3}$	$0.5^{+0.5}_{-0.3}$	$0.5^{+0.3}_{-0.2}$

1288 test to see if any bin has fewer than 5 events, and if so, we combine it with whichever  
1289 neighboring bin has fewer events, repeating until all bins have at least 5 events.

1290 In each of the two sidebands, we then fit the resulting ratios with a straight  
1291 line, where the slope and y-intercept are allowed to vary, and extrapolate the fit to  
1292 200  $\mu\text{m}$ , which is where we expect the largest contribution from tau lepton decays (see  
1293 Section 3.5.1). 200  $\mu\text{m}$  also happens to be approximately the center-of-mass of the  
1294 100–500  $\mu\text{m}$  bin in background simulation. We average the two extrapolated ratios  
1295 and derive a correction and systematic uncertainty from this average extrapolated  
1296 ratio.

1297 If the average extrapolated ratio is  $> 1.0$ , we take the central value as a multi-  
1298 plicative correction to the background estimate and the uncertainty in the average as  
1299 a systematic uncertainty in the background estimate. In this case, we also vary the  
1300 200  $\mu\text{m}$  extrapolation point by  $\pm 50 \mu\text{m}$  (the approximate width of the peak in the tau  
1301 lepton contribution as a function of  $|d_0|$ ). We apply the difference from this varia-  
1302 tion in extrapolation point as an additional systematic uncertainty in the background  
1303 estimate. If the average is  $\leq 1.0$ , we set the correction equal to 1.0 and use the un-  
1304 certainty in the average as a symmetric systematic uncertainty about 1.0. Table 3.14  
1305 shows the resulting correction factors along with the uncorrected and corrected SR I  
1306 background estimate.

### 1307 **500 $\mu\text{m}$ –10 cm systematic uncertainty**

1308 In the 500  $\mu\text{m}$ –10 cm region, we derive a systematic uncertainty in the background  
1309 estimate from the data closure tests shown in Section 3.5.3. We take the largest  
1310 deviation from 1.0 that occurs in the ratio of the actual to the estimated number  
1311 of events plus its uncertainty, in either of the two closure tests that correspond to a

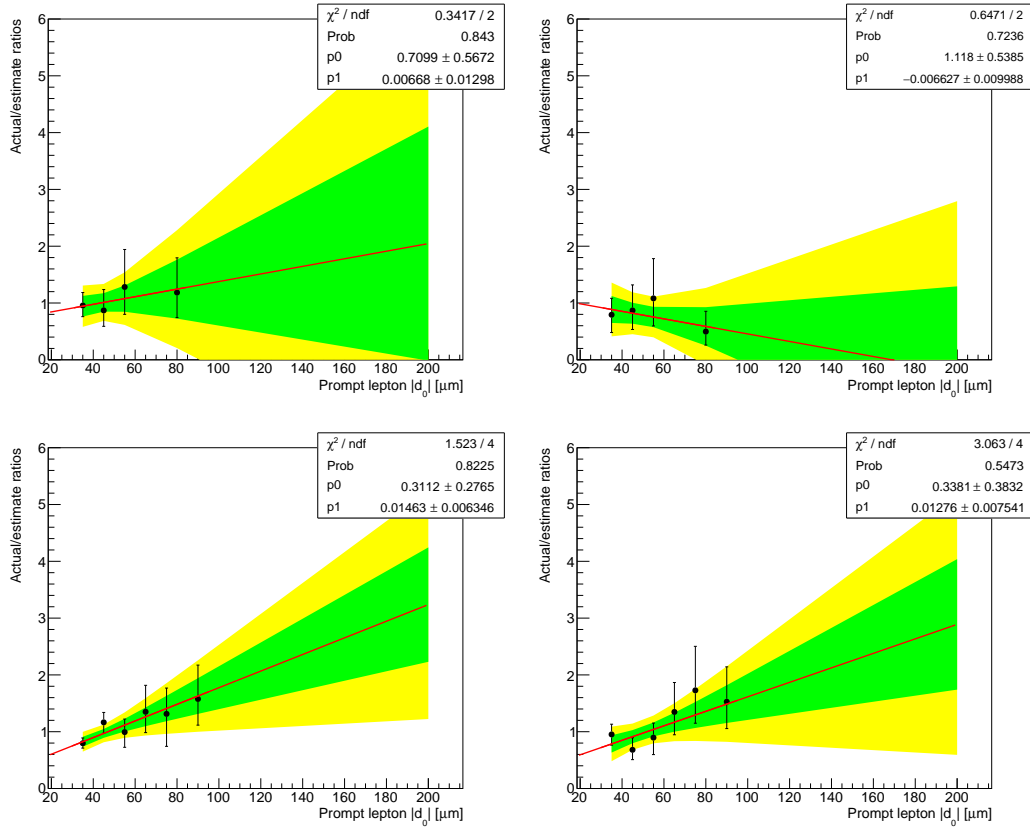


Figure 3.23: Background estimation closure tests in data, in  $100\text{--}500\,\mu\text{m}$  subregions of regions B (left) and C (right) in the  $e\mu$  channel. Each plot shows the ratio of the actual to the estimated number of events as a function of the prompt lepton  $|d_0|$  in 2016 (top) and 2017–18 (bottom). A linear fit is shown in black along with the 68 % and 95 % confidence intervals of the extrapolated fit value.

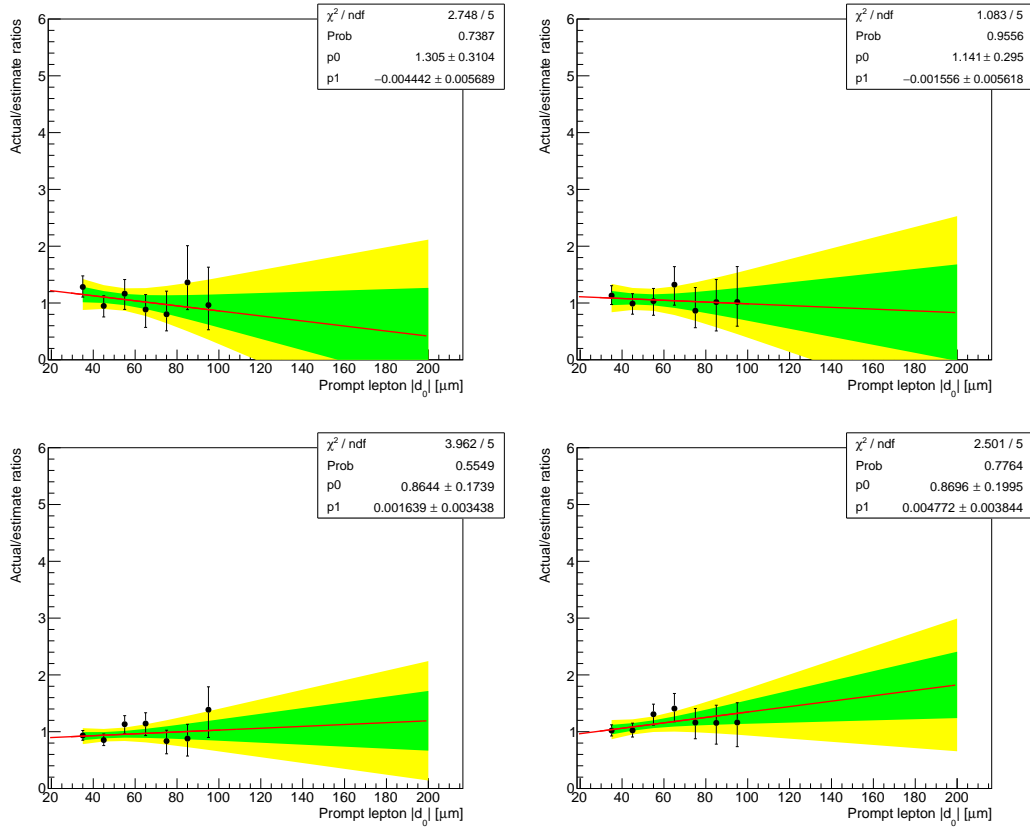


Figure 3.24: Background estimation closure tests in data, in  $100\text{--}500\,\mu\text{m}$  subregions of regions B (left) and C (right) in the  $ee$  channel. Each plot shows the ratio of the actual to the estimated number of events as a function of the prompt lepton  $|d_0|$  in 2016 (top) and 2017–18 (bottom). A linear fit is shown in black along with the 68 % and 95 % confidence intervals of the extrapolated fit value.

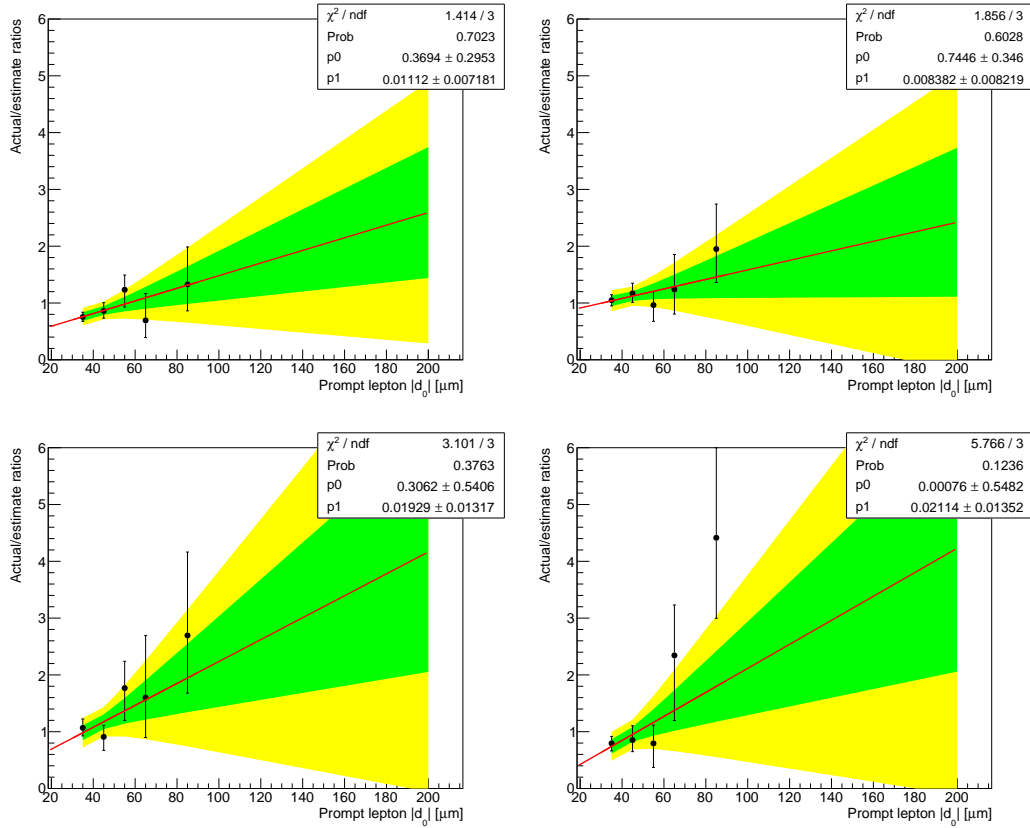


Figure 3.25: Background estimation closure tests in data, in 100–500  $\mu\text{m}$  subregions of regions B (left) and C (right) in the  $\mu\mu$  channel. Each plot shows the ratio of the actual to the estimated number of events as a function of the prompt lepton  $|d_0|$  in 2016 (top) and 2017–18 (bottom). A linear fit is shown in black along with the 68 % and 95 % confidence intervals of the extrapolated fit value.

Table 3.14: The correction factors and the uncorrected and corrected background estimates in SR I . The correction factor uncertainties include both the uncertainty in the average and the additional uncertainty obtained from varying the fit extrapolation point. The total uncertainty (statistical plus systematic) is given for the corrected background estimates.

	Correction factor	Uncorrected estimate	Corrected estimate
2016 $e\mu$	$1.0^{+1.3}_{-1.0}$	$4.21^{+0.38}_{-0.40}$	$4.2^{+5.4}_{-4.2}$
2017+2018 $e\mu$	$3.0 \pm 1.0$	$12.53^{+0.64}_{-0.61}$	$38 \pm 13$
2016 $ee$	$1.00 \pm 0.60$	$18.30^{+0.94}_{-0.91}$	$18 \pm 11$
2017+2018 $ee$	$1.51^{+0.43}_{-0.42}$	$41.6 \pm 1.3$	$63^{+18}_{-17}$
2016 $\mu\mu$	$2.5 \pm 1.0$	$3.07 \pm 0.08$	$7.7 \pm 3.1$
2017+2018 $\mu\mu$	$4.2 \pm 1.8$	$1.00 \pm 0.04$	$4.2 \pm 1.8$

given SR, as a systematic uncertainty. This is a conservative approach that produces a large systematic uncertainty in the small background yields that we predict in these regions. Table 3.15 shows the systematic uncertainty and the predicted number of events in SRs II, III, and IV.

### 3.5.5 Testing full background estimation procedure

Having defined the full background estimation procedure and seen that the  $|d_0^a|$ - $|d_0^b|$  correlation observed in data is also present in simulated background events, we now perform a final closure test of the full background estimation method using simulated background events in SRs I–IV.

Table 3.16 shows the estimated and actual number of simulated background events in SRs I–IV. The listed estimates include all corrections and statistical and systematic uncertainties as discussed in 3.5.4. The uncertainties in the actual values are

Table 3.15: The systematic uncertainty and the background estimates in SRs II, III, and IV. The total uncertainty (statistical plus systematic) is given for each estimate.

	Systematic uncertainty	SR II	SR III	SR IV
2016 $e\mu$	98%	$0.15 \pm 0.15$	$0.09^{+0.12}_{-0.09}$	$0.003^{+0.004}_{-0.003}$
2017+2018 $e\mu$	106%	$0.71^{+0.76}_{-0.71}$	$0.23^{+0.27}_{-0.23}$	$0.01^{+0.02}_{-0.01}$
2016 $ee$	199%	$0.51^{+1.02}_{-0.51}$	$0.43^{+0.85}_{-0.43}$	$0.01^{+0.02}_{-0.01}$
2017+2018 $ee$	37%	$3.6 \pm 1.4$	$2.8 \pm 1.1$	$0.24^{+0.10}_{-0.09}$
2016 $\mu\mu$	64%	$0.17 \pm 0.11$	$0.19 \pm 0.12$	$0.01 \pm 0.01$
2017+2018 $\mu\mu$	140%	$0.14^{+0.19}_{-0.14}$	$0.08^{+0.12}_{-0.08}$	$0.01^{+0.02}_{-0.01}$

1324 purely statistical. The general agreement between estimated and actual yields leads  
 1325 us to conclude that the background estimation procedure is valid and the assigned  
 1326 systematic uncertainties are sufficient to cover any potential sources of nonclosure  
 1327 that we have not explicitly considered.

### 1328 3.5.6 Additional background checks

1329 We perform a few additional studies to check for other potential sources of back-  
 1330 ground. We find that their SR contributions are either negligible or already covered  
 1331 by the background estimation method described above.

#### 1332 Material interactions

1333 In order to further study the material interactions, we invert the preselection  
 1334 criterion that rejects good vertices in the material. In data, we find seven events,  
 1335 across all channels and years, that pass the preselection with this inverted criterion.  
 1336 As shown in Table 3.17, three of these events are in the prompt control region and

Table 3.16: Closure test results in background simulation in the SRs with all background estimate corrections and uncertainties applied. The estimated number of events, the actual number of events, and their total uncertainties (statistical plus systematic) are given. In cases where the actual number of events is zero, the uncertainty is given by the product of the average background simulation event weight and the upper bound of the 68% Poisson interval given by a single observation of zero events.

	SR I	SR II	SR III	SR IV
2016 $e\mu$ estimated	$7.4^{+4.8}_{-4.2}$	$0.07 \pm 0.07$	$0.096^{+0.105}_{-0.096}$	$0.001 \pm 0.001$
2016 $e\mu$ actual	$5.0^{+1.5}_{-1.2}$	$0.07^{+0.09}_{-0.05}$	$0.005^{+0.011}_{-0.004}$	$0.000^{+0.037}_{-0.000}$
2017+2018 $e\mu$ estimated	$13.5 \pm 6.4$	$0.37^{+0.40}_{-0.37}$	$0.34^{+0.36}_{-0.34}$	$0.02 \pm 0.02$
2017+2018 $e\mu$ actual	$19.1^{+11.4}_{-7.6}$	$0.52^{+0.41}_{-0.25}$	$0.00^{+0.24}_{-0.00}$	$0.00^{+0.24}_{-0.00}$
2016 $ee$ estimated	$9.3 \pm 5.0$	$0.12^{+0.23}_{-0.12}$	$0.14^{+0.28}_{-0.14}$	$0.002^{+0.004}_{-0.002}$
2016 $ee$ actual	$13.4^{+3.4}_{-2.8}$	$0.15^{+0.19}_{-0.09}$	$1.03^{+1.36}_{-0.67}$	$0.000^{+0.550}_{-0.000}$
2017+2018 $ee$ estimated	$18 \pm 11$	$0.59^{+0.27}_{-0.26}$	$0.45^{+0.21}_{-0.20}$	$0.02 \pm 0.01$
2017+2018 $ee$ actual	$8.2^{+6.5}_{-3.9}$	$0.17^{+0.23}_{-0.11}$	$0.00^{+0.17}_{-0.00}$	$0.00^{+0.17}_{-0.00}$
2016 $\mu\mu$ estimated	$1.3 \pm 0.6$	$0.04 \pm 0.04$	$0.03 \pm 0.03$	$0.002 \pm 0.002$
2016 $\mu\mu$ actual	$3.3^{+1.8}_{-1.2}$	$0.11^{+0.14}_{-0.07}$	$0.06^{+0.14}_{-0.05}$	$0.000^{+0.110}_{-0.000}$
2017+2018 $\mu\mu$ estimated	$2.7 \pm 1.4$	$0.04 \pm 0.04$	$0.02 \pm 0.02$	$0.002 \pm 0.002$
2017+2018 $\mu\mu$ actual	$7.1^{+6.9}_{-3.8}$	$0.00^{+0.15}_{-0.00}$	$0.00^{+0.15}_{-0.00}$	$0.078^{+0.179}_{-0.064}$

1337 four are in region B or region C. The lepton vertices in these events coincide with the  
 1338 material as we expect: two are in the beampipe, one is in the pixel detector inner  
 1339 shield, and four are in the first layer of the pixel detector. Even with the material  
 1340 interaction veto inverted, we find no SR events resulting from material interactions  
 1341 and therefore conclude that material interactions are not a significant background  
 1342 after the full selection is applied.

Table 3.17: Some properties of the seven events found in data with the material interactions selection inverted.

Channel, Era	$( d_0^a ,  d_0^b )$ [μm]	Region	Vertex (x, y, z) [cm]	Material
$e\mu$ , 2017C	(-14, -10)	A	(-2.5, 1.4, 6.8)	pixel L1
$e\mu$ , 2018D	(46, -14)	A	(0.9, 2.1, 0.1)	beampipe
$ee$ , 2018D	(198, -34)	B	(-1.9, 0.5, 2.7)	beampipe
$\mu\mu$ , 2016G	(407, -8)	B	(-1.4, 4.0, 6.3)	pixel L1
$\mu\mu$ , 2016G	(-17, -2215)	C	(-2.6, 3.1, 6.6)	pixel L1
$\mu\mu$ , 2016H	(2, 0)	A	(-1.6, -3.5, 12)	inner shield
$\mu\mu$ , 2017F	(522, -13)	B	(-1.1, -3.0, -7.5)	pixel L1

### 1343 Cosmic-ray muons

1344 To estimate the SR contribution of cosmic-ray muons, we perform a study in which  
 1345 we invert the  $\Delta t$  and  $\cos \alpha$  criteria in the  $\mu\mu$  preselection and check how many events  
 1346 are in the SRs. We find three data events with the criteria inverted (one event per year,  
 1347 all in SR IV). Next, we use NoBPTX data, which is dominated by cosmic-ray muon  
 1348 events, to estimate the efficiency for cosmic-ray muons to pass the  $\Delta t$  and  $\cos(\alpha)$   
 1349 criteria after passing the rest of the  $\mu\mu$  preselection criteria. While 3736 NoBPTX  
 1350 data events pass the preselection criteria with the  $\Delta t$  and  $\cos(\alpha)$  criteria removed,  
 1351 zero NoBPTX data events pass the full preselection. To conservatively estimate the

Table 3.18: Background estimates in data while applying the 2018  $\mu\mu$  preselection and the additional requirement of at least one  $b$ -tagged jet. The estimates with at least one  $b$ -tagged jet are about an order of magnitude below the nominal prediction.

	SR I	SR II	SR III	SR IV
Preselection (corrected)	$2.6 \pm 1.0$	$0.09^{+0.12}_{-0.09}$	$0.05^{+0.07}_{-0.05}$	$0.007^{+0.010}_{-0.007}$
Preselection + 1 $b$ jet	$0.19 \pm 0.03$	$0.008^{+0.007}_{-0.004}$	$0.005^{+0.004}_{-0.002}$	$0.0002^{+0.0002}_{-0.0001}$

efficiency, we fluctuate the number of passing events up to 1 and find an efficiency of  $1/3736$ . We therefore find the approximate upper bound on the SR contribution of cosmic-ray muons to be  $3 \times \frac{1}{3736} = 0.0008$ , which is negligible compared to the background estimation in each SR.

### Heavy-flavor mesons

We perform two studies to estimate an upper limit on the SR contribution of leptons from heavy-flavor mesons. First, we estimate SR yields with a simple ABCD method in 2018  $\mu\mu$  preselection data while additionally requiring at least one medium CSVv2  $b$ -tagged jet [76]. The test is performed in the  $\mu\mu$  channel because it contains the smallest relative SR contribution from mismeasurements and should therefore be most sensitive to heavy flavor. As shown in Table 3.18, the background estimates are about an order of magnitude smaller than when no  $b$ -tagged jet is required in our usual preselection.

Next, we look at 2018 data and simulated QCD multijet events that pass the  $\mu\mu$  preselection with the isolation criterion inverted. These samples are dominated by muons from B meson decays, and the QCD simulation describes the data well in the region outside of the Z boson peak, as shown in Fig. 3.26. We use this QCD multijet

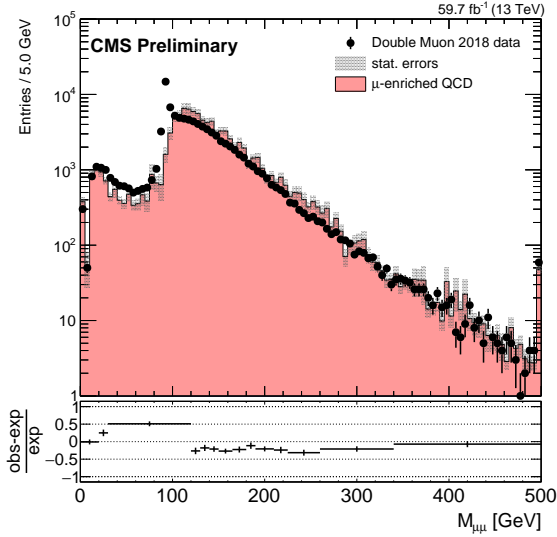


Figure 3.26: The di-muon invariant mass distribution in data and QCD multijet simulation events that pass the 2018  $\mu\mu$  preselection with the muon isolation criterion inverted.

1369 sample to test the heavy-flavor background in two ways. First, we perform a simple  
 1370 ABCD estimate in the simulated QCD multijet events to check for  $|d_0^a|-|d_0^b|$  correlation.  
 1371 As shown in Table 3.19, we find no evidence of correlation, which indicates that the  
 1372 background estimation already accounts for the heavy-flavor background. Second,  
 1373 we estimate the approximate heavy-flavor background in the SRs by taking the ratio  
 1374 of SR to prompt control region events in QCD multijet simulation from the anti-  
 1375 isolated region and the normalization from the number of simulated QCD multijet  
 1376 events that pass the  $\mu\mu$  preselection. Using this approach, we estimate that the  
 1377 heavy-flavor background to be  $0.06^{+0.13}_{-0.05}$  events in SR I and  $0.0015^{+0.0034}_{-0.0012}$  events in  
 1378 SR IV, which is small relative to the nominal prediction shown in the first row of  
 1379 Table 3.18.

Table 3.19: A closure test of the ABCD method in 2018 QCD simulation in the  $\mu\mu$  channel with the muon isolation criterion inverted. The estimates from the ABCD method, the actual yields in simulation, and the ratios of the actual to the estimated yields are shown.

Region	Estimated yield	Actual yield	Ratio of actual to estimate
SR I	$9500 \pm 1100$	$11000 \pm 1000$	$1.2 \pm 0.2$
SR II	$1740^{+310}_{-280}$	$2200^{+330}_{-290}$	$1.3 \pm 0.3$
SR III	$1450^{+280}_{-240}$	$1500^{+180}_{-160}$	$1.0 \pm 0.2$
SR IV	$265^{+62}_{-54}$	$268^{+61}_{-50}$	$1.0 \pm 0.3$

1380 We therefore conclude that the heavy-flavor SR contribution is small and already  
1381 accounted for in our background estimates.

1382 **Low-mass SM hadrons**

1383 To estimate an upper limit on the SR contribution of leptons from decays of low-  
1384 mass SM hadrons, we examine 2018 data and QCD multijet simulation in the  $\mu\mu$   
1385 channel with both the muon isolation and the  $\Delta R$  requirements inverted. As shown  
1386 in Fig. 3.27, this region is dominated low-mass  $\mu\mu$  pairs, with clear  $J/\psi$ ,  $\psi'$ , and  $\Upsilon$   
1387 mass peaks. Many of these leptons are displaced, especially those in the  $J/\psi$  mass  
1388 range. To estimate the fraction of such leptons that will be displaced, we take the  
1389 ratio of SR to prompt control region events of SM hadrons that decay to leptons from  
1390 data in this region.

1391 Even though the inverted-isolation region is dominated by low-mass muon pairs,  
1392 the only QCD multijet simulation event that survives the 2018  $\mu\mu$  preselection has  
1393 a di-muon invariant mass of approximately 300 GeV. Furthermore, the muons are

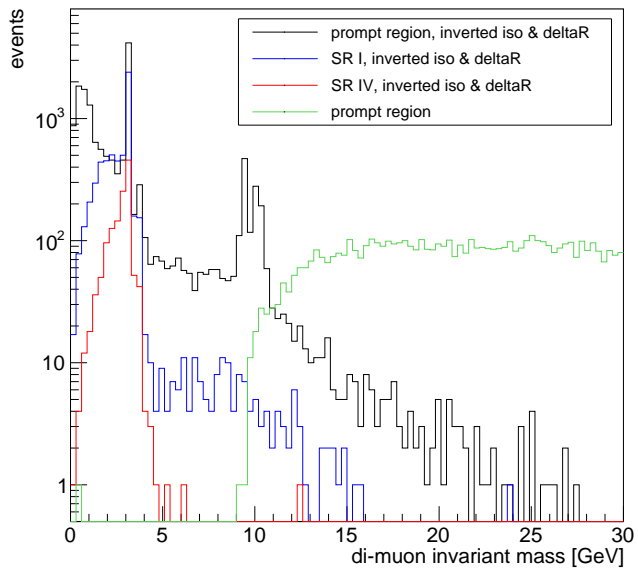


Figure 3.27: The di-muon invariant mass distribution in data events that pass the 2018  $\mu\mu$  prompt control region (black), SR I (blue), and SR IV (red) criteria with the muon isolation and di-muon  $\Delta R$  criteria inverted. The equivalent distribution in the prompt control region is also shown in green.

1394 not near each other in the  $\eta$ - $\phi$  plane ( $\Delta R \approx 3$ ), which is inconsistent with the low-  
1395 mass SM hadron events that dominate the region with the inverted isolation and  $\Delta R$   
1396 criteria. To find a normalization from which to estimate the low-mass SM hadron  
1397 SR contribution, we therefore turn to the inverted-isolation sample used above in the  
1398 heavy-flavor meson cross check. In this sample, the ratio of events with  $\Delta R < 0.5$   
1399 to events with  $2.8 < \Delta R < 3.2$  is about 0.1. We find 0.2 QCD multijet simulated  
1400 events that pass the nominal preselection, and so we estimate that of the events  
1401 passing the 2018  $\mu\mu$  preselection, about 0.02 contain pairs of muons produced in low-  
1402 mass SM hadron decays. We estimate the SR contributions using this preselection  
1403 normalization and the ratio of SR to prompt control region events from the sample  
1404 of SM hadrons that decay to leptons in data. We find this contribution is less than  
1405  $0.006^{+0.013}_{-0.005}$  events in SR I and less than  $0.001^{+0.002}_{-0.001}$  events in SR IV, which, if compared  
1406 with the nominal prediction shown in the first row of Table 3.26, are respectively  
1407 negligible and easily covered by the 140 % systematic uncertainty already applied to  
1408 the background prediction in this region.

1409 **3.6 Systematic uncertainties**

1410 Several systematic uncertainties are applied to the simulated signal efficiency to  
1411 account for uncertainty in the signal yields arising from possible mismodeling of the  
1412 detector conditions and response. The following subsections describe each systematic  
1413 uncertainties in turn, and Table 3.20 summarizes all systematic uncertainties applied  
1414 to the simulated signal.

1415 **3.6.1 Integrated luminosity**

1416 The integrated luminosities of the 2016, 2017, and 2018 data-taking periods are  
1417 individually known with uncertainties in the 2.3–2.5 % range [77, 78, 79], while the  
1418 total Run 2 (2016–2018) integrated luminosity has an uncertainty of 1.8 %, the im-  
1419 provement in precision reflecting the uncorrelated time evolution of some systematic  
1420 effects.

1421 **3.6.2 Pileup**

1422 The simulation of pileup events assumes a total inelastic proton-proton cross sec-  
1423 tion of 69.2 mb with an associated uncertainty of 5 % [80]. The systematic uncertainty  
1424 arising as a result of the modeling of pileup events is estimated by varying the cross  
1425 section of the minimum bias events by 5 % when generating the target pileup distri-  
1426 butions. The pileup weights are recomputed with these new distributions and applied  
1427 to the simulated events to obtain the variation in the yields in the inclusive signal  
1428 region. The average uncertainty is between 1 and 2 %. We treat these uncertainties  
1429 as 100 % correlated across the three years of data taking.

Table 3.20: Systematic uncertainties in the signal efficiency for all three years and the three channels. The mean is provided in cases where the uncertainty varies by signal sample. Uncertainties in the same row are treated as correlated among the years of data taking, except for the displaced tracking and muon pixel hit efficiencies, where the 2016 uncertainty is treated as uncorrelated with the 2017 and 2018 uncertainties.

Systematic uncertainty	2016	2017	2018
<i>Integrated luminosity</i>	1.8%	1.8%	1.8%
<i>Pileup</i>			
- $e\mu$ channel	0.5%	0.6%	0.5%
- $ee$ channel	0.5%	0.9%	0.8%
- $\mu\mu$ channel	0.2%	0.1%	0.2%
<i>Displaced tracking efficiency</i>	14%	5.8%	2.4%
<i>Trigger efficiency</i>			
- $e\mu$ channel, electrons	1.6%	1.3%	1.2%
- $e\mu$ channel, muons	1.6%	1.4%	1.2%
- $ee$ channel	10%	13%	19%
- $\mu\mu$ channel	1.2%	1.0%	1.1%
<i>Muon trigger efficiency at large <math> d_0 </math></i>			
- $e\mu$ channel, muons	20%	20%	20%
- $\mu\mu$ channel	20%	20%	20%
<i>Lepton identification and isolation</i>			
- $e\mu$ channel, electrons	1.2%	3.6%	3.5%
- $e\mu$ channel, muons	0.05%	0.07%	0.06%
- $ee$ channel	2.4%	7.2%	7.0%
- $\mu\mu$ channel	0.10%	0.14%	0.12%
<i>Muon pixel hit efficiency</i>			
- $e\mu$ channel, muons	32%	12%	16%
- $\mu\mu$ channel	73%	23%	30%
<i>Lepton <math> d_0 </math> correction</i>			
- $e\mu$ channel, electrons	—	0.001%	0.001%
- $e\mu$ channel, muons	—	0.003%	0.001%
- $ee$ channel	—	0.11%	0.11%
- $\mu\mu$ channel	—	0.11%	0.11%

1430 **3.6.3 Displaced tracking efficiency**

1431 The systematic uncertainty associated with the modeling of the displaced tracking  
1432 efficiency is derived from a dedicated study using cosmic-ray muons. Following the  
1433 results of the study presented in Appendix C, we assign 14.1%, 5.8%, and 2.4%  
1434 systematic uncertainties in 2016, 2017, and 2018, respectively. Because the CMS pixel  
1435 detector was upgraded between 2016 and 2017 data taking, we treat the 2017 and  
1436 2018 systematic uncertainties as fully correlated and the 2016 systematic uncertainty  
1437 as uncorrelated with 2017 and 2018.

1438 **3.6.4 Trigger efficiency**

1439 The trigger efficiency systematic uncertainty is given by the uncertainty in the  
1440 measured trigger efficiency scale factors (see Section 3.4.4). These uncertainties are  
1441 1% or less for the  $e\mu$  and  $\mu\mu$  channels and about 10% for the  $ee$  channel. In addition,  
1442 we have studied the trigger efficiency in signal as a function of  $|d_0|$  for events in the  
1443 trigger  $p_T$  plateau. To cover the change observed in the muon trigger efficiency over  
1444 the full  $|d_0|$  range, we assign an additional 20% uncertainty.

1445 We treat the trigger efficiency uncertainties as 100% correlated across the three  
1446 years of data taking.

1447 **3.6.5 Lepton ID and isolation**

1448 To find the systematic uncertainty associated with the corrections to the lepton  
1449 ID and isolation, we fluctuate the lepton scale factors up and down by their uncer-  
1450 tainty and observe the change in the event yields in the inclusive signal region. The  
1451 average uncertainty for electrons is about 3% in the  $e\mu$  channel and about 7% in

1452 the  $ee$  channel, while the average uncertainty for muons is  $< 1\%$ . We treat these  
1453 uncertainties as 100 % correlated across the three years of data taking.

1454 **3.6.6 Muon pixel hit efficiency**

1455 The requirement in the muon ID that muons have at least one pixel hit could in  
1456 principle have some appreciable  $|d_0|$  dependence, so we perform a dedicated study  
1457 to ensure that we account for any differences in  $|d_0|$  dependence between data and  
1458 simulation. Figure 3.28 shows the efficiency of this requirement in cosmic simulation  
1459 and NoBPTX data (described in appendix C) as a function of muon  $|d_0|$ . For events  
1460 in the denominator of these plots, we require that at least 2 global, PF muons have  
1461  $|\eta| < 1.0$ ,  $p_T > 25 \text{ GeV}$ , no displaced vertices in the tracker material,  $|d_z| < 15 \text{ cm}$ ,  
1462 and pass all the tight ID criteria except the pixel hit requirement. We also require  
1463 the muons to be separated by  $\Delta R > 0.2$ . The events in the numerator must pass the  
1464 same requirements in addition to the requirement that the muons have at least one  
1465 pixel hit. From this plot, we calculate the mean efficiency to identify the muons in the  
1466 simulated signal events using the same procedure as is used for the displaced tracking  
1467 efficiency systematic uncertainty described in Appendix C. We repeat the procedure  
1468 in both cosmic simulation and in NoBPTX data, and using the ratio of these two  
1469 efficiencies, we derive the relative systematic uncertainty in the signal. The average  
1470 uncertainty is about 16 % (32 %) in the  $e\mu$  ( $\mu\mu$ ) channel. As the pixel detector was  
1471 upgraded after 2016, the 2017 and 2018 systematic uncertainties are treated as fully  
1472 correlated while the 2016 uncertainty is treated as uncorrelated with the 2017 and  
1473 2018 uncertainties.

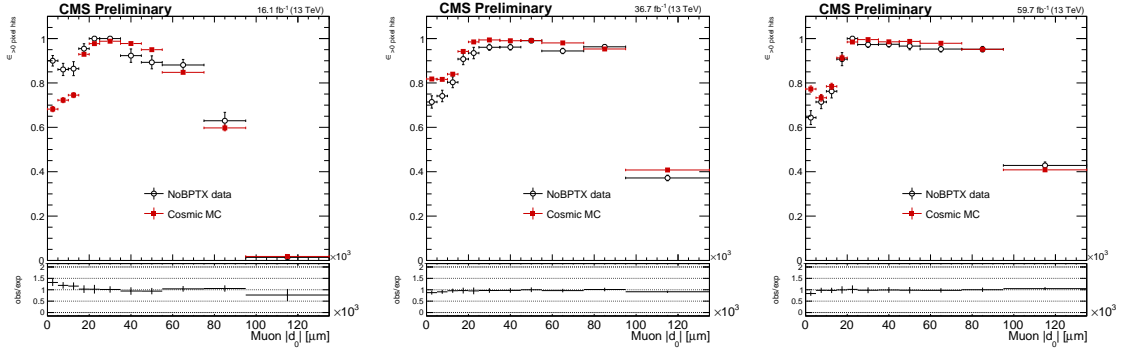


Figure 3.28: The pixel hit efficiency as a function of muon  $|d_0|$  in simulated cosmic ray events and NoBPTX data in 2016 (left), 2017 (center), and 2018 (right) conditions.

### 1474 3.6.7 Lepton $d_0$ resolution

1475 To find the systematic uncertainty associated with the corrections to the lepton  
 1476  $d_0$  (see Section 3.4.3), we fluctuate the lepton  $d_0$  corrections up and down by their  
 1477 uncertainty and observe the change in the event yields in the inclusive signal region.  
 1478 The average uncertainty is  $< 1\%$ . We treat these uncertainties as 100 % correlated  
 1479 in 2017 and 2018. No  $d_0$  correction or systematic uncertainty is needed for 2016  
 1480 simulation.

1481 **3.7 Results**

1482 After unblinding and comparing the observed SR yields with the predicted back-  
1483 ground yields, we find no significant excess. Table 3.21 shows the predicted number  
1484 of background events and the observed yields in each SR, and Figs. 3.29 and 3.30  
1485 visually summarize this same information.

1486 **3.7.1 Observed events**

1487 In general, the observed SR events appear to be SM events from proton-proton  
1488 collisions. Specifically, we see no evidence of leptons from cosmic rays, material inter-  
1489 actions, or signal. Figure 3.31 shows two-dimensional  $|d_0|$  distributions of data events  
1490 that pass the preselection, and Fig. 3.32 shows the same but for data events in the  
1491 inclusive SR. As expected for SM background, the observed events are concentrated  
1492 in the low  $|d_0|$  region.

1493 We also use event display visualizations to examine each observed SR event indi-  
1494 vidually and record our observations below.

1495 In the  $e\mu$  channel, the SR events tend to have several jets and often have  $p_T^{\text{miss}} >$   
1496 100 GeV. Many events have muon  $\phi$  values such that the muon system hits are all  
1497 near the edges of detector sections or muon  $\eta$  values such that the muon is near the  
1498 barrel/endcap transition in the muon system. There are also a few events in which  
1499 the electron and/or muon are associated with a different primary vertex than their  
1500 associated track.

1501 In the  $ee$  channel, the majority of SR events contain at least one electron with  
1502  $|\eta| > 1.1$ , which increases the probability that their  $d_0$  is poorly measured. Across all  
1503 three years, most events fall into one of three categories:

Table 3.21: The number of estimated background and observed events in each channel and SR. For each estimate, the total uncertainty is given. The  $p_T$  boundaries that separate the low- and high- $p_T$  bins of SR I are listed in Table 3.11.

	SR I, low- $p_T$ bin	SR I, high- $p_T$ bin	SR II	SR III	SR IV
<i>2016 e<math>\mu</math></i>					
- estimated	$3.8^{+4.8}_{-3.8}$	$0.41^{+0.53}_{-0.41}$	$0.09^{+0.12}_{-0.09}$	$0.15 \pm 0.15$	$0.003^{+0.004}_{-0.003}$
- observed	8	1	0	0	0
<i>2017+2018 e<math>\mu</math></i>					
- estimated	$38 \pm 13$	$0.75^{+0.41}_{-0.34}$	$0.23^{+0.27}_{-0.23}$	$0.71^{+0.76}_{-0.71}$	$0.01^{+0.02}_{-0.01}$
- observed	28	3	0	1	0
<i>2016 ee</i>					
- estimated	$18 \pm 11$	$0.22^{+0.17}_{-0.16}$	$0.51^{+1.02}_{-0.51}$	$0.43^{+0.85}_{-0.43}$	$0.01^{+0.02}_{-0.01}$
- observed	40	0	0	1	0
<i>2017+2018 ee</i>					
- estimated	$62^{+18}_{-17}$	$0.85^{+0.33}_{-0.35}$	$2.8 \pm 1.1$	$3.6 \pm 1.4$	$0.24^{+0.10}_{-0.09}$
- observed	48	0	1	4	0
<i>2016 <math>\mu\mu</math></i>					
- estimated	$7.4 \pm 3.0$	$0.25 \pm 0.11$	$0.17 \pm 0.11$	$0.19 \pm 0.12$	$0.01 \pm 0.01$
- observed	15	0	0	1	0
<i>2017+2018 <math>\mu\mu</math></i>					
- estimated	$3.5 \pm 1.5$	$0.69 \pm 0.31$	$0.08^{+0.12}_{-0.08}$	$0.14^{+0.19}_{-0.14}$	$0.01^{+0.02}_{-0.01}$
- observed	1	1	1	1	0

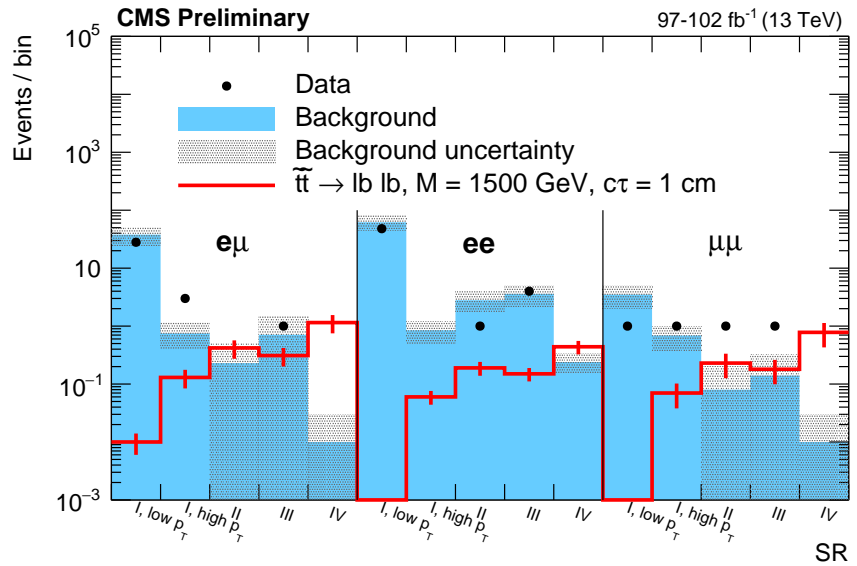
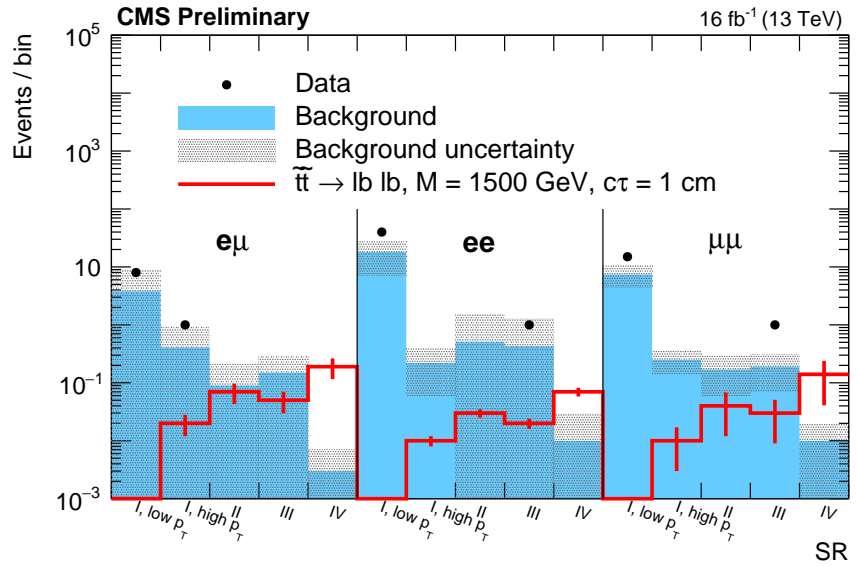


Figure 3.29: The number of estimated background and observed events in each channel and SR, with a representative signal overlaid, for 2016 (top) and 2017–2018 (bottom). For each background estimate and signal yield, the total uncertainty is given.

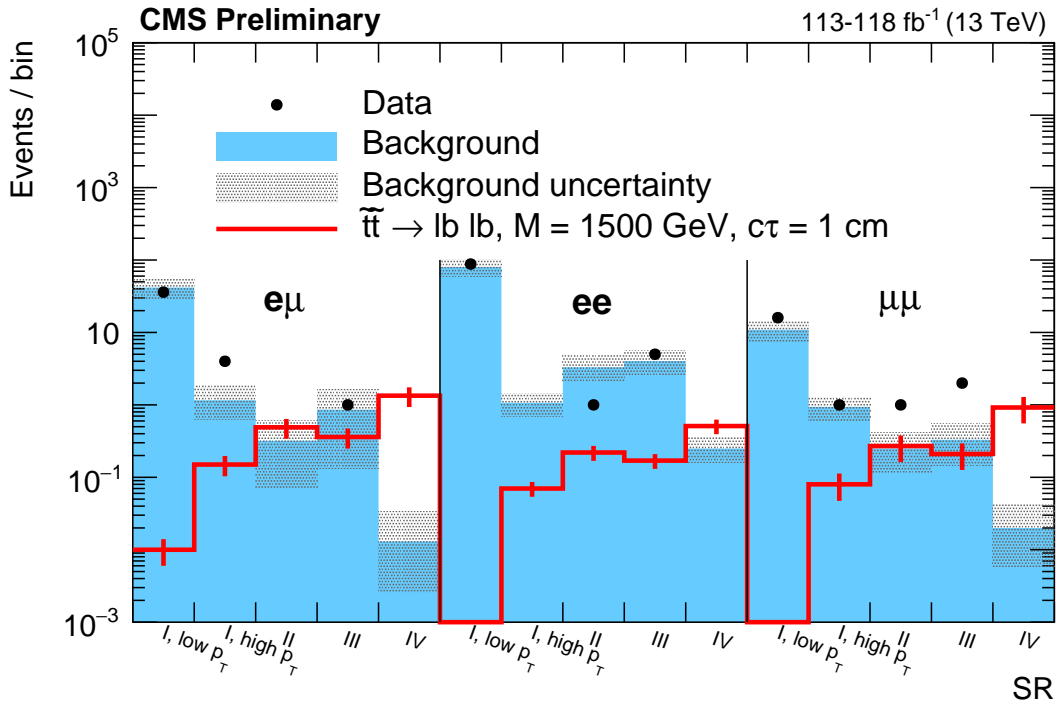


Figure 3.30: The number of estimated background and observed events in each channel and SR, with a representative signal overlaid, for 2016–2018. For each background estimate and signal yield, the total uncertainty is given.

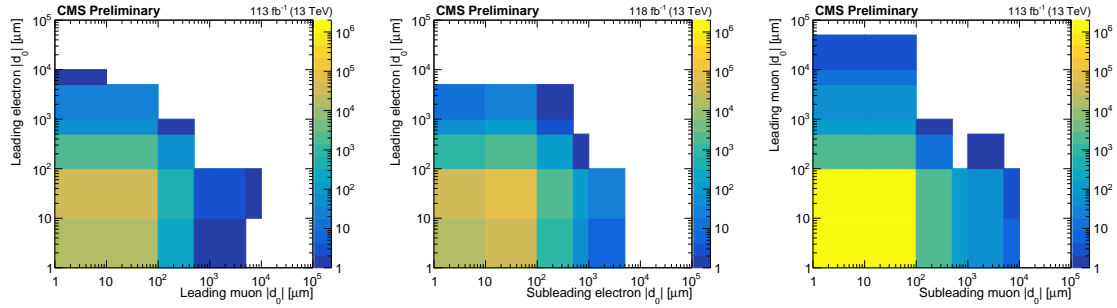


Figure 3.31: Two-dimensional distributions of  $|d_0^a|$  and  $|d_0^b|$ , for the events in data that pass the  $e\mu$  (left),  $ee$  (center), and  $\mu\mu$  (right) preselection. The bins along the x and y axes contain underflow. The inclusive signal region covers the region between  $100 \mu\text{m}$  and  $10 \text{ cm}$  in each  $|d_0|$  variable shown.

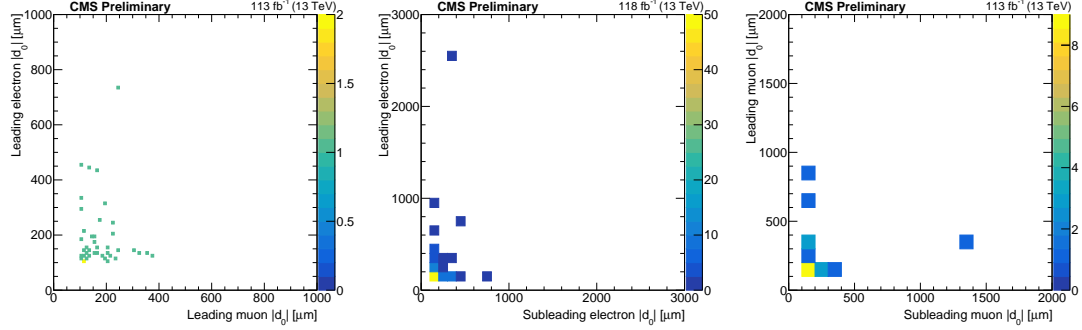


Figure 3.32: Two-dimensional distributions of  $|d_0^a|$  and  $|d_0^b|$ , for data events in the inclusive SR in the  $e\mu$  (left),  $ee$  (center), and  $\mu\mu$  (right) channels.

- 1504     1. Events with two electrons that appear to be from a boosted Z boson with an
- 1505         invariant mass between 80 and 100 GeV, opposite one or two jets
- 1506     2. Events with two electrons approximately back-to-back in  $\phi$  with an invariant
- 1507         mass greater than 100 GeV and  $p_T^{\text{miss}}$  usually between 10 and 40 GeV
- 1508     3. Events that are similar to type 2 but with at least one jet and frequently  $p_T^{\text{miss}}$
- 1509         between 70 and 110 GeV
  
- 1510         In the  $\mu\mu$  channel, many events have an invariant mass consistent with the mass
- 1511         of the Z boson and  $p_T^{\text{miss}}$  less than about 60 GeV. Most of the events found in 2017
- 1512         and 2018 have an invariant mass higher than than the Z boson mass and could be  $t\bar{t}$
- 1513         events. Eight of the sixteen SR events in 2016 have two muons with  $\phi$  values of about
- 1514          $\pm\pi/2$  (i.e. in the  $y$ - $z$  plane). Every muon pair in these eight events have an invariant
- 1515         mass consistent with a Z boson, and the  $\cos(\alpha)$  and  $\Delta t$  distributions of these muons
- 1516         confirm that they are not from cosmic rays. As shown in Fig. 3.33, these features are
- 1517         clearly visible in the  $\phi$  and di-muon invariant mass distributions of the SR data when
- 1518         compared with background simulation. Thirteen of the sixteen muons in these eight

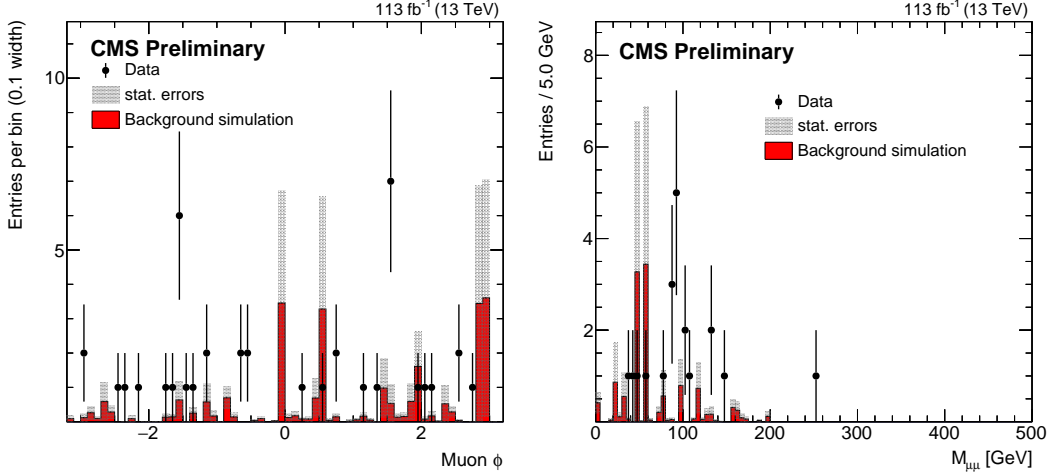


Figure 3.33: Muon  $\phi$  and di-muon invariant mass distributions for data and composite background simulation in the  $\mu\mu$  channel in the inclusive SR. The background simulation is normalized to the ABCD method background prediction.

1519 events have only one valid pixel hit, and event displays of these events show that the  
 1520 muon track often passes between or at the edge of pixel modules near the place where  
 1521 the two halves of the original pixel detector barrel are joined. We believe that this  
 1522 feature causes the muon  $d_0$  values to be poorly measured.

### 1523 3.7.2 Limits

1524 The data show no significant excess over background, so we set upper limits on the  
 1525 product of the signal production cross section ( $\sigma$ ) and branching fraction ( $\mathcal{B}$ ) using  
 1526 the HybridNew statistical method of the “Combine” tool developed by the CMS  
 1527 Higgs working group [81, 82, 83, 84]. The ABCD estimate is performed in Combine,  
 1528 which means that any signal contamination in the control regions is accounted for  
 1529 automatically. We perform a simultaneous counting experiment in each signal region

1530 bin. Figure 3.34 shows the 95% confidence level (CL) upper limits on the top squark  
1531 mass as a function of its lifetime.

1532 The variation in the size and shape of the exclusion regions between the three  
1533 channels is mostly explained by variation in signal yields between the three channels.  
1534 Looking at the high- $p_T$  bin of SR I, which is the most sensitive bin for top squarks with  
1535 large masses and small lifetimes, we find that the simulated signal yield is highest  
1536 in the  $e\mu$ . This difference between the  $e\mu$  and same-flavor channels is a result of  
1537 simple combinatorics: the two independent top squark decays will result in an  $e\mu$  final  
1538 state twice as often as an  $ee$  or  $\mu\mu$  final state. In this bin, the  $ee$ - and  $\mu\mu$ -channel  
1539 signal yields are similar. SR IV drives the sensitivity for top squarks with large  
1540 lifetimes. Because CMS identifies muons with higher efficiency than it does electrons,  
1541 the  $\mu\mu$  channel has the largest simulated signal yield in SR IV when considering top  
1542 squarks with lifetimes  $\gtrsim 10$  cm. For this same reason, the  $ee$  channel has the smallest  
1543 signal yield out of the three channels in SR IV when considering top squark lifetimes  
1544  $\gtrsim 10$  cm. Taking all of these effects together, we find that the  $e\mu$  channel is the most  
1545 sensitive for lifetimes  $\lesssim 10$  cm while the  $\mu\mu$  channel is the most sensitive for lifetimes  
1546  $\gtrsim 10$  cm.

1547 Figure 3.35 shows the 95% CL upper limits for the combination of the three  
1548 channels. The top squark limits assume  $\mathcal{B}(\tilde{t} \rightarrow bl) = \mathcal{B}(\tilde{t} \rightarrow dl) = 100\%$ , and each  $l$   
1549 has an equal probability of being an electron, a muon, or a tau lepton.

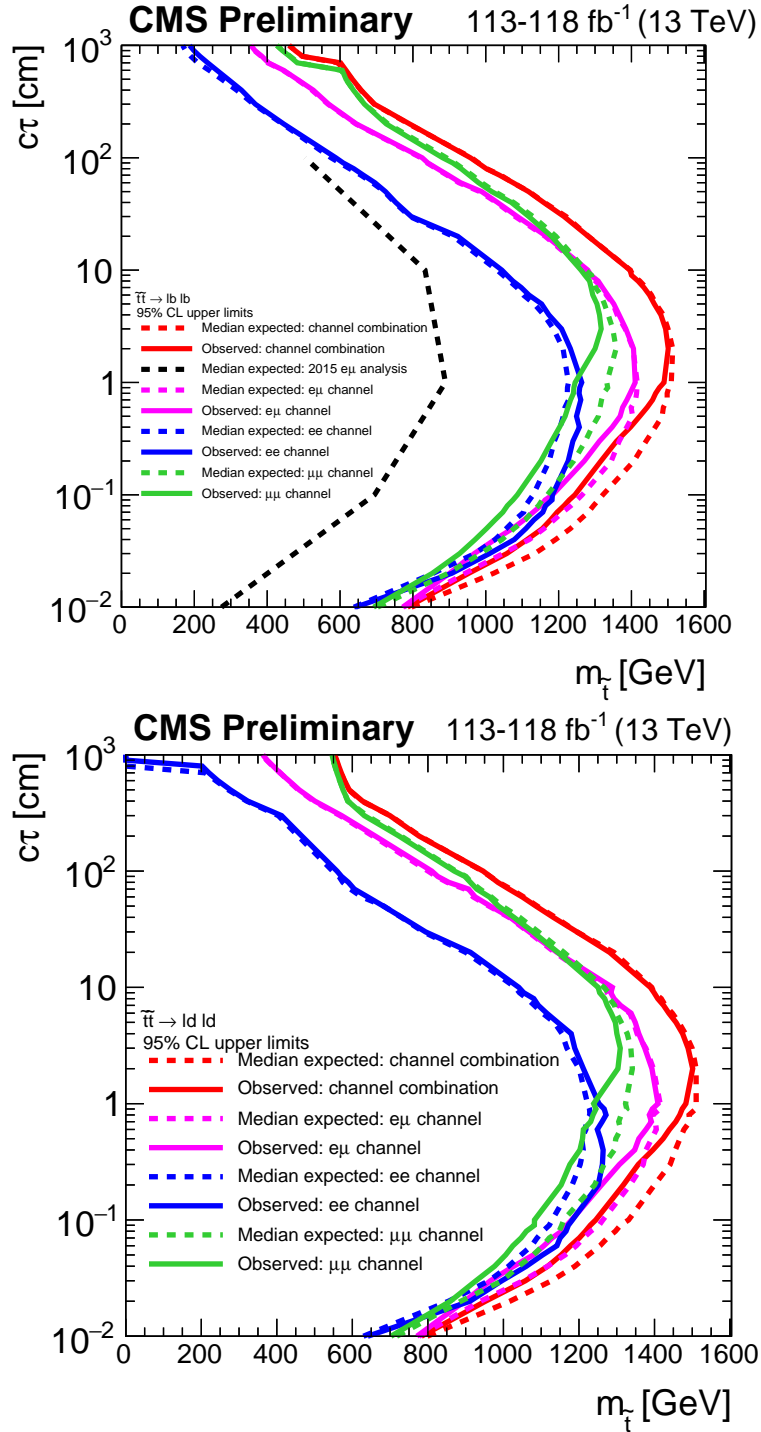


Figure 3.34: The 95% CL upper limits on the top squark mass ( $m_{\tilde{t}}$ ) as a function of its lifetime ( $c\tau$ ), for the  $e\mu$ ,  $ee$ , and  $\mu\mu$  channels. The  $\tilde{t}\tilde{t} \rightarrow \bar{l}b \bar{l}b$  (top) and  $\tilde{t}\tilde{t} \rightarrow \bar{l}d \bar{l}d$  (bottom) processes are shown.

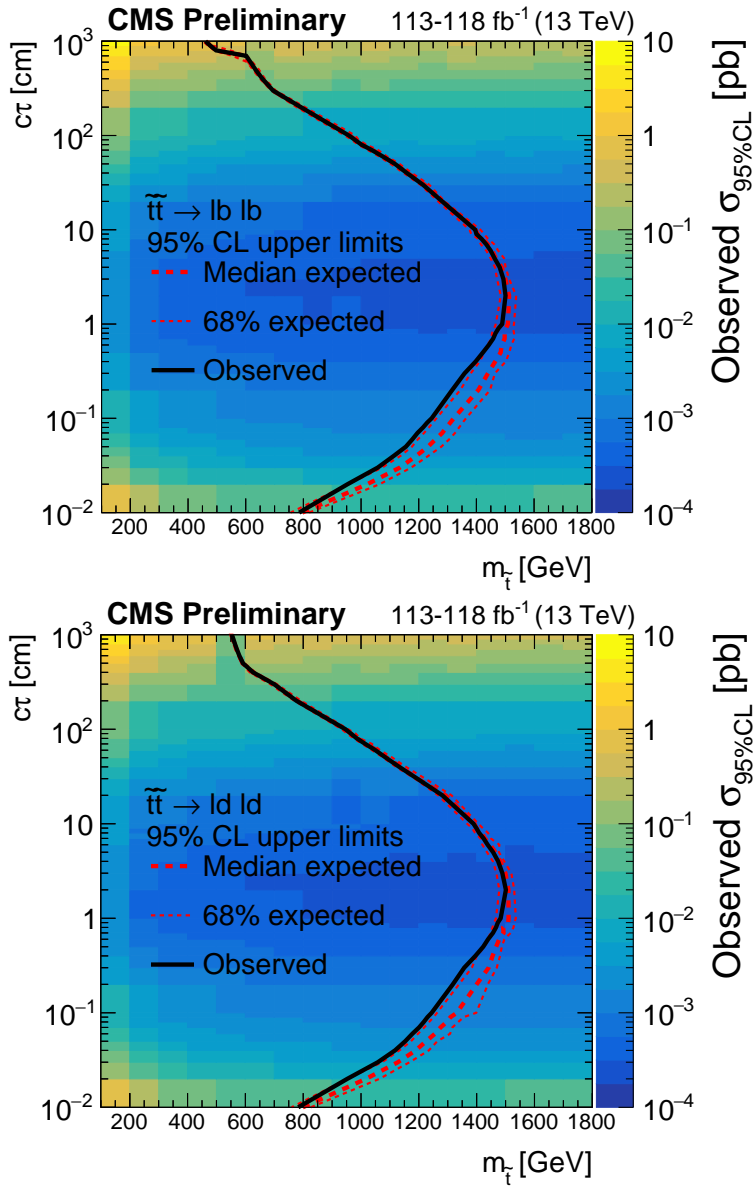


Figure 3.35: The 95% CL upper limits on the top squark mass ( $m_{\tilde{t}}$ ) as a function of its lifetime ( $c\tau$ ). The colors indicate the observed 95% CL upper limit on the cross section. The  $\tilde{t}\bar{t} \rightarrow l\bar{b} l\bar{b}$  (left) and  $\tilde{t}\bar{t} \rightarrow l\bar{d} l\bar{d}$  (right) processes are shown.

1550    **3.7.3 Additional likelihood tests**

1551    We also perform several statistical tests to help assess the significance of the  
1552    differences between the observed and predicted SR yields and to ensure that the  
1553    likelihood is handling the observed yields in a reasonable way.

1554    We first compare the best-fit background yields under the background-only hy-  
1555    pothesis while masking the signal regions with the best-fit background yields under  
1556    the signal+background hypothesis using the full information from all signal and con-  
1557    trol regions. For simplicity, we refer to the first quantity as the pre-fit prediction and  
1558    the second as the post-fit prediction. Table 3.22 lists the pre- and post-fit predictions  
1559    for each channel and SR, and Fig. 3.36 (left) shows associated pull distribution. We  
1560    find that the differences between the pre- and post-fit predictions are consistent with  
1561    the variation one would expect from purely statistical effects.

1562    Next, we examine the equivalent pull distribution for background yield nuisance  
1563    parameters. Figure 3.36 (right) shows that the differences in nuisance parameter  
1564    values before and after the fit are also consistent with the variation one would expect  
1565    from purely statistical effects.

1566    Finally, we check the observed asymptotic significance of the  $\tilde{t}\bar{t} \rightarrow \bar{l}b\bar{l}\bar{b}$  signal  
1567    model. As shown in Fig. 3.37, the observed significance is less than two for all signal  
1568    points we consider when looking at the combination of all channels as well as each  
1569    channel individually. We therefore conclude that the observed yields do not constitute  
1570    a significant excess.

Table 3.22: The pre- and post-fit predictions for each signal region bin.

	SR I, low- $p_T$ bin	SR I, high- $p_T$ bin	SR II	SR III	SR IV
<i>2016 e<math>\mu</math></i>					
- pre-fit	$3.8 \pm 3.9$	$0.40 \pm 0.45$	$0.09 \pm 0.11$	$0.15 \pm 0.13$	$0.003 \pm 0.003$
- post-fit	$7.1 \pm 2.0$	$0.76 \pm 0.31$	$0.08 \pm 0.08$	$0.14 \pm 0.14$	$0.003 \pm 0.003$
<i>2017+2018 e<math>\mu</math></i>					
- pre-fit	$38 \pm 14$	$0.75 \pm 0.40$	$0.23 \pm 0.37$	$0.71 \pm 0.90$	$0.01 \pm 0.02$
- post-fit	$31 \pm 5$	$0.68 \pm 0.25$	$0.20 \pm 0.17$	$0.65 \pm 0.48$	$0.01 \pm 0.01$
<i>2016 ee</i>					
- pre-fit	$18 \pm 11$	$0.22 \pm 0.17$	$0.51 \pm 2.41$	$0.43 \pm 2.06$	$0.01 \pm 0.06$
- post-fit	$35 \pm 5$	$0.40 \pm 0.14$	$0.50 \pm 0.75$	$0.44 \pm 0.53$	$0.01 \pm 0.02$
<i>2017+2018 ee</i>					
- pre-fit	$62 \pm 17$	$0.85 \pm 0.31$	$2.8 \pm 0.9$	$3.6 \pm 1.2$	$0.25 \pm 0.09$
- post-fit	$50 \pm 6$	$0.65 \pm 0.19$	$2.5 \pm 0.7$	$3.2 \pm 0.9$	$0.22 \pm 0.06$
<i>2016 <math>\mu\mu</math></i>					
- pre-fit	$7.4 \pm 3.3$	$0.25 \pm 0.11$	$0.17 \pm 0.11$	$0.19 \pm 0.12$	$0.01 \pm 0.01$
- post-fit	$11 \pm 2$	$0.37 \pm 0.10$	$0.19 \pm 0.10$	$0.21 \pm 0.12$	$0.01 \pm 0.01$
<i>2017+2018 <math>\mu\mu</math></i>					
- pre-fit	$3.4 \pm 1.6$	$0.69 \pm 0.32$	$0.08 \pm 0.12$	$0.14 \pm 0.18$	$0.01 \pm 0.02$
- post-fit	$2.5 \pm 1.1$	$0.51 \pm 0.22$	$0.14 \pm 0.36$	$0.23 \pm 0.63$	$0.02 \pm 0.05$

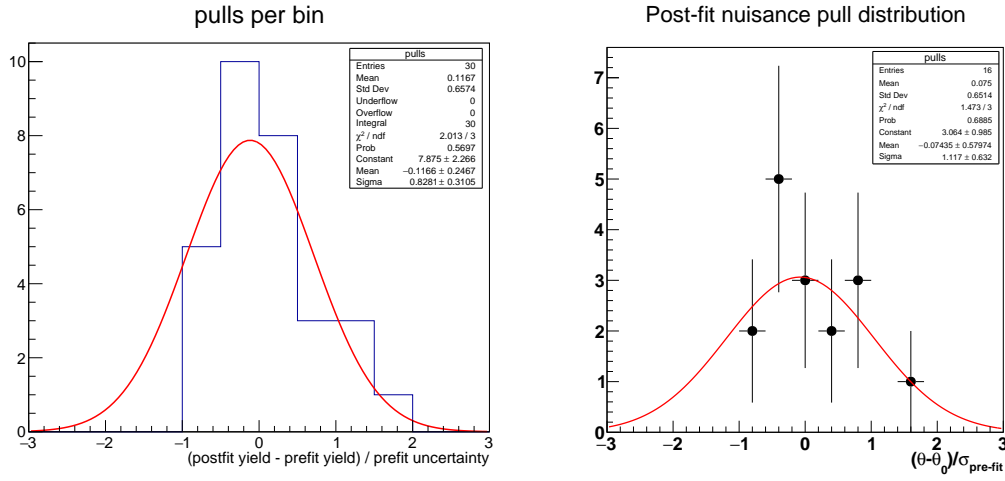


Figure 3.36: The distribution of pulls for each signal region bin, where pulls are calculated as the difference between the post-fit background yield and the pre-fit background yield divided by the pre-fit background uncertainty (left). The distribution of pulls for each background nuisance parameter, where pulls are calculated as the difference between the post-fit value and the pre-fit value divided by the pre-fit uncertainty (right).

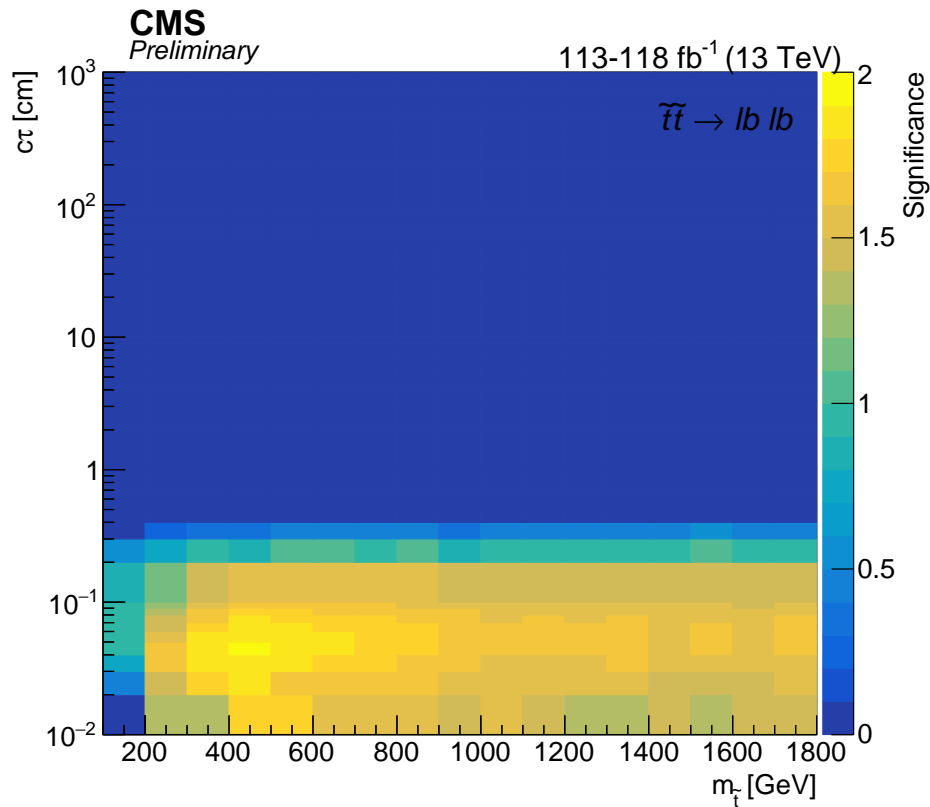


Figure 3.37: The observed asymptotic significances for the  $\tilde{t}\tilde{t} \rightarrow \bar{l}b\bar{l}b$  process as a function of  $\tilde{t}$  mass and lifetime using the combined results.

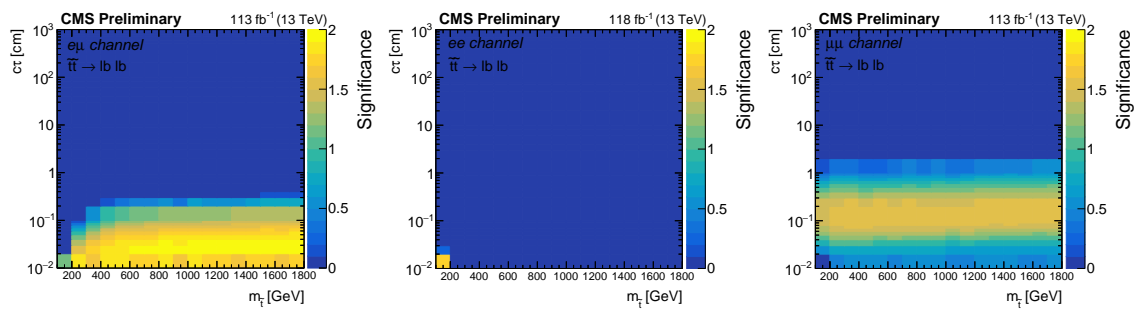


Figure 3.38: The observed asymptotic significances for the  $\tilde{t}\tilde{t} \rightarrow \bar{l}b\bar{l}b$  process as a function of  $\tilde{t}$  mass and lifetime in the  $ee$  (left),  $e\mu$  (center),  $\mu\mu$  channels (right).

## Chapter 4: Conclusion

1572 A search has been presented for new long-lived particles that propagate a mea-  
1573 surable distance before decaying to leptons inside the CMS detector. The resulting  
1574 displaced lepton signature is targeted by selecting events with two leptons (an electron  
1575 and a muon, two electrons, or two muons) whose transverse impact parameters are  
1576 between 0.01 and 10 cm. The search is performed in  $113\text{--}118 \text{ fb}^{-1}$  of proton-proton  
1577 collision data produced by the CERN LHC at a center-of-mass energy of 13 TeV and  
1578 collected by the CMS detector in 2016, 2017, and 2018. This analysis is the first  
1579 at CMS to target pairs of displaced electrons or muons without requiring that they  
1580 form a common vertex. The observation is consistent with the background-only hy-  
1581 pothesis, and limits are set on the product of the cross section of top squark pair  
1582 production and the branching fraction to a lepton and a  $b$  or  $d$  quark through an  
1583 R-parity-violating vertex. For a proper decay length hypothesis of 2 cm, top squarks  
1584 with masses up 1500 GeV are excluded at the 95 % confidence level.

1585 Looking to the future, there are several opportunities to increase the sensitivity to  
1586 new long-lived particles that decay to leptons. Aside from the incremental improve-  
1587 ments offered by the expected increases in integrated luminosity and center-of-mass  
1588 energy provided by the LHC (14 TeV proton-proton collisions may be available as

1589 soon as 2022 [85, 86]), there are a few changes to the analysis strategy that may be  
1590 worth pursuing.

1591 The most straightforward improvement would be to study the electron and muon  
1592 identification requirements with an eye to improving the signal efficiency, especially  
1593 at large  $|d_0|$ . In particular, the missing inner hit and pixel hit requirements applied  
1594 to electrons and muons, respectively, in the current analysis effectively limit the max-  
1595 imum LLP decay length to the radius of the CMS pixel detector, which is 16 cm.  
1596 Any gains in signal efficiency would of course have to be balanced against the likely  
1597 increase in the mismeasurement background. Thinking along similar lines, it may be  
1598 interesting to investigate the effects of relaxing the lepton isolation requirement.

1599 A more challenging angle would be to explicitly consider tau leptons in the final  
1600 state. The analysis presented here is sensitive to displaced taus that decay leptonically  
1601 to electrons and muons, but a future analysis could likely expand this sensitivity by  
1602 explicitly studying the  $|d_0|$  behavior of displaced taus. Given the tau decay branching  
1603 fractions [33], the largest gain would likely come from considering hadronic tau decays,  
1604 though this route would also likely represent a considerable challenge.

1605 Finally, one could perform an analysis similar to the one presented here but specif-  
1606 ically target new low-mass long-lived particles. The lepton  $p_T$  requirements imposed  
1607 by the trigger limit the low-mass sensitivity of the current analysis. One possible  
1608 approach would be to adopt a different triggering strategy in the next data-taking  
1609 period, but it may be that CMS has already collected the ideal dataset in which to  
1610 perform such a search. In 2018, CMS debuted a novel trigger strategy in which special-  
1611 ized triggers collected approximately ten billion unbiased B-hadron-decay events [87].  
1612 The triggers use a tag-and-probe strategy that actually require the presence of at

1613 least one displaced muon whose  $p_T$  can be as low as 7 GeV. The trade-off is that  
1614 most of the muons will be embedded in  $b$ -tagged jets, which will likely necessitate  
1615 changes to the analysis strategy. Such a search could be an interesting way to cover  
1616 new ground with existing data.

1617 Searches for BSM LLPs are critical to exploring the available new-physics param-  
1618 eter space and ultimately to understanding whether new physics exists at currently  
1619 accessible energy scales. The analysis presented here explicitly constrains the natural  
1620 parameter space of RPV SUSY models, but more importantly, it also constrains any  
1621 not-yet-imagined new physics scenarios that could produce displaced leptons. There  
1622 are still many stones unturned, and the analysis presented in this thesis shines a light  
1623 on one more region of this unexplored space.

## Appendix A: Impact of APV25 saturation on displaced tracking

1626 A portion of the data collected by the CMS detector in 2016 is affected by the APV  
1627 saturation effect described in Ref. [88]. The APV25 saturation effect is a byproduct  
1628 of the production of heavily ionising particles (HIPs) in inelastic interactions between  
1629 hadrons and the nuclei of silicon sensors. The energy deposits of HIPs can be up to  
1630 1000 times greater than those of typical particles produced in LHC collisions. These  
1631 large energy deposits can saturate the analog readout of the APV25 chips [89] that are  
1632 used to read out the CMS silicon strip tracker, which is described in Section 2.2.2. Due  
1633 to a feature of the APV25 powering scheme that normally helps stabilize the pulse-  
1634 height baseline, a single saturated channel can inadvertently suppress the outputs of  
1635 the 127 other APV25 channels for hundreds of nanoseconds.

Only around one in every 1000 incident hadrons will result in saturating HIP events, so the effect is only significant at high instantaneous luminosities. In 2016, the instantaneous luminosity increased to greater than the original LHC design goal, and the effect began influencing detector performance. Starting in run 278802, the tracker front-end electronics were reconfigured to substantially reduce their sensitivity to the APV25 saturation effect.

1642        The deadtime associated with a saturating HIP event can cause some tracker hits  
1643        to be lost. This effect can lead to reduced tracking efficiency, and it is reasonable to  
1644        suspect that the loss of efficiency may be more significant for displaced particles that  
1645        may have fewer tracker hits to begin with. To investigate the impact on displaced  
1646        tracking, one of our collaborators, Ian Tomalin, performed a study with  $K_S^0 \rightarrow \pi^+\pi^-$   
1647        decays. From this study, we conclude that the Displaced Leptons analysis should  
1648        only use data taken after the APV25 saturation effect was mitigated. We therefore  
1649        use only eras G and H in 2016 and all available data in 2017 and 2018.

1650        Using data collected in 2016, 2017, and 2018 with the `HLT_ZeroBias` trigger, the  
1651        reconstructed  $K_S^0$  candidate decay lengths are compared among several different runs  
1652        that correspond to a wide range of instantaneous luminosities and data-taking periods.  
1653        The  $K_S^0$  candidates used come from the `generalV0Candidates:Kshort` collection.  
1654        Each candidate must have a pair of oppositely charged tracks consistent with the  $K_S^0$   
1655        mass and coming from a common vertex that is at least 2 cm from the beam line.  
1656        The tracks are required to have at least one pixel hit and  $|\eta| < 2$ . In 2016 (2017-18),  
1657        the tracks are required to have  $p_T > 0.7$  GeV (1.5 GeV).

1658        Figure A.1 shows the reconstructed transverse decay length of the  $K_S^0$  candidates  
1659        for data from all three years. Each distribution is normalized to the integrated lumi-  
1660        nosity of the run from which it is taken. In the 2016 plot, the solid (dashed) lines  
1661        correspond to runs taken before (after) the APV25 saturation effect was mitigated.  
1662        In the pre-mitigation runs, the  $K_S^0$  transverse decay length distribution falls rapidly  
1663        with increasing instantaneous luminosity, but the dependence on instantaneous lumi-  
1664        nosity is significantly reduced in the post-mitigation runs and in all 2017 and 2018

1665 runs. The narrower transverse decay length at higher luminosity in the 2016 pre-  
1666 mitigation runs is interpreted as an instantaneous-luminosity-dependent decrease in  
1667 tracking efficiency.

1668 Given the size of this effect, we decide not to use 2016 data taken before run  
1669 278802 in the Displaced Leptons analysis. The instantaneous-luminosity-dependent  
1670 displaced tracking efficiency would be difficult to quantify, which would lead to large  
1671 systematic uncertainties. Furthermore, the signal yield would be suppressed by the  
1672 lower displaced tracking efficiency. Finally, studies of displaced tracking efficiency  
1673 with cosmic-ray data are insensitive to the APV25 saturation effect because the in-  
1674 stantaneous luminosity during dedicated cosmic runs is zero.

1675 A small dependence on instantaneous luminosity is also apparent in the 2017  
1676 and 2018 distributions shown in Fig. A.1. The runs with the lowest (highest) in-  
1677 stantaneous luminosity examined in each data-taking period are shown with dashed  
1678 (solid) lines. This may be due to a residual APV saturation effect or possibly another  
1679 luminosity-related tracker inefficiency. We do not find it necessary to take any special  
1680 measures to account for this small effect in 2017 and 2018.

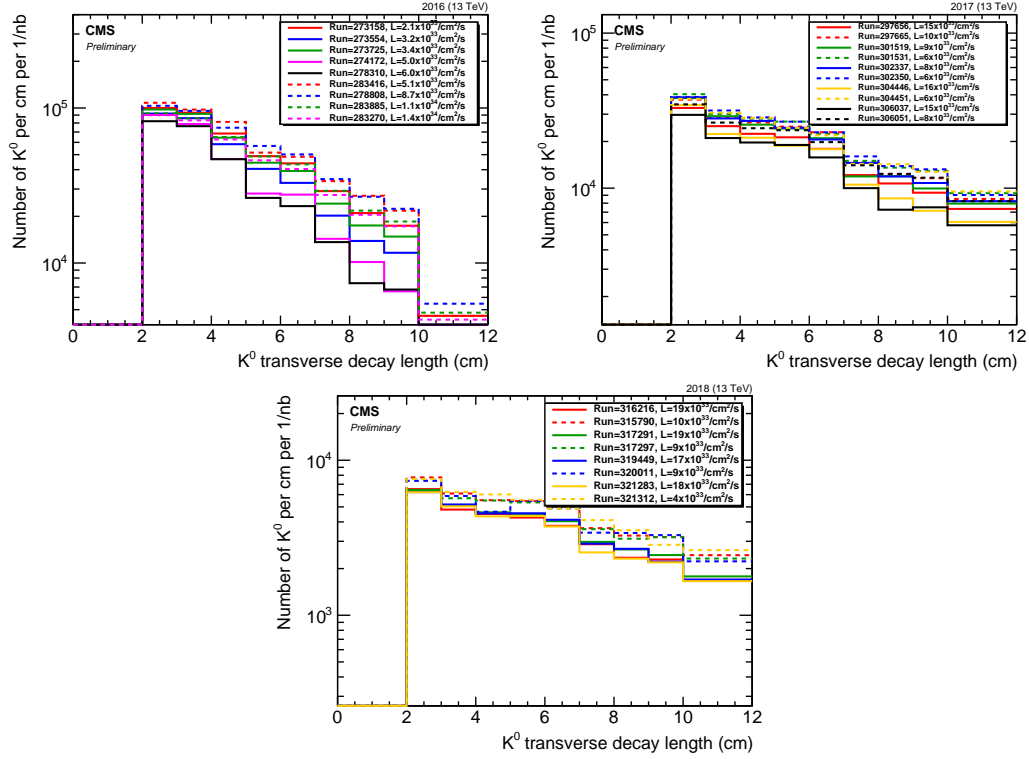


Figure A.1: Transverse decay length distribution of reconstructed  $K_0^0 \rightarrow \pi^+\pi^-$  candidates for various runs in 2016 (top left), 2017 (top right) and 2018 (bottom). The peak instantaneous luminosity of each run is indicated in the legend, and each distribution is normalized to the integrated luminosity of the run. In the 2016 plot, runs taken before (after) the APV25 saturation effect was mitigated are shown by solid (dashed) lines. In the 2017 plot, the run with lowest (highest) instantaneous luminosity examined in each data-taking era is plotted with a dashed (solid) line. Towards the end of 2017 (orange and black lines) the LHC ran with approximately 20% fewer proton bunches, meaning that the instantaneous luminosity per bunch crossing was higher than one might naively expect from the instantaneous luminosities shown in the legend.

1681

## Appendix B: Poorly measured lepton $|d_0|$ at large $|\eta|$

1682

We require muons to have  $|\eta| < 1.5$  due to the observed increase in width of the muon  $d_0$  distribution at large  $|\eta|$  in Drell-Yan simulation with  $Z \rightarrow \tau\tau \rightarrow ll$  events removed (see Fig. B.1 (left)). The width visibly increases at large  $|\eta|$  in all three years but is less pronounced in 2017 and 2018 due to the improved performance of the Phase-1 pixel detector. The upgraded pixel detector is also responsible for the overall difference in  $d_0$  width between years. Requiring muon  $|\eta| < 1.5$  has two effects: (1) it dramatically reduces the mismeasurement background in 2016 data in the  $\mu\mu$  channel, and (2) it removes a possible source of  $|d_0^a| - |d_0^b|$  correlation in which the correlation between muons in  $\eta$  leads to correlation between muons in  $|d_0|$ . As shown in Fig. B.1 (right), muons from  $\tilde{t}\tilde{t} \rightarrow \bar{l}b l\bar{b}$  events tend to have small  $|\eta|$ , so requiring muon  $|\eta| < 1.5$  has a minimal effect on the signal acceptance.

1693

Electron  $d_0$  resolution also worsens at large  $|\eta|$ . Furthermore, Fig. B.2 (left) shows that electrons from SM mesons are particularly concentrated  $|\eta| > 1.5$ . As in the muon case, electrons from  $\tilde{t}\tilde{t} \rightarrow \bar{l}b l\bar{b}$  events tend to have  $|\eta| < 1.5$  (see Fig. B.2), which implies that requiring electron  $|\eta| < 1.5$  will reduce the mismeasurement and SM meson backgrounds without significantly reducing signal acceptance.

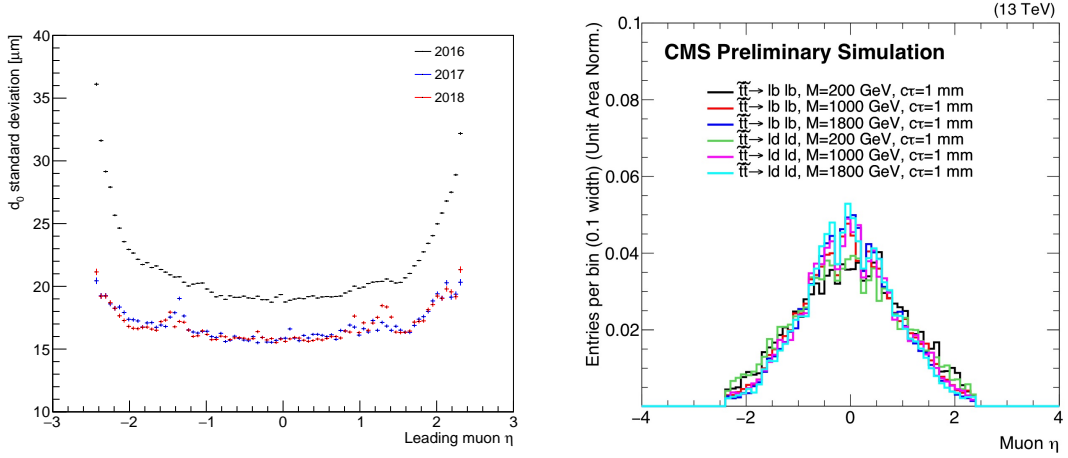


Figure B.1: The standard deviation of the leading muon  $d_0$  as a function of the leading muon  $\eta$  for simulated background events (left). To ensure that the variation in width is purely due to  $d_0$  resolution effects, we use a sample of simulated Drell-Yan events from which the  $Z \rightarrow \tau\tau \rightarrow ll$  events have been removed. Muon  $\eta$  distribution for simulated  $\tilde{t}\tilde{t} \rightarrow \bar{l}b \bar{l}b$  events (right). The  $\mu\mu$  preselection with a loosened  $|\eta|$  requirement is applied in both plots.

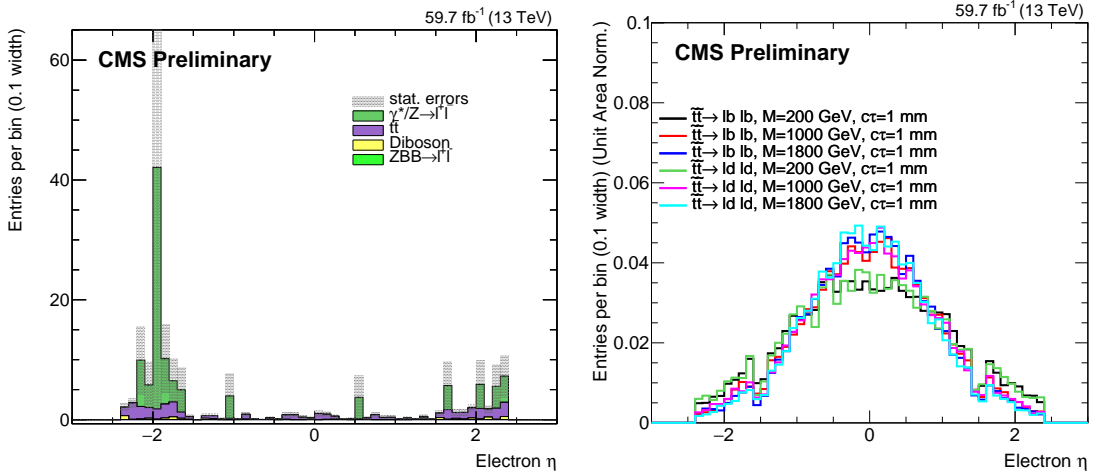


Figure B.2: Electron  $\eta$  distribution for simulated background events in which the electron parent particles are required to be SM mesons (left). Electron  $\eta$  distribution for simulated  $\tilde{t}\tilde{t} \rightarrow \bar{l}b \bar{l}b$  events (right). The  $e\mu$  preselection with a loosened  $\eta$  requirement is applied in both plots.

## Appendix C: Displaced tracking efficiency

1699 To measure the efficiency to reconstruct displaced, isolated, high- $p_T$  muons, our  
1700 collaborator Ian Tomalin performed a study with cosmic rays. The basic idea is to ap-  
1701 proximate the displaced tracking efficiency in data and simulation from the fraction of  
1702 cosmic-ray muons reconstructed in the muon system that have a corresponding track  
1703 in the tracker. The results of this study are used to assign a systematic uncertainty  
1704 in the signal efficiency (see Section 3.6) and define the upper bound of 10 cm on the  
1705 inclusive signal region (see Section 3.3).

1706 First, the cosmic-ray dataset is chosen. CMS collects cosmic-ray data in two  
1707 types of runs: (1) dedicated cosmic runs in which cosmic-ray muons are reconstructed  
1708 with dedicated reconstruction algorithms and (2) parasitic cosmic runs in which the  
1709 triggers veto bunch-crossing events to collect cosmic-ray data in otherwise normal  
1710 proton-proton running conditions. In the parasitic cosmic runs, the cosmic-ray muons  
1711 are reconstructed with the standard reconstruction algorithms as well as some dedi-  
1712 cated reconstruction algorithms. These two types of runs are then collected into two  
1713 datasets: (1) `Cosmics`, which contains only the dedicated cosmic runs and (2) `NoBPTX`,  
1714 which contains both the dedicated and parasitic cosmic runs. In each case, the strip  
1715 tracker electronics operate in the same mode used for proton-proton collisions. The

1716 NoBPTX datasets are used in this study because they include the same reconstruction  
1717 algorithms as used in the Displaced Leptons analysis.

1718 Events are collected with the `HLTL2Mu10NoVertexNoBPTX3BXv*` trigger, which ve-  
1719 toes events with proton-proton collisions and requires that a muon with  $p_T > 10 \text{ GeV}$   
1720 is reconstructed in the muon system. As in the Displaced Leptons analysis, the trig-  
1721 ger does not explicitly constrain the muon  $d_0$  or  $d_z$ . Following the study presented  
1722 in Appendix A, only eras G and H are used in 2016. The set of data-taking periods  
1723 with reliable detector performance is identified with particular attention paid to the  
1724 following properties: (1) suitable cosmic trigger timing configuration, (2) data qual-  
1725 ity assessed from reconstructed (as opposed to trigger-level) quantities, (3) trigger,  
1726 tracker, muon system, and track reconstruction known to be functioning well, and  
1727 (4) magnetic field value in normal range.

1728 To compare the displaced tracking efficiency between data and simulation, sim-  
1729 ulated cosmic-ray events are produced using the CMSCGEN generator [90]. The  
1730 simulated cosmic-ray muons have  $p_T > 20 \text{ GeV}$ ,  $|d_0| < 40 \text{ cm}$ ,  $|d_z| < 80 \text{ cm}$ , and ar-  
1731 rive within a 30 ns window centered on the time at which tracker readout efficiency  
1732 is greatest. The detector response is modeled with GEANT [70].

1733 In both data and simulated events, cosmic rays are reconstructed in the tracker  
1734 using the same track reconstruction algorithm that is used during proton-proton  
1735 collisions. This algorithm assumes particles propagate outwards from the center of  
1736 the detector, so cosmic-ray muons are typically reconstructed as two tracks: one  
1737 moving upward and one moving downwards. In the muon system, cosmic-ray muons  
1738 are reconstructed with two dedicated algorithms. The first is a two-leg algorithm  
1739 that reconstructs each cosmic-ray muon as two separate muons, one in the top half of

1740 CMS and the other in the bottom. The second is a one-leg algorithm that reconstructs  
1741 cosmic rays as a single muon that traverses the entire detector. The longer lever arm  
1742 provided by the one-leg algorithm generally results in more accurate measurements  
1743 of the muon curvature in the magnetic field.

1744 A preliminary event selection is then applied to the data and simulation. The  
1745 events are required to have one one-leg muon with  $p_T > 20 \text{ GeV}$  and at least 50 hits  
1746 in the muon system. While the  $p_T$  requirement of the muons selected in this study  
1747 is lower than the Displaced Leptons muon  $p_T$  requirement, the tracking efficiency  
1748 does not depend significantly on  $p_T$  in the relevant range. The one-leg muon is also  
1749 required to be within 0.3 rad of two two-leg muons in  $\phi$  in order to reject cosmic-ray  
1750 muon candidates that do not traverse the entire detector.

1751 The tracking efficiency is inferred from the fraction of selected one-leg muons that  
1752 are associated with a tracker track that has  $p_T > 15 \text{ GeV}$  and is within 0.2 rad in  $\phi$  of  
1753 the selected one-leg muon. To mimic the Displaced Leptons event selection, tracker  
1754 tracks are also required to have at least one pixel hit. Because each cosmic-ray muon  
1755 generally results in two tracker tracks, two separate efficiencies are measured. These  
1756 efficiencies are referred to as “upward” and “downward” according to the direction of  
1757 the relevant tracker track. The downward efficiency is expected to be more reliable  
1758 because the tracker readout electronics assume that particles propagate outward from  
1759 the center of the detector. The upward and downward efficiencies measured in this  
1760 study agree within a few percent, but the downward efficiencies are used for the  
1761 definitive measurement.

1762 The muon system also measures the cosmic-ray muon arrival time. The average  
1763 of the two two-leg muon arrival times provides the most precise measurement of the

Table C.1: Cosmic-ray muon arrival time requirements used when measuring displaced tracking efficiency in data and simulation.

	2016–2017	2018
Data	$-13 \text{ ns} < t_{\mu\text{on}} < -7 \text{ ns}$	$-8 \text{ ns} < t_{\mu\text{on}} < -2 \text{ ns}$
Simulation	$-38 \text{ ns} < t_{\mu\text{on}} < -32 \text{ ns}$	$-40 \text{ ns} < t_{\mu\text{on}} < -34 \text{ ns}$

1764 cosmic-ray muon arrival time. This approach provides a time resolution on the order  
 1765 of 5 ns, whereas the time resolution provided by one-leg muons can be an order of  
 1766 magnitude greater.

1767 The selected one-leg muons with  $|d_0| < 8 \text{ cm}$  and  $|d_z| < 20 \text{ cm}$  are used to study the  
 1768 tracking efficiency dependence on cosmic-ray muon arrival time. Figure C.1 shows the  
 1769 distribution of the measured arrival time while Fig. C.2 shows the measured downward  
 1770 tracking efficiency as a function of measured arrival time. The disagreement between  
 1771 data and simulation in measured arrival time is simply an artifact of the specified  
 1772 simulation time window. Despite this offset, the efficiency shows a clear peak with a  
 1773 width of approximately 15 ns in both data and simulation. Based on the results of  
 1774 Fig. C.2, muons used in the downward tracking efficiency measurement must also pass  
 1775 the requirements listed in Table C.1. Using the upward efficiency produces similar  
 1776 results that are shifted by approximately 5 ns. The same sample of one-leg muons is  
 1777 also used to measure the downward tracking efficiency as a function of run number.  
 1778 No meaningful dependence is identified.

1779 The downward tracking efficiency is then measured using all selected one-leg  
 1780 muons that meet the timing requirements specified in Table C.1. The downward track-  
 1781 ing efficiency as a function of  $|d_0|$  and  $|d_z|$  is shown for all three years in Fig. C.3. The

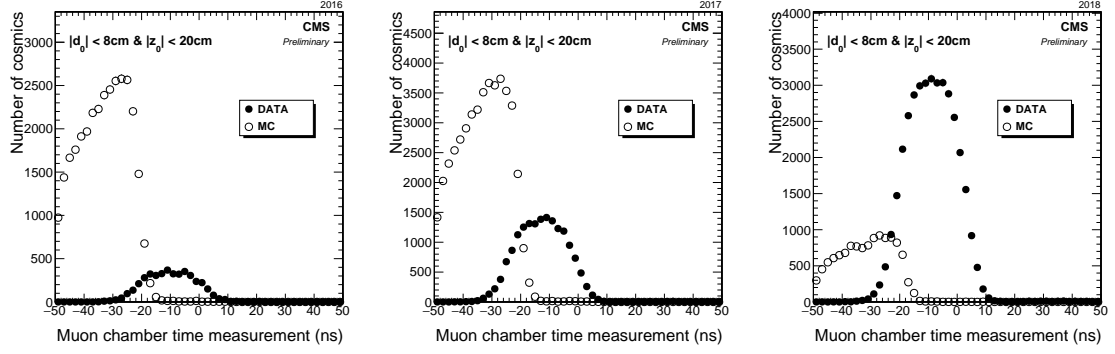


Figure C.1: Distribution of the arrival time of cosmic rays at their point of closest approach to the beamline as measured by the muon system in 2016 (left), 2017 (center), and 2018 (right) in data and simulation. Only cosmic-ray muons with  $|d_0| < 8\text{ cm}$  and  $|z_0| < 20\text{ cm}$  are considered.

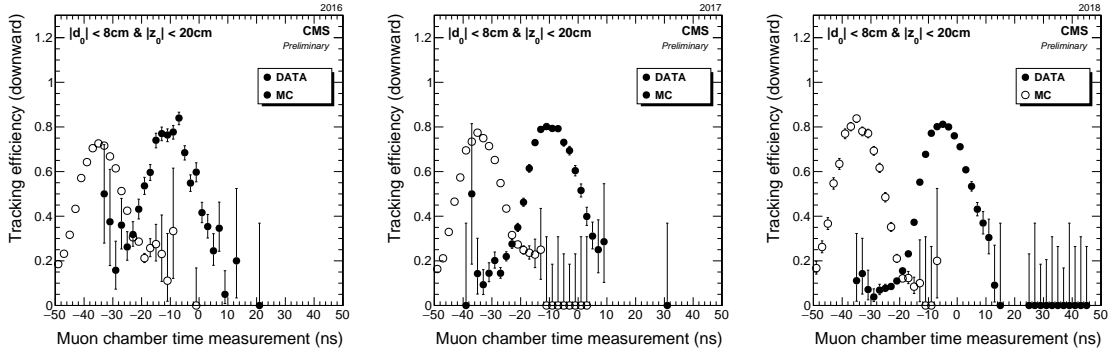


Figure C.2: Measured downward tracking efficiency versus cosmic ray muon arrival time in 2016 (left), 2017 (center), and 2018 (right) in data and simulation. Only cosmic-ray muons with  $|d_0| < 8\text{ cm}$  and  $|z_0| < 20\text{ cm}$  are considered.

1782 tracking efficiency is found to be nonzero out to at least  $|d_0| \leq 10$  cm and  $|d_z| \leq 30$  cm  
1783 in all three years. We also note that removing the pixel-hit requirement increases this  
1784 range to approximately  $|d_0| \leq 30$  cm and  $|d_z| \leq 50$  cm.

1785 The results of Fig. C.3 are used to estimate a systematic uncertainty in the sim-  
1786 ulated signal efficiency arising from the displaced tracking efficiency. A simulated  
1787  $\tilde{t}\tilde{t} \rightarrow \bar{l}b \bar{l}b$  sample with a top squark mass of 1800 GeV and proper decay length  
1788  $c\tau = 100$  cm is considered as it produces leptons with the largest impact parameters  
1789 and therefore represents the most challenging scenario for the displaced track recon-  
1790 struction. To accommodate the pixel hit requirements, only those events in which  
1791 both top squarks decay within the volume of the pixel detector are considered. First,  
1792 the  $|d_0|$  and  $|d_z|$  of both leptons in this subset of signal events are noted. Next, a  
1793 two-dimensional plot of tracking efficiency as a function of  $|d_0|$  and  $|d_z|$ ,  $\epsilon(|d_0|, |d_z|)$ , is  
1794 produced from the cosmic-ray muons in data and simulated cosmic-ray events. Using  
1795 this plot, the mean efficiency to reconstruct both lepton tracks in the simulated signal  
1796 events is evaluated as:

$$\frac{1}{N} \sum_i \epsilon(|d_0|_i^{(1)}, |z_0|_i^{(1)}) \epsilon(|d_0|_i^{(2)}, |z_0|_i^{(2)}) \quad (\text{C.1})$$

1797 where the sum extends over the  $N$  events in the signal sample and the superscripts (1)  
1798 and (2) denote the two leptons in each event. For each year, the relative systematic  
1799 uncertainty in the efficiency to reconstruct both lepton tracks is then taken from  
1800 the ratio of the efficiencies in data and simulation. The resulting efficiencies and  
1801 systematic uncertainties are listed in Table C.2.

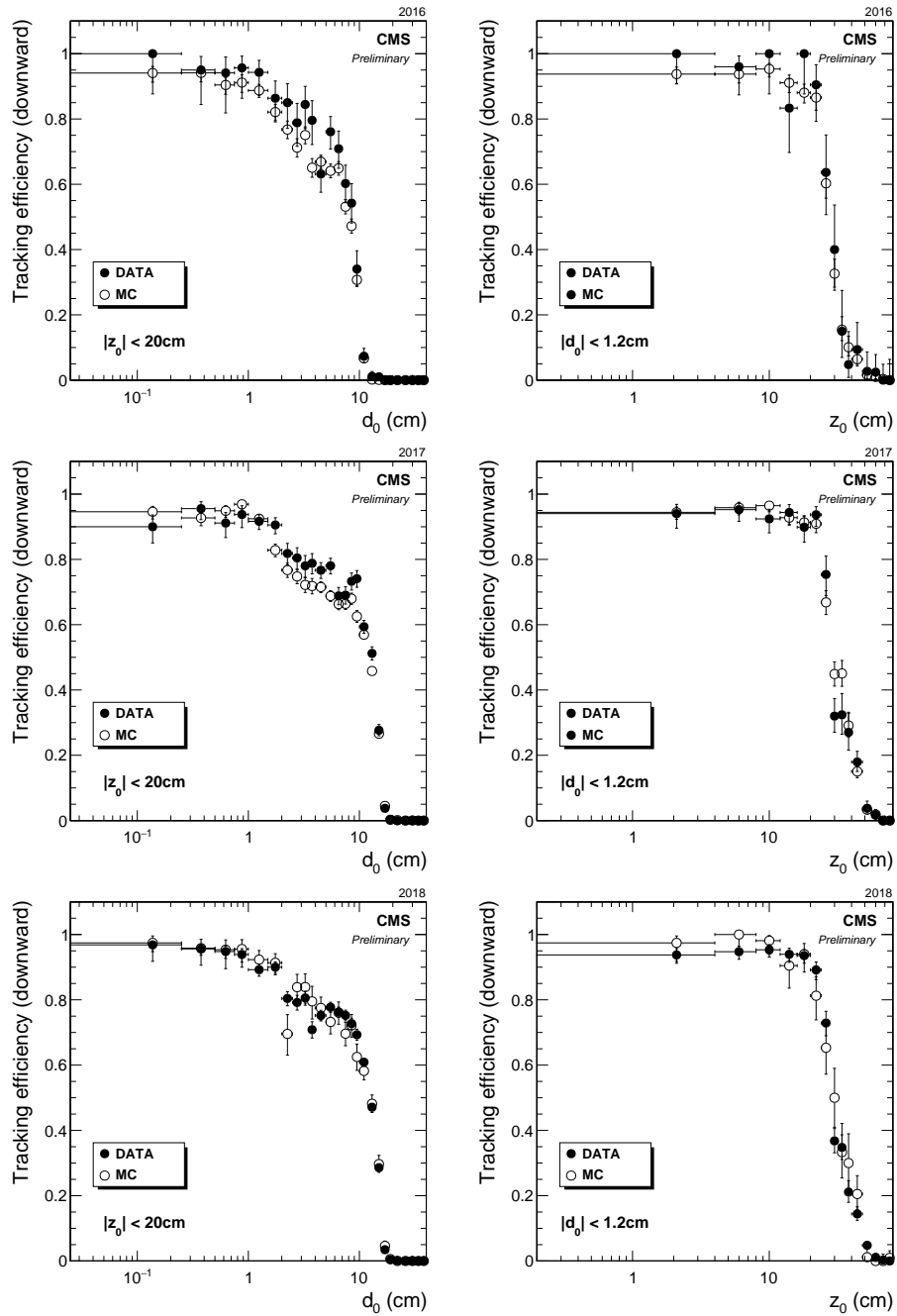


Figure C.3: Measured downward tracking efficiency in 2016 (top), 2017 (middle), and 2018 (bottom) versus  $|d_0|$  (left) and  $|d_z|$  (right) in data and simulation.  $|d_z|$  ( $|d_0|$ ) impact parameter is constrained to less than 20 cm (1.2 cm) when plotting against  $|d_0|$  ( $|d_z|$ ).

Table C.2: Mean measured efficiency to reconstruct both lepton tracks in simulated  $\tilde{t}\tilde{t} \rightarrow l b \bar{l} \bar{b}$  events in data and simulation and the resulting systematic uncertainty. The top squark mass and proper decay length are assumed to be 1800 GeV and 100 cm.

	2016	2017	2018
Efficiency in data	$57.5 \pm 2.1\%$	$55.3 \pm 1.1\%$	$56.1 \pm 0.7\%$
Efficiency in simulation	$50.3 \pm 1.0\%$	$52.3 \pm 0.7\%$	$57.5 \pm 1.1\%$
Systematic uncertainty	$14.1 \pm 4.3\%$	$5.8 \pm 2.3\%$	$2.4 \pm 2.2\%$

## Bibliography

- [1] CMS Collaboration. Performance of electron reconstruction and selection with the CMS detector in proton-proton collisions at  $\sqrt{s} = 8$  TeV. *Journal of Instrumentation*, 10(06), Jun 2015.
- [2] Summaries of CMS cross section measurements. [twiki.cern.ch/twiki/bin/view/CMSPublic/PhysicsResultsCombined](http://twiki.cern.ch/twiki/bin/view/CMSPublic/PhysicsResultsCombined). Accessed: 2021-04-04.
- [3] CMS Supersymmetry Physics Results. [twiki.cern.ch/twiki/bin/view/CMSPublic/PhysicsResultsSUS](http://twiki.cern.ch/twiki/bin/view/CMSPublic/PhysicsResultsSUS). Accessed: 2021-04-04.
- [4] Brian Shuve. Theory Overview of Long-Lived Particles at the LHC. [indico.cern.ch/event/607314/contributions/2542308](https://indico.cern.ch/event/607314/contributions/2542308).
- [5] Lyndon Evans and Philip Bryant. LHC Machine. *Journal of Instrumentation*, 3(08), Aug 2008.
- [6] Esma Mobs. The CERN accelerator complex - 2019. (CERN-Graphics-2019-002), Jul 2019.
- [7] Jorg Wenninger. Operation and Configuration of the LHC in Run 2. (CERN-ACC-NOTE-2019-0007), Mar 2019.
- [8] AC Team. Diagram of an LHC dipole magnet. [cds.cern.ch/record/40524](https://cds.cern.ch/record/40524), Jun 1999.
- [9] Tai Sakuma. 3D SketchUp images of the CMS detector (120918). (CMS-OUTREACH-2018-008), May 2016.
- [10] CMS Collaboration. The CMS experiment at the CERN LHC. The Compact Muon Solenoid experiment. *JINST*, 3, 2008.
- [11] Run II Pixel Performance plots for data and simulation. [twiki.cern.ch/twiki/bin/view/CMSPublic/PixelOfflinePlots2016](http://twiki.cern.ch/twiki/bin/view/CMSPublic/PixelOfflinePlots2016). Accessed: 2021-04-04.
- [12] The Tracker Group of the CMS Collaboration. The CMS Phase-1 Pixel Detector Upgrade. *JINST*, 16(02), 2021.

- 1828 [13] CMS Collaboration. Observation of a new boson at a mass of 125 GeV with the  
1829 CMS experiment at the LHC. *PLB*, 716, 2012.
- 1830 [14] CMS Collaboration. CMS Physics: Technical Design Report Volume 1: Detector  
1831 Performance and Software. (CERN-LHCC-2006-001), 2006.
- 1832 [15] CMS Collaboration. Particle-flow reconstruction and global event description  
1833 with the CMS detector. *JINST*, 12, 2017.
- 1834 [16] Image courtesy of Jamie Antonelli.
- 1835 [17] David J. Gross and Frank Wilczek. Asymptotically Free Gauge Theories. I. *Phys.*  
1836 *Rev. D*, 8, Nov 1973.
- 1837 [18] H. Fritzsch, M. Gell-Mann, and H. Leutwyler. Advantages of the color octet  
1838 gluon picture. *Physics Letters B*, 47(4), 1973.
- 1839 [19] Steven Weinberg. A Model of Leptons. *Phys. Rev. Lett.*, 19, Nov 1967.
- 1840 [20] Jeffrey Goldstone, Abdus Salam, and Steven Weinberg. Broken symmetries.  
1841 *Phys. Rev.*, 127, Aug 1962.
- 1842 [21] F. Englert and R. Brout. Broken Symmetry and the Mass of Gauge Vector  
1843 Mesons. *Phys. Rev. Lett.*, 13, Aug 1964.
- 1844 [22] Peter Ware Higgs. Broken symmetries, massless particles and gauge fields. *Phys.*  
1845 *Lett.*, 12, 1964.
- 1846 [23] G. S. Guralnik, C. R. Hagen, and T. W. B. Kibble. Global Conservation Laws  
1847 and Massless Particles. *Phys. Rev. Lett.*, 13, Nov 1964.
- 1848 [24] ATLAS Collaboration. Observation of a new particle in the search for the stan-  
1849 dard model Higgs boson with the ATLAS detector at the LHC. *PLB*, 716, 2012.
- 1850 [25] CMS Collaboration. Combined measurements of Higgs boson couplings in pro-  
1851 ton–proton collisions at  $\sqrt{s} = 13$  TeV. *Eur. Phys. J. C*, 79(5), 2019.
- 1852 [26] ATLAS Collaboration. Combined measurements of Higgs boson production and  
1853 decay using up to  $80 \text{ fb}^{-1}$  of proton-proton collision data at  $\sqrt{s} = 13$  TeV  
1854 collected with the ATLAS experiment. *Phys. Rev. D*, 101, Jan 2020.
- 1855 [27] Masataka Fukugita and P. J. E. Peebles. The Cosmic Energy Inventory. *The*  
1856 *Astrophysical Journal*, 616(2), Dec 2004.
- 1857 [28] Gian Francesco Giudice. Naturally Speaking: The Naturalness Criterion and  
1858 Physics at the LHC. *Perspectives on LHC Physics*, Jun 2008.

- 1859 [29] Gerard 't Hooft. Naturalness, chiral symmetry, and spontaneous chiral symmetry  
1860 breaking. *NATO Sci. Ser. B*, 59, 1980.
- 1861 [30] Nima Arkani–Hamed, Savas Dimopoulos, and Gia Dvali. The hierarchy problem  
1862 and new dimensions at a millimeter. *Physics Letters B*, 429(3-4), Jun 1998.
- 1863 [31] Stephen P. Martin. A Supersymmetry Primer. *Advanced Series on Directions in*  
1864 *High Energy Physics*, Jul 1998.
- 1865 [32] Nathaniel Craig. The State of Supersymmetry after Run I of the LHC. In *Beyond*  
1866 *the Standard Model after the first run of the LHC*, Sep 2013.
- 1867 [33] Particle Data Group. Review of Particle Physics. *Progress of Theoretical and*  
1868 *Experimental Physics*, 2020(8), 08 2020.
- 1869 [34] Zhen Liu and Brock Tweedie. The fate of long-lived superparticles with hadronic  
1870 decays after LHC Run 1. *Journal of High Energy Physics*, 2015(6), Jun 2015.
- 1871 [35] W. Kilian, T. Plehn, P. Richardson, and E. Schmidt. Split Supersymmetry at  
1872 Colliders. *Eur. Phys. J. C*, 39, Oct 2004.
- 1873 [36] F. Paige and J. Wells. Anomaly mediated SUSY breaking at the LHC. (hep-  
1874 ph/0001249), Jan 2000.
- 1875 [37] Peter W. Graham, David E. Kaplan, Surjeet Rajendran, and Prashant Saraswat.  
1876 Displaced Supersymmetry. *JHEP*, 07, 2012.
- 1877 [38] Lawrence J. Hall and Mahiko Suzuki. Explicit R-parity breaking in supersym-  
1878 metric models. *Nuclear Physics B*, 231(3), 1984.
- 1879 [39] Linear accelerator 2. [cds.cern.ch/record/1997427](https://cds.cern.ch/record/1997427), Sep 2012.
- 1880 [40] The Proton Synchrotron Booster. [cds.cern.ch/record/1997372](https://cds.cern.ch/record/1997372), Jul 2012.
- 1881 [41] Proton Synchrotron. [cds.cern.ch/record/1479637](https://cds.cern.ch/record/1479637), 1959.
- 1882 [42] The Super Proton Synchrotron. [cds.cern.ch/record/1997188](https://cds.cern.ch/record/1997188), Jan 2012.
- 1883 [43] CMS Collaboration. CMS Technical Design Report, Volume II: Physics Perfor-  
1884 mance. *J. Phys. G*, 34(6), 2007.
- 1885 [44] CMS Collaboration. [cms.cern/collaboration](https://cms.cern/collaboration). Accessed: 2021-03-28.
- 1886 [45] Aaron Dominguez et al. CMS Technical Design Report for the Pixel Detector  
1887 Upgrade. (CERN-LHCC-2012-016), Sep 2012.
- 1888 [46] Lea Michaela Caminada. Performance and Operation of the CMS Phase 1 Pixel  
1889 Detector. (CMS-CR-2018-067), Jun 2018.

- 1890 [47] CMS Collaboration. Performance of the CMS muon detector and muon recon-  
 1891 struction with proton-proton collisions at  $\sqrt{s} = 13$  TeV. *Journal of Instrumen-*  
 1892 *tation*, 13(06), Jun 2018.
- 1893 [48] M.A. Shah et al. The CMS RPC detector performance and stability during LHC  
 1894 RUN-2. *Journal of Instrumentation*, 14(11), Nov 2019.
- 1895 [49] Mia Tosi. The CMS trigger in Run 2. (CMS-CR-2017-340), Oct 2017.
- 1896 [50] L. Cadamuro. The CMS Level-1 trigger system for LHC Run II. *Journal of*  
 1897 *Instrumentation*, 12(03), 2017.
- 1898 [51] W. Adam, R. Fröhwirth, A. Strandlie, and T. Todorov. Reconstruction of elec-  
 1899 trons with the Gaussian-sum filter in the CMS tracker at the LHC. *Journal of*  
 1900 *Physics G: Nuclear and Particle Physics*, 31(9), Jul 2005.
- 1901 [52] CMS Collaboration. Search for Displaced Supersymmetry in Events with an  
 1902 Electron and a Muon with Large Impact Parameters. *Physical Review Letters*,  
 1903 114(6), Feb 2015.
- 1904 [53] CMS Collaboration. Search for displaced leptons in the e-mu channel. (CMS-  
 1905 PAS-EXO-16-022), 2016.
- 1906 [54] ATLAS Collaboration. Search for displaced leptons in  $\sqrt{s} = 13$  TeV  $pp$  collisions  
 1907 with the ATLAS detector, 2020.
- 1908 [55] Juliette Alimena et al. Searching for long-lived particles beyond the Standard  
 1909 Model at the Large Hadron Collider. *Journal of Physics G: Nuclear and Particle*  
 1910 *Physics*, 47(9), Sep 2020.
- 1911 [56] CMS Collaboration. Search for disappearing tracks in proton-proton collisions  
 1912 at  $\sqrt{s} = 13$  TeV. *Physics Letters B*, 806, Jul 2020.
- 1913 [57] CMS Collaboration. Search for long-lived particles using delayed photons in  
 1914 proton-proton collisions at  $\sqrt{s} = 13$  TeV. *Physical Review D*, 100(11), Dec 2019.
- 1915 [58] CMS Collaboration. Search for long-lived particles using nonprompt jets and  
 1916 missing transverse momentum with proton-proton collisions at  $\sqrt{s} = 13$  TeV.  
 1917 *Physics Letters B*, 797, Oct 2019.
- 1918 [59] Johan Alwall et al. The automated computation of tree-level and next-to-leading  
 1919 order differential cross sections, and their matching to parton shower simulations.  
 1920 *JHEP*, 07, 2014.
- 1921 [60] Rikkert Frederix and Stefano Frixione. Merging meets matching in MC@NLO.  
 1922 *JHEP*, 12, 2012.

- 1923 [61] Johan Alwall et al. Comparative study of various algorithms for the merging of  
1924 parton showers and matrix elements in hadronic collisions. *Eur. Phys. J. C*, 53,  
1925 2008.
- 1926 [62] Stefano Frixione and Bryan R. Webber. Matching NLO QCD computations and  
1927 parton shower simulations. *JHEP*, 06, 2002.
- 1928 [63] Paolo Nason. A New method for combining NLO QCD with shower Monte Carlo  
1929 algorithms. *JHEP*, 11, 2004.
- 1930 [64] Stefano Frixione, Paolo Nason, and Carlo Oleari. Matching NLO QCD com-  
1931 putations with Parton Shower simulations: the POWHEG method. *JHEP*, 11,  
1932 2007.
- 1933 [65] Simone Alioli, Paolo Nason, Carlo Oleari, and Emanuele Re. NLO vector-boson  
1934 production matched with shower in POWHEG. *JHEP*, 07, 2008.
- 1935 [66] Simone Alioli, Paolo Nason, Carlo Oleari, and Emanuele Re. A general frame-  
1936 work for implementing NLO calculations in shower Monte Carlo programs: the  
1937 POWHEG BOX. *JHEP*, 06, 2010.
- 1938 [67] Torbjörn Sjöstrand et al. An introduction to PYTHIA 8.2. *Comput. Phys.*  
1939 *Commun.*, 191, 2015.
- 1940 [68] CMS Collaboration. Event generator tunes obtained from underlying event and  
1941 multiparton scattering measurements. *Eur. Phys. J.*, C76(3), 2016.
- 1942 [69] CMS Collaboration. Extraction and validation of a new set of CMS PYTHIA8  
1943 tunes from underlying-event measurements. *EPJC*, 80, 2020.
- 1944 [70] S. Agostinelli et al. Geant4—a simulation toolkit. *Nuclear Instruments and*  
1945 *Methods in Physics Research Section A: Accelerators, Spectrometers, Detectors*  
1946 *and Associated Equipment*, 506(3), 2003.
- 1947 [71] Johan Alwall et al. A standard format for Les Houches event files. *Comput.*  
1948 *Phys. Commun.*, 176, 2007.
- 1949 [72] B.C. Allanach et al. The Snowmass points and slopes: Benchmarks for SUSY  
1950 searches. *EPJC*, 25, 2002.
- 1951 [73] CMS Collaboration. Precision measurement of the structure of the CMS inner  
1952 tracking system using nuclear interactions. *JINST*, 13, 2018.
- 1953 [74] CMS Collaboration. Precision measurement of the structure of the CMS inner  
1954 tracking system using nuclear interactions with data collected in 2018. *CMS-*  
1955 *DP-2019-001*, 2019.

- 1956 [75] Jared A. Evans and Jessie Shelton. Long-lived staus and displaced leptons at  
 1957 the LHC. *JHEP*, 04, 2016.
- 1958 [76] CMS Collaboration. Identification of b quark jets at the CMS Experiment in the  
 1959 LHC Run 2. (CMS-PAS-BTV-15-001), 2016.
- 1960 [77] CMS Collaboration. CMS luminosity measurements for the 2016 data taking  
 1961 period. CMS Physics Analysis Summary CMS-PAS-LUM-17-001, 2017.
- 1962 [78] CMS Collaboration. CMS luminosity measurements for the 2017 data-taking  
 1963 period at  $\sqrt{s} = 13$  TeV. CMS Physics Analysis Summary CMS-PAS-LUM-17-  
 1964 004, 2018.
- 1965 [79] CMS Collaboration. CMS luminosity measurements for the 2018 data-taking  
 1966 period at  $\sqrt{s} = 13$  TeV. CMS Physics Analysis Summary CMS-PAS-LUM-18-  
 1967 002, 2018.
- 1968 [80] CMS Collaboration. Measurement of the inelastic proton-proton cross section at  
 1969  $\sqrt{s} = 13$  TeV. *JHEP*, 07, 2018.
- 1970 [81] Thomas Junk. Confidence level computation for combining searches with small  
 1971 statistics. *Nucl. Instrum. Meth. A*, 434, 1999.
- 1972 [82] A. L. Read. Presentation of search results: the  $CL_s$  technique. In *Durham IPPP*  
 1973 *Workshop: Advanced Statistical Techniques in Particle Physics*, Durham, UK,  
 1974 Mar 2002. [*J. Phys. G* 28 (2002) 2693].
- 1975 [83] Glen Cowan, Kyle Cranmer, Eilam Gross, and Ofer Vitells. Asymptotic formulae  
 1976 for likelihood-based tests of new physics. *Eur. Phys. J. C*, 71, 2011.
- 1977 [84] ATLAS Collaboration, CMS Collaboration, LHC Higgs Combination Group.  
 1978 Procedure for the LHC Higgs boson search combination in Summer 2011. (CMS-  
 1979 NOTE-2011-005, ATL-PHYS-PUB-2011-11), 2011.
- 1980 [85] B. Aa.b Petersen and C. Schwick. Experiment Requests and Constraints for Run  
 1981 3. In *9th LHC Operations Evian Workshop*, 2019.
- 1982 [86] Longer term LHC schedule. [lhcc-commissioning.web.cern.ch/schedule/LHC-long-term.htm](http://lhcc-commissioning.web.cern.ch/schedule/LHC-long-term.htm). Accessed: 2021-04-04.
- 1984 [87] Robert Bainbridge. Recording and reconstructing 10 billion unbiased b hadron  
 1985 decays in CMS. *EPJ Web Conf.*, 245, 2020.
- 1986 [88] Wolfgang Adam et al. The effect of highly ionising particles on the CMS silicon  
 1987 strip tracker. *Nucl. Instrum. Meth. A*, 543, 2005.

- 1988 [89] M. J. French et al. Design and results from the APV25, a deep sub-micron  
1989 CMOS front-end chip for the CMS tracker. *Nucl. Instrum. Methods Phys. Res.*,  
1990 *A*, 466(2), 2001.
- 1991 [90] Philipp Biallass, Thomas Hebbeker, and K Höpfner. Simulation of Cosmic Muons  
1992 and Comparison with Data from the Cosmic Challenge using Drift Tube Cham-  
1993 bers. (CMS-NOTE-2007-024), Mar 2007.